Institut für Chemie

Arbeitskreis Angewandte Polymerchemie

New inverse hydrogel opals as protein-responsive sensors

DISSERTATION

zur Erlangung des akademischen Grades

“doctor rerum naturalium” (Dr. rer. nat.)
in der Wissenschaftsdisziplin Kolloid- und Polymerchemie

eingereicht an der
Mathematisch-Naturwissenschaftlichen Fakultät
der Universität Potsdam
von
M.Sc. Martin Sütterlin

Gutachter:
1. Prof. Dr. André Laschewsky, Universität Potsdam
2. Prof. Dr. Andreas Taubert, Universität Potsdam
3. Prof. Dr. Rainer Haag, Freie Universität Berlin

eingereicht am: 25.10.2013
Tag der mündlichen Prüfung: 13.03.2014

Acknowledgements

Zu allererst danke ich Herrn Prof. Dr. André Laschewsky herzlich für die Möglichkeit in seiner Arbeitsgruppe zu promovieren, für die Überlassung dieses spannenden Themas und für die Freiheit eigene Ideen einzubringen. Die Diskussionen waren immer sehr lehrreich und informativ, ob es nun um die Chemie oder andere Themen ging.

Weiterer Dank gilt Dr. Erik Wischerhoff für die alltägliche Betreuung der Arbeit am IAP, für die anregenden Diskussionen sowie für das Korrekturlesen dieser Arbeit.

Dem Fraunhofer IAP, vertreten durch Herrn Prof. Dr. Hans-Peter Fink, gilt mein Dank für die Möglichkeit, die Arbeit im Rahmen der Kooperation mit der Universität Potsdam in den Räumlichkeiten des IAPs durchführen zu dürfen.

Herzlichen Dank an alle, die fachlich direkt zu dieser Arbeit beitragen haben. Namentlich Herr Prof. Koetz und Frau Dr. Tiersch (AG Koetz, UP) für die SEM-Aufnahmen der inversen Opale, Herr Dr. Wieland und Frau Stegmann (IAP) für GPC-Messungen, Herr Dipl.-Ing. Stiller (AG Neher, UP) für die AFM-Aufnahmen der Kolloid Kristalle, Prof. Kleinpeter und seinem Team für die NMR-Messungen sowie Herr Dr. Buller für die Synthese und Überlassung des HABA-Derivats.

Mein Dank gilt natürlich der “Laborgang” um Jens und Sandor, die mir stets mit Rat und Tat zur Seite standen, aber auch für jeden Spaß zu haben waren. Auch wenn wir uns in Punkto Musikgeschmack nicht immer ganz einig waren, so waren die Arbeitstage mit Euch trotzdem nie langweilig.

Den Bürokollegen Jonas, Anna, Anne E. und Jean-Philippe der “Schaltzentrale der Macht” danke ich ebenfalls für anregende Gespräche und für die Toleranz der Kaffeerunde. Weiter bedanke ich mich bei allen Mitdoktoranden, Mitarbeitern der AG Laschewsky und des FB4, sowie den weiteren Weggefährten für die tolle Zeit, besonders Sahika, Frank, Robert, Viet, Laura, Christoph, Jan, Michael, Anne S., Kristin, Sophia, Tina, Sabrina und Steffi.

Weiterer Dank gilt meiner Schwester Katrin und all meinen Freunden für die schöne Zeit abseits der Arbeit. Ebenso meiner lieben Freundin Sabrina, die immer für mich da war.

Ein ganz besonderer Dank gilt meinen Eltern, ohne die ich meinen Ausbildungsweg nicht so ohne Weiteres hätte begehen können und die mich bei allem unterstützt haben.

Abstract

Zusammenfassung

In dieser Arbeit wird die Entwicklung von temperatur- und proteinresponsiven Sensormaterialien auf Basis von biokompatiblen, inversen Hydrogelopalen (IHO) vorgestellt, mit welchen die spezifische Erkennung größerer Biomoleküle visuell ausgelesen werden kann. Die Darstellung der IHOs erfolgte mittels Templatverfahren, bei dem im ersten Schritt monodisperse Silicapartikel vertikal auf Objektträger abgeschieden wurden. Die so erhaltenen Kolloidkristalle mit einer Dicke von 5 µm zeigten opaleszente Reflexionen aufgrund der gleichförmigen Anordnung der Partikel.

Im zweiten Schritt wurde das Templat in eine Matrix aus biokompatiblen, thermoresponsiven Hydrogelen eingebettet. Die Comonomere wurden aus der Familie der Oligo(ethylenglykol)methacrylate ausgewählt. Zur Synthese des Hydrogels wurde die Monomerlösung in eine Polymerisationsform injiziert, welche die Kolloidkristalle als Templat beinhaltete. Die Zwischenräume der Templatpartikel wurden mit der Monomerlösung gefüllt und das Hydrogelnetzwerk per UV-Polymerisation erhalten. Die Templatpartikel wurden anschließend nasschemisch heraus gelöst, so dass eine poröse innere Struktur erhalten wurde. Die regelmäßige Anordnung der Poren und damit die opaleszenten Reflexionen wurden dabei beibehalten, so dass diese Systeme als inverse Hydorgelopale bezeichnet werden. Ein Porendurchmesser von mehreren hundert Nanometer, sowie durchgängige Verbindungskanäle zwischen den einzelnen Poren sollten eine Diffusion von großen (Bio)molekülen erleichtern, was bei bisherigen Systemen ein Problem darstellte. Die Copolymerzusammensetzung wurde dabei so gewählt, dass ein Kollaps des Hydrogels über 35 °C stattfand. Alle Hydrogele zeigten ausgeprägte Quellung in Wasser unterhalb der kritischen Temperatur. Der Einbau von reaktiven Comonomeren mit Hydroxylgruppen gewährleistete dabei die Funktionalisierbarkeit des Hydrogels mit Erkennungsgruppen für entsprechende Analytmoleküle, wie z.B. Proteine.

Als Testsystem wurde Biotin als Erkennungseinheit für Avidin in das Hydrogel mittels polymeranaloger Steglich Veresterung eingebaut. Die Menge an zugänglichem Biotin wurde dabei per colorimetrischem Bindungsassay quantifiziert. Dabei zeigte sich, dass sich die Wellenlänge der Reflexion nach Zugabe von Avidin zum biotinylierten inversen Hydrogelopal signifikant verschob und damit das Bindungsereignis visuell auslesbar ist. Dieser Effekt beruht auf dem veränderten Quellungsverhalten des Hydrogels nach Bindung des hydrophilen Proteins Avidin in Wasser, welches durch den thermosresponsiven Charakter des Hydrogels verstärkt ist. Ein Aufweiten oder Schrumpfen der Poren ändert die Abstände der gleichmäßig angeordneten Poren, welche für die Farbe des inversen Opals verantwortlich sind. Auf Basis dieser Erkenntnisse lassen sich möglicherweise Sensormaterialen für die Erkennung weiterer Biomoleküle in der Größenordnung von Avidin erstellen.

Abstract

In this work, the development of temperature- and protein-responsive sensor materials based on biocompatible, inverse hydrogel opals (IHOs) is presented. With these materials, large biomolecules can be specifically recognised and the binding event visualised. The preparation of the IHOs was performed with a template process, for which monodisperse silica particles were vertically deposited onto glass slides as the first step. The obtained colloidal crystals with a thickness of 5 µm displayed opalescent reflections because of the uniform alignment of the colloids.

As a second step, the template was embedded in a matrix consisting of biocompatible, thermoresponsive hydrogels. The comonomers were selected from the family of oligo(ethylene glycol)methacrylates. The monomer solution was injected into a polymerisation mould, which contained the colloidal crystals as a template. The space in-between the template particles was filled with the monomer solution and the hydrogel was cured *via* UV-polymerisation. The particles were chemically etched, which resulted in a porous inner structure. The uniform alignment of the pores and therefore the opalescent reflection were maintained, so these system were denoted as inverse hydrogel opals. A pore diameter of several hundred nanometres as well as interconnections between the pores should facilitate a diffusion of bigger (bio)molecules, which was always a challenge in the presented systems until now. The copolymer composition was chosen to result in a hydrogel collapse over 35 °C. All hydrogels showed pronounced swelling in water below the critical temperature. The incorporation of a reactive monomer with hydroxyl groups ensured a potential coupling group for the introduction of recognition units for analytes, e.g. proteins.

As a test system, biotin as a recognition unit for avidin was coupled to the IHO *via* polymer-analogous Steglich esterification. The amount of accessible biotin was quantified with a colorimetric binding assay. When avidin was added to the biotinylated IHO, the wavelength of the opalescent reflection was significantly shifted and therefore the binding event was visualised. This effect is based on the change in swelling behaviour of the hydrogel after binding of the hydrophilic avidin, which is amplified by the thermoresponsive nature of the hydrogel. A swelling or shrinking of the pores induces a change in distance of the crystal planes, which are responsible for the colour of the reflection. With these findings, the possibility of creating sensor materials or additional biomolecules in the size range of avidin is given.

Abbreviations and variables

AFM	atomic force microscopy
bIHO	biotinylated inverse hydrogel opal
CC	colloidal crystal
CP	cloud point
DCC	*N,N*'-dicyclohexyl-carbodiimide
DCM	dichloromethane
DCU	dicyclohexylurea
DLS	dynamic light scattering
DMAP	4-dimethylaminopyridine
DMF	dimethylformamide
DSC	differential scanning calorimetry
EG	ethylene glycol
EtOH	ethanol
F	degree of functionalisation
FWHM	full width at half maximum
GC	gas chromatography
HABA	4'-hydroxy azobenzene-2-carboxylic acid
HEMA	hydroxyethyl methacrylate
HG	hydrogel
IHO	inverse hydrogel opal
IR	infrared spectroscopy
LCST	lower critical solution temperature
LCP	linear copolymer
MEO$_2$MA	di(ethylene glycol)methylether methacrylate
MEOMA	mono(ethylene glycol)methylether methacrylate
NMR	nuclear magnetic resonance spectroscopy
OEGDMA	oligo(ethylene glycol)dimethacrylate
OEGDMA$_{400}$	oligo(ethylene glycol) dimethacrylate M_n =

	400 g mol^{-1}
OEGDMA$_{550}$	oligo(ethylene glycol) dimethacrylate M_n = 550 g mol^{-1}
OEGMA	oligo(ethylene glycol)methacrylate
OEGMA$_{300}$	oligo(ethylene glycol) methylether methacrylate M_n = 300 g mol^{-1}
OEGMA$_{475}$	oligo(ethylene glycol) methylether methacrylate M_n = 475 g mol^{-1}
PAAm	poly(acrylamide)
PBS	phosphate buffered saline
PDI	polydispersity index
PEG	poly(ethylene glycol)
PHEMA	poly(hydroxyethyl methacrylate)
PMMA	poly(methyl methacrylate)
PNiPAam	poly(*N*-isopropylacrylamide)
PP	poly(propylene)
PS	polystyrene
SEC	size exclusion chromatography
SEM	scanning electron microscopy
SP	silica/stoeber particles
SR	swelling raio
T	temperature
TEOS	tetraethyl orthosilicate
THF	tetrahydrofuran
TLC	thin layer chromatography
UCST	upper critical solution temperature
UV	ultra-violet (light)
V-501	4,4’-azobis(4-cyanovaleric acid)
VD	vertical deposition
ε	molar extinction coefficient
λ	wavelength
ϕ	volume fraction
w	(“weight”)/mass fraction
ξ	mesh size

Contents

Acknowledgements **iii**

Abstract **v**

Abbreviations and variables **ix**

1 Introduction **1**
1.1 Structural colour 1
1.2 Opals 3
  1.2.1 Opals as sensors 5
1.3 Objective and outline 6

2 Spherical monodisperse particles and their synthesis **9**
2.1 Selection of material 9
2.2 Introduction to silica particle synthesis 11
2.3 Stöber silica particle synthesis 13
  2.3.1 Nucleation and particle growth 16
  2.3.2 Stability of Stöber particle suspensions 17
  2.3.3 Particle analysis 18
2.4 Synthesised Stöber particles 22

3 Colloidal crystals **27**
3.1 Colloidal crystal assembly 27
  3.1.1 Vertical deposition 29
3.2 Opals and light 33
  3.2.1 Crystal structure in colloidal crystals 33
3.3 Light scattering 34
  3.3.1 Snellius' law 35
  3.3.2 Bragg's law 35
  3.3.3 UV/vis-spectroscopy in reflection mode 36
  3.3.4 UV/vis-spectroscopy in transmission mode 37
3.4 Assembly of SiO_2-based colloidal crystals 38
3.5 Structural elucidation 42
  3.5.1 Scanning electron microscopy of colloidal crystals 42

3.5.2 Atomic force microscopy of colloidal crystals 43
3.6 Interference with Light 45
3.6.1 Transmission UV/Vis spectroscopy of colloid crystals . . . 45
3.6.2 Reflection UV/Vis spectroscopy of colloid crystals 46

4 Thermoresponsive polymers and hydrogels 49
4.1 Theoretical view on thermoresponsive polymers 50
4.1.1 Cloud point determination 55
4.2 Linear HEMA/OEGMA copolymers 58
4.2.1 Synthesis and cloud point determination of linear HEMA/OEGMA copolymers 58
4.3 Cross-linked HEMA/OEGMA hydrogels 62
4.3.1 Synthesis of cross-linked HEMA/OEGMA hydrogels 62
4.3.2 Stability and swelling of HEMA/OEGMA hydrogels 64

5 Inverse hydrogel opals 69
5.1 Creating inverse opals 69
5.2 Synthesis of inverse hydrogel opals 72
5.3 Analysis of inverse hydrogel opals 74
5.3.1 UV/Vis transmission spectroscopy 74
5.3.2 Scanning electron microscopy 79
5.3.3 Calculation of mesh sizes 81
5.4 Functionalisation of inverse hydrogel opals 83
5.4.1 Coupling of HABA-propionate 83
5.4.2 Coupling of biotin 88

6 Summary and conclusion 99

7 Experimental part 103
7.1 Chemicals 103
7.2 Methods 104
7.3 Calculations 108
7.4 Silica nanoparticles and colloid crystals 109
7.4.1 Silica nanoparticle synthesis 109
7.4.2 Colloidal crystal assembly via vertical deposition 109
7.5 Synthesis of polymers 110
7.5.1 Synthesis of linear polymers 110
7.5.2 Synthesis of chemically crosslinked hydrogels 112
7.5.3 Synthesis of inverse hydrogel opals (IHOs) 114
7.5.4 Synthesis of HABA-functionalised hydrogels 114
7.5.5 Biotinylation of IHOs 115

Appendix III

List of Figures VII

List of Tables **XIII**

Bibliography **XV**

Für meine Familie.

1 Introduction

1.1 Structural colour

In nature, structural colour can be found in feathering of several bird species (e.g. pigeons, peacocks and wild ducks), in shell of bugs (e.g. jewel and scarabaeid beetles) as well as in wings of butterflies (mainly male representatives of the Morpho butterfly family).[1–6] The colour is used by these animals for attraction of the other sex, irritation of natural predators or marking of the territory.

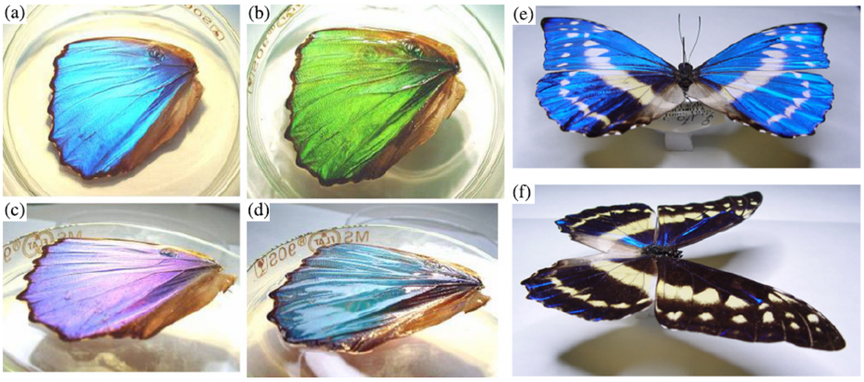

Figure 1.1: Frontal and oblique views of the wing of a butterfly (Morpho didius) (a) and (c) in air and (b) and (d) when immersed into liquid ethanol. Colour change of the wing is observed when the viewing angles are changed, keeping the direction (e) perpendicular and (f) parallel to the wing veins. From [4], used with permission.

The main feature of this structural colour is a bright colourful light reflection, the so-called iridescence, which was found to be depending on viewing angle and surrounding medium (cf. **figure 1.1**). The physical principle behind this phenomenon is the so-called “Brag diffraction” of visible light, which is introduced in detail in **chapter 3**.

In contrast to the excitation of dye molecules, which is another common colour source in nature, materials displaying structural colour rely on the interaction of incoming light with special architectural features. As an example, the wings of Morpho butterfly are shown in more detail in **figure 1.1**.

When looking onto the wing of Morpho didius, a bright blue iridescence is observed with air as a surrounding medium (**figure 1.1** (a)). When the wing is soaked with ethanol, the colour changes from blue to green, accompanied with a decrease in intensity (**figure 1.1** (b)). The reason for this change in colour and intensity is the change in refractive index contrast between the wing material and the surrounding medium ($n_D(EtOH) = 1.359 > n_D(air) \approx 1.0$). The angular dependence of the reflected colour is shown **figure 1.1** (c) and (d) (in air and ethanol (EtOH)), displaying colour changes when the viewing angle is tilted. The same observation can be made, when the butterfly specimen is rotated, while the viewing angle is maintained (**figure 1.1** (c) and (f)).

The source of the iridescence are nanostructured entities in the feathers, shell and wings of these animals. Electron micrographs of butterfly wings display lamellar architectures, which are able to produce Bragg diffraction patterns with incoming light.

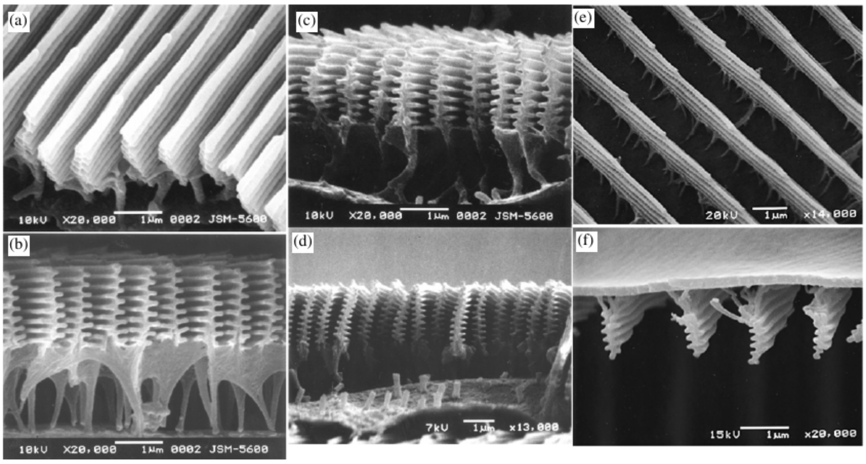

Figure 1.2: SEM micrographs of the lamellar architecture in scales of Morpho didius, M. sulkowskyii and M. rhetenor, observed with various magnifications and angles. From [4], used with permission.

These uniformly oriented lamellae interact with light due a pronounced difference in refractive index between the lamellar material and surrounding air, as mentioned above. The lamellar material diffracts incoming light in such a way, that only a specific wavelength is reflected. This reflected light is observed as the iridescent colour. The wavelength of the reflection and so its colour are determined by the distance in-between the lamellae.

In summary, the prerequisites for Bragg diffraction are the existence of a diffraction grating with a uniform alignment of the diffracting architecture and a sufficient difference in refractive index between the uniformly oriented material and the surrounding medium.

1.2 Opals

Structural colour in nature does not only occur in feathers or shells of animals, but also in a certain type of stones: the opals. Opal gemstones show a similar iridescence like butterfly wings. This iridescence, which is here also called opalescence, is also based on structural colour, yet the internal architecture is different. Instead of lamellar structures, spherical particles are aligned in a uniform fashion, thus forming three-dimensional diffraction gratings.[7–10] These spherical particles are made from crystalline silica, and are surrounded by an amorphous silica matrix (**figure 1.3(b)**). Depending on the intensity of the opalescence and on the colour of the background, cut opal gemstones are sold for prices from tens to several thousand Euros per ounce.[1] This makes certain grades of naturally occurring opals nearly as expensive as diamonds.

Opalescence and the practical use thereof has drawn also increasing interest as a technical application in wave-guides, reflectors or sensors during the last 15 years.[11–14] For this reason, synthetic analogues of natural opals have been developed, which are also called “colloidal crystals” (CC) due to their similarity to crystalline materials.[15–17] Primarily, spherical silica or polymer particles are deposited in a regular orientation, like in **figure 1.3(b)**, and are additionally embedded in a matrix for mechanical support.

---

[1] http://www.opals.info/opalevalguide.php - accessed Oct. 2013

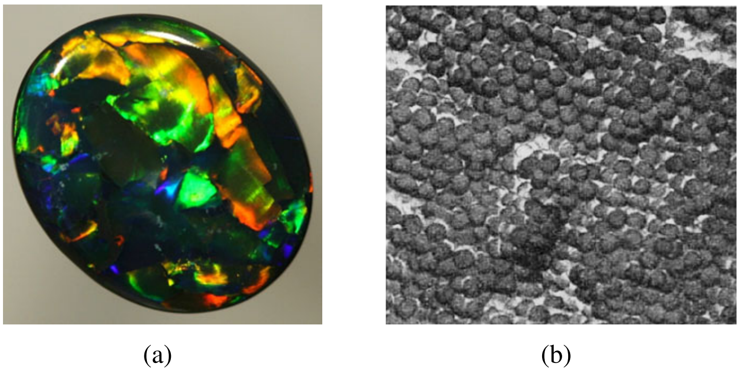

Figure 1.3: a) Naturally found opal, cut as a gemstone, b) SEM micrograph of a natural opal; the amorphous matrix was partly etched with HF (From [8] with permission).

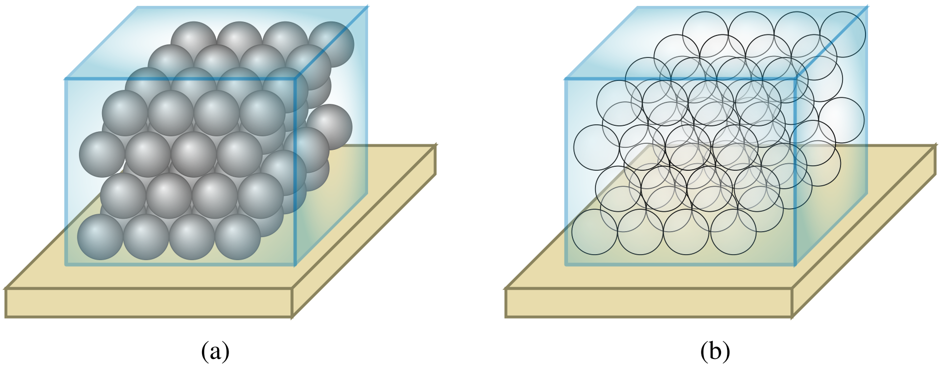

Figure 1.4: Schematic drawing of a) a synthetically made opal in a matrix, b) an inverse opal, where particles were etched and cavities are left.

A derivative of normal opals is obtained, when the template particles are removed after synthesis of the matrix (cf. **figure 1.4**). A porous material with spherical cavities, where the particles used to be, is obtained. Due to the inversion of the structure, these type of opaline materials are called "inverse opals". The optical properties of normal and inverse opals are similar, as long as a refractive index contrast between cavities and matrix is given. Therefore, inverse opals are an alternative to normal synthetic opals or colloidal crystals. Inverse opals also offer advantages due to the porous structure inside of the material.

1.2.1 Opals as sensors

Out of the diverse technical application, which were briefly mentioned above, opals have shown to be particularly versatile for sensing applications.[18] When designing an opaline material as a sensor, the chemical nature of the matrix is chosen in such a way, that their macroscopic structure can be modified by an external stimulus.[2] With a macroscopic change in the matrix, the regular distance between the spherical particles or cavities can be either increased, decreased or the uniform structure can be even destroyed. The latter is an example for a qualitative sensor, which will only visualise the presence of a particular stimulus without quantitative information.

When the distance alteration is distinct enough, the colour, which is reflected by the opaline material, also changes. In summary this means, that the presence of a particular stimulus changes the reflected colour of the opal sensor. This mechanism is visualised in a simplified version in **figure 1.5**. The principle of stimuli-responsive materials and their application in opals will be discussed in more detail in **chapter 4** and **chapter 5**.

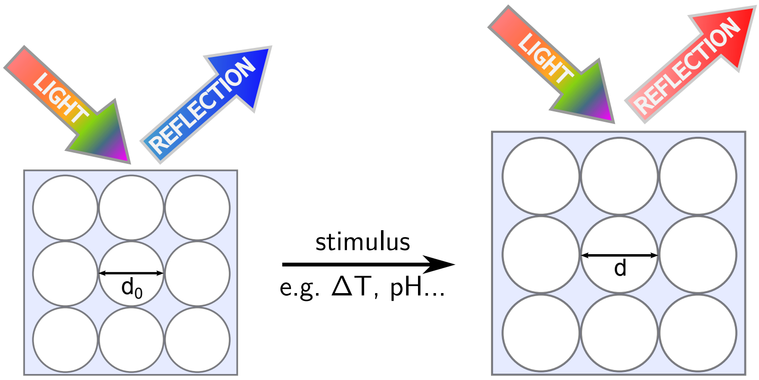

Figure 1.5: Schematic representation of an opal-based sensor subjected to a stimulus, resulting in deformation of the matrix ($d > d_0$) and a change in Bragg diffraction wavelength.

For sensor applications, often cross-linked hydrophilic polymers, so-called hydrogels, are applied as matrix material. In contrast to the silica matrix of the natural opals, hydrogels are soft, non-brittle materials, which are able to react to changes in their environment. This is based on the fact, that hydrogels are able to shrink

---

[2] Shifting of the particle diameter, instead of the matrix, in response to a stimulus is also an applicable approach. As only responsive matrices were used in this work, this principle is not presented in detail.

or swell when the composition of the surrounding medium is changing, a so-called "stimulus" on the hydrogel. The chemical composition of a hydrogel defines, towards which particular stimulus it will be sensitive to.

If e.g. pH-sensitive monomers like acrylic acid are incorporated in the hydrogel network, neutral or alkaline aqueous solutions induce a swelling of the hydrogel, while acidic solutions result in a much lower increase in hydrogel volume.[19–21] This effect is based on the degree of dissociation of the carboxylic acid moieties, which liberates negative charges in the hydrogel. Repulsion of negative charges induces a massive swelling. Therefore, such materials are considered to be pH-sensitive.

This sensitivity can be extended to other stimuli like temperature[22–27], solvent[20, 21, 28–31] or humidity[32–35], but also to presence of specific ions[36–40] or (bio)molecules[14, 41–47] by selecting suitable monomers for the particular sensing task. All the cited examples are applied as matrix material in hydrogel-based opal sensors.

As an example for work in literature on sensing of (bio)-molecules, the Asher group demonstrated an opal-based sensor, consisting of polystyrene (PS) nanoparticles in a poly(acrylamide) (PAAm) matrix, for the quantitive detection of glucose in tear fluid.[14, 48, 49] Specific targeting of glucose molecules was realised with boronic acid derivatives as binding partners. Binding of glucose molecules induced a swelling of the PAAm matrix, inducing a red-shift of the Bragg reflection wavelength, which was observable with the unaided eye.

1.3 Objective and outline

So far, opal-based sensors in literature have been predominantly applied for sensing of small molecules, yet reports on applications for sensing of larger (bio)molecules are rare.[18, 41, 43, 46, 50] In medical diagnostics, proteins are one of the most important compound classes. For this reason, the development of a sensor material for proteins is of high interest.

The aim of this work was the synthesis and characterisation of hydrogel-based opal sensors, which are able to selectively bind protein molecules and visualise this binding event *via* a shift of the reflected wavelength of the opal. This implies that unspecific interactions of the polymer with biomolecules had to be suppressed by choosing suitable non-fouling polymers. To facilitate diffusion of the large protein molecules into the sensor films, inverse opal structures were aspired. When particles of appropriate size are etched, cavities with diameter of several hundreds of nanometres provide enough space for proteins to diffuse into the sensor, if hydrophilic polymers or hydrogels are used as matrix materials. Diffusion of analyte molecules to the inside of the sensor is desired, to ensure a high number of binding events, which increases the sensitivity of the sensor. Moreover, a thermoresponsive polymer matrix was to be explored. Thermoresponsive polymers undergo a reversible phase-transition at a certain temperature, switching the state of the matrix polymer from hydrophilic to hydrophobic (or vice versa). This phase-transition should be induced by the specific binding of the particular protein molecules to the targeting groups, which changes the hydrophilic character of the hydrogel, for amplification of the signal. Last note least, reflection wavelengths of the opals in the visible range were aspired, so that in the optimal case a read-out by the unaided eye would be possible.

The objectives were approached in four steps, which are presented as separate chapters in this work. The theoretical fundamentals are introduced separately for each topic, before the respective practical work is described. **Chapter 2** describes the synthesis and characterisation of spherical silica nanoparticles. The main focus lied on control of the synthesis with the ability to reproduce particle diameters with monodisperse particle size distribution. Such particles were subsequently used for the assembly of colloidal crystals, which is presented in **chapter 3**. A uniform deposition of the particles to obtain colourful opalescence from Bragg diffraction in the visible range was the key objective in this step, monitored *via* UV/Vis spectroscopic characterisation. **Chapter 4** describes the synthesis and thermoresponsive characterisation of linear and cross-linked polymers for the use as matrix material in the sensor. **Chapter 5** shows the combination of colloidal crystals and hydrogels for the preparation of inverse hydrogel opals (IHOs). The obtained structured hydrogel sensors were characterised in terms of their thermoresponsive and optical properties. The chapter describes further the functionalisation of the IHO with a targeting unit, followed by binding tests for the corresponding analyte protein, with regard to the effect on the wavelength of the opalescence.

2 Spherical monodisperse particles and their synthesis

In this chapter, the process of creating uniformly sized spherical particles is explained from material selection to actual one-pot particle synthesis and particle analysis *via* dynamic light scattering (DLS). Such particles were used for the assembly of colloidal crystals (CCs), which is described in the subsequent chapter.

2.1 Selection of material

For the assembly of CCs and the transformation into IHOs, the particle suspension has to fulfil several prerequisites. The high demands on the particle quality are summarised as follows:

1. monodisperse particle size with very narrow size distribution
2. suspension free of impurities
3. sufficiently charged particle surface for electrostatic stabilisation
4. particles have to be dissolvable

Firstly, colloids that are too differently sized, are unable to build up a regular crystal lattice. Space requirements are not equal for all particles and therefore, irregular alignment is the result. Secondly, (ionic) impurities interfere in the electrical double layer, that is present around the (charged) particles.

The double layer around the particles is responsible for two properties: 1. an equally charged surface of the particles prevents a ripening and therefore coagulation of the colloids and 2. charges on the surface account for a short-range repulsion between colloids, when the particles are deposited (for more details see **sections 2.3.2** and **3.1**). With impurities present in the dispersion, either particle stability or deposition regularity might be disturbed. Both can result in defective colloidal crystal deposition.

As the aim of this work was the assembly of IHOs, particles needed to be removable after serving as a template for the inverse opal structure. Therefore, only non-cross-linked polymer particles or inorganic silica particles were considered as an option. The latter, though cross-linked, can be etched with aqueous HF.

Normally, for the application as CCs, scientists almost exclusively choose between two types of particles: polymeric colloids manufactured *via* emulsion polymerisation[51–57] or inorganic silica particles fabricated *via* the Stöber synthesis.[58–64] With both types it is possible to satisfy the demands stated above, but there are some differences concerning synthesis, purification and aftertreatment, which favour one of the two approaches.

Regarding particle formation, both approaches share a similar nucleation and growth mechanism, which is explained in detail in **section 2.3.1**. The main disparities concerning synthesis are mainly the applied chemicals and reaction control in general. The product itself, spherical particles with a certain surface charge in a liquid medium, are obtained with both strategies. Also, size variation can be achieved by varying reagent concentration in both syntheses (for more details see **section 2.3**).

Comparing the ease of purification for both crude suspensions, silica suspensions tend to be much more resilient. SiO_2 suspensions can be easily (ultra) centrifuged to completely exchange the supernatant in short time. This guarantees very pure suspensions, almost free of unreacted reagents or other impurities. As the inorganic SiO_2 particles are very hard, redispersible sediments can be easily separated again after centrifugation by ultrasonic treatment.

The purification of non-cross-linked polymeric colloid dispersions (poly(methyl methacrylate) (PMMA) or polystyrene (PS)) is more demanding. (Ultra)-centrifugation cannot be applied, because polymer particles are softer than SiO_2 spheres and are prone to irreversible coagulation. This, in the best case, impairs the particle size distribution. In the worst case, a redispersion of the colloids is not possible at all. The same issues are valid for freeze-drying, which is an alternative for the removal of liquid impurities.

Therefore, gentler purification techniques like dialysis or ultra filtration have to be used for polymer colloids. Although these are established methods in colloid science, there are also several downsides. First of all, both techniques are rather time-consuming. As dialysis relies on the concentration difference between pure and “contaminated” solvent, it normally takes several days to weeks until a satisfactory purity for the deposition of CCs is reached. Quite often, ion exchange resin has to be added after dialysis to clean the suspension of any residual ionic impurities. Otherwise, even the best size-controlled polymer particles will not self-assemble to CCs due to a disturbance by potential impurities.

Altogether, the primary aim of this work was the design of an IHO, so particle synthesis was used as a tool towards the final target. Therefore, the established robust silica synthesis with its faster and less delicate purification was chosen for preparation of spherical particles. All steps from synthesis to a purified suspension can be conducted in roughly one day’s work.

2.2 Introduction to silica particle synthesis

There are several different ways to produce amorphous colloidal silica particles. In industry, typically two strategies are applied that lead to the formation of colloidal silica:

1. pyrogenic/fumed silica
2. precipitation from water glass

Fumed silica is produced, when silanes (e.g. $SiCl_4$) are burned in an oxygen-rich atmosphere in presence of hydrogen. This synthetic strategy yields particles of $<$ 50 nm with high specific surface areas. Advantage of the process is that only gasses and solids are involved with only gaseous side products. Disadvantages include high energy costs as well as poor control over particle sizes. Though, particle diameters can be adjusted to a certain extent by variation of the reaction parameters like temperature and feed velocities.

The more common approach is precipitation from sodium silicate solutions, which is called *water glass*. Here, the aqueous silicate is precipitated with HCl. This usually forms a gel-like material, which, after dehydration, yields microporous silica particles.

The main drawback of both systems is, that control over shape and size of particles is rather low. This means, that industrial batches of silica particles normally exhibit a rather broad size distribution. As an example, a DLS plot of commercially available Snowtex® ZL silica particles from Nissan Chemical (USA) is shown in **figure 2.1**. These silica particles are manufactured by precipitation from alkaline solution, according to Nissan's product specifications.[3]

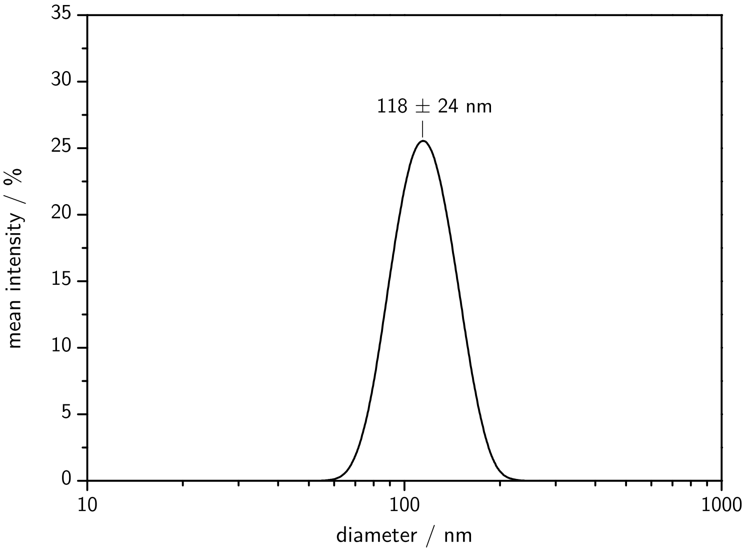

Figure 2.1: Particle size distribution of a commercially available Snowtex® ZL silica batch determined by dynamic light scattering.

From particle size distribution in **figure 2.1** it is evident, that the size distributions of most of the commercially available SiO_2 particles are rather broad. A size deviation of 20 % was determined *via* DLS, which would be too much for the fabrication of CCs, where size deviations not greater than 5 % to 8 % can be tolerated for defined particle assembly.[59]

---

[3] http://www.nissanchem-usa.com/snowtex.php

For the use in CCs, defined particle size and narrow size distribution are essential. Therefore, industrially-made silica particles were not considered suitable for this application, and particles had to be synthesised in a more controlled way.

2.3 Stöber silica particle synthesis

A different synthetic strategy had to be used, which is the silica synthesis developed by the german Werner Stöber and his co-workers.[65] Since its discovery in 1968, the so-called Stöber synthesis is one of the most applied particle synthesis strategies in colloid science. According to the article database "Web of Knowledge" by Thomson Reuters, the article of Stöber *et al.* was cited nearly 5000 times as of this writing.[4]

The Stöber synthesis is driven by the condensation reaction of organoalkoxysilanes in basic aqueous media. Particles produced *via* this approach are often termed after the developer of the synthetic approach: Stöber particles. This does not categorise silica particles in general, but only when the particles were produced of organoalkoxysilanes in water/alcohol mixture, with ammonia as catalyst. Particles produced *via* this route share some characteristics like a certain density, surface charge as well as chemical composition.

$$n\,\mathrm{Si(OC_2H_5)} + 4n\,\mathrm{H_2O} \longrightarrow n\,\mathrm{Si(OH)_4} + 4n\,\mathrm{C_2H_5OH}$$

$$n\,\mathrm{Si(OH)_4} \longrightarrow \mathrm{(SiO_2)}_n + 2n\,\mathrm{H_2O}$$

Figure 2.2: Overall reaction equation of the condensation of tetraethyl orthosilicate in aqueous media.

The simplified overall reaction scheme using the example of tetraethyl orthosilicate (TEOS) is depicted in **figure 2.2**. Here, the typical reaction mixture contains water, ammonia, TEOS and ethanol. While water and ammonia serve as hydrolysing agent/catalyst, ethanol acts as solvent.

It must be mentioned, that the process is not yet understood in full detail, but a large part of it was successfully evaluated, which is presented here.

If we observe the reaction more carefully, as a first step, the organoalkoxysilane is

---

[4] Date of retrieval: 15 October 2013

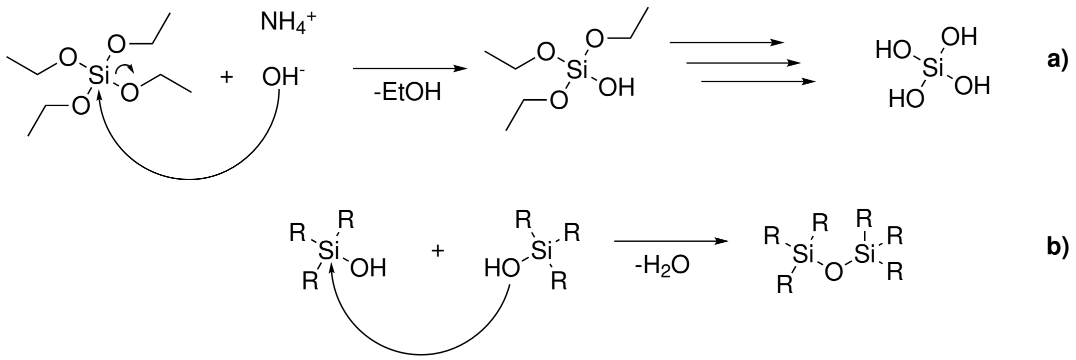

Figure 2.3: Hydrolysis and condensation of tetraethyl orthosilicate in aqueous media.

hydrolysed by OH^- to yield R_3Si-OH, with R either -OH or the respective alcohol as depicted in **figure 2.3 a)**. In the following reaction pathway, the nucleophilic silanol moieties attack another silicon center atom *via* nucleophilic substitution, resulting in a pentavalent transition complex,[66–68] finally introducing -Si-O-Si bonds, that later build up the cross-linked SiO_2 network (cf. **figure 2.3 b)**).

The reaction rate of the Stöber synthesis and therefore also the particle size of the resulting silica spheres is strongly dependent on the concentration of the reaction partners.[66, 69–71] The nucleophile, OH^- is produced by NH_3 and H_2O, the reaction rate increases almost linearly with $[NH_3]$. According to Harris *et al.*[70], the dependence of the rate constant on $[H_2O]$ is even bigger, with a factor of $[NH_3]:[H_2O]^{1.5}$. Overall, the hydrolysis is a first order reaction, as expected. Thus, increasing $[H_2O]$ and $[NH_3]$ results in shorter reaction time and therefore also in larger particle sizes. But there is to notice, that these concentrations of H_2O and NH_3 reach a maximum, after which still fast reaction rates are observed, but particle sizes decrease again.

A similar observation can be made, when [TEOS] is varied. With increasing [TEOS] larger particles are generated, although the increase in particle size is not so distinct as for the other reactants.

Cross-linking occurs eventually when applying base-catalysed synthesis strategy, as the introduction of the more electronegative -OH and -O-Si groups accelerate the upcoming reaction steps. This is because of the stronger withdrawal of electrons from the center Si atom, compared to the alkoxide residues, resulting in a more electron-poor silicon center. Therefore, the electron-poor silicon is a better target for a nucleophilic attack, thus increasing reaction rate.

Difference in electronegativity as well as steric hinderance is the reason why the reaction rate of silicon alkoxides is slower the longer alkyl chains are. For example, tetramethyl orthosilicate is far more reactive than tetrabutyl orthosilicate. TEOS presents a good compromise of moderate reactivity. TEOS allows to control the condensation while still maintaining short reaction times and good control over particle sizes. Due to this, TEOS is the most frequently used organoalkoxysilane for silica particle synthesis.

The acid-catalysed reaction generally proceeds more slowly and does not yield highly cross-linked materials, but normally linear chains and therefore leads to a different microstructure in the final product.[66, 72] Many of these facts are due to the opposite effects of, for example, substituents on silicon or on the stabilisation of the transition state in base- and acid-catalysed reactions. Since only base-catalysed reactions were applied in this work, the acid-catalysed pathway is not discussed in detail.

Apart from the concentration of the reactants, there are also other parameters during the Stöber synthesis, which alter size and quality of the silica particles. First of all, there is temperature, which often plays an important role in chemical reactions. Bogush *et al.* studied the effect of temperature on particle size in the Stöber reaction.[73] They showed, that particle size monotonically decreases with temperature and monodispersity could be achieved for all but the lowest temperature (9 °C in this case). These findings created a rule of thumb, according to which particle size is halved when T is increased by 30 °C.

Another crucial parameter is the addition rate of TEOS. Nozawa *et al.*[74] studied the continuous addition of TEOS feed in contrast to seeded-growth techniques, which are often used for the creation of particles larger than 1 µm. They were successful in creating particles close to 2 µm with very slow TEOS addition rates (0.005 mL min^{-1}), while speeding up the process (0.5 mL min^{-1}) yielded particles of around 600 nm. This shows, that the feed rate is crucial factor in silica particle synthesis. Since often this information is either vague or not given in literature procedures, it is hard to reproduce the exact results of other researchers.

Altogether, the Stöber reaction proved over several decades to be a very versatile reaction, when it comes to the creation of spherical silica particles in the range from nanometres to several micrometres. Yet, the outcome of the synthesis is very sensitive

Table 2.1: Summary of the influence of several reaction parameters on SiO_2 particle size in Stöber synthesis.

influence on/increase in	T	$[NH_3]$	$[H_2O]$	[TEOS]	addition velocity
particle diameter	↓	$\uparrow^a$	$\uparrow^a$	↑	↓

[a] until maximum is reached

towards reagent concentrations and process parameters. Therefore, protocols have to be followed very precisely, to obtain reproducible results.

2.3.1 Nucleation and particle growth

One of the questions, that always arises in colloid particle synthesis, is: why are the particles so well defined in size? When Stöber particle synthesis is performed in a very controlled way, particles of defined diameter with a narrow size distribution ($\sigma \leq 5\%$) are obtained. Several research groups have tried to elucidate the particle growth mechanism. Applying various analytical methods, several different theories were postulated. As the nucleation and growth mechanism is a very important aspect in particle synthesis, the next sections give a short overview over the findings reported in literature.

2.3.1.1 LaMer model

The research group around Harris[69, 70] concluded that the Stöber system obeyes La Mer's homogeneous nucleation and growth model[75].

The LaMer model is one of the oldest models to describe synthesis of uniformly sized particles in colloid science. In the 1940s and 1950s, the American chemist Victor LaMer and his co-workers studied the generation of molecularly dissolved sulphur by precipitation reaction of sodium thiosulphate in dilute hydrochloric acid.[75] Similar to the Stöber reaction, he observed that the production of colloidal sulphur can be split into three parts: hydrolysis, nucleation and growth.

In the Stöber reaction, during hydrolysis the silicon alkoxide (e.g. TEOS) is converted to silicic acid, the monomer used for condensation into particles, as described earlier. This slow hydrolysis increases the concentration of silicic acid until a critical concentration is reached, at which nucleation occurs (i.e. the condensation of silicic acid into very small particles). The nucleation itself consumes silicic acid and therefore obviously lowers its concentration below the critical concentration. After this, the number of nuclei stays constant during the subsequent growth period. Here, the remaining silicic acid monomer is consumed by the present particles, which grow in size as long as there is still monomer present in the reaction solution. Monodispersity is always achieved, if the nucleation period is short enough, so that no new nuclei are produced during the remaining reaction time. Harris *et al.* showed this, as they only received polydisperse samples, when the concentration of silicic acid was kept above the critical concentration throughout longer periods of the reaction.

2.3.1.2 Other models

Bogush and co-workers[73] investigated the Stöber synthesis using electron microscopy, conductivity measurements, and the (small) change in reaction medium volume. They concluded that all TEOS hydrolyses completely in the first few minutes, and that the Stöber silica particles are formed through a size-dependent, controlled, coagulative nucleation and growth mechanism. They postulated that nucleation from extremely supersaturated solutions continued almost to the point at which the particles reached their final size. In the beginning of the reaction, small unstable particles aggregate until a critical size is reached, at which the probability of two particles of equal size sticking together becomes negligible. Homogeneous nucleation still continues, and the freshly formed small particles are taken up by the large stable particles that now remain constant in number. Classical nucleation expressions were used to estimate nucleation rates per unit volume.[76] Their proposed size-dependent nucleation–aggregation mechanism is analogous to a similar model developed to explain the emulsion polymerization of styrene.[77]

2.3.2 Stability of Stöber particle suspensions

Suspension stability is a common problem for metastable colloids. If particles are not sufficiently stabilised, they will aggregate to bigger agglomerates, a process called

"Ostwald-ripening", which was first described by Wilhelm Ostwald in 1896.[78]

Briefly, this spontaneous process is thermodynamically-driven, as larger particles are simply more stable than small ones. This is due to the fact, that molecules on the surface are energetically less favoured than molecules in the interior.

Considering the forces involved in this process, Hamaker concluded[79] that it's mainly Van-der-Waal's forces which are responsible for the attraction of spherical particles in a liquid and that in this case, particles are always attracted by each other.

To avoid that monodisperse particles agglomerate over time, they have to be stabilised in some way. In case of the Stöber particles, as well as in many other synthetic approaches towards stable colloids, charges are introduced at the particle surface. This ensures the repulsion of equally charged particles and therefore prevents them from coming close together, which would be the first step of the ripening process.

Here it is beneficial, that charges are already created during the Stöber synthesis. Namely deprotonated silanol groups are present in vast number on the surface of the particles, which stabilise the particles in water and ethanol.[80]

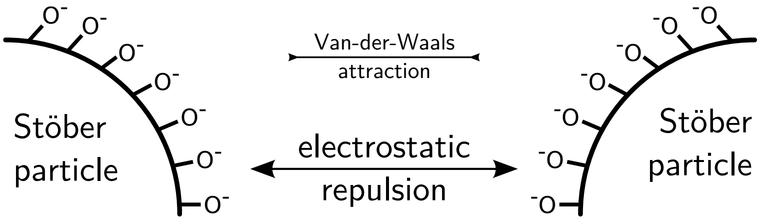

Figure 2.4: Simplified interaction scheme of two Stöber silica particles.

As long as the charges are not screened, e.g. by addition of strong salts or mixing with non-polar solvents (cf. Kiraly et al.[80]), Stöber particle suspensions are stable over a long time scale.

2.3.3 Particle analysis

2.3.3.1 Conversion

After synthesis is conducted successfully, particles have to be analysed. As in any other chemical reaction, conversion is one of the first parameters, which should be determined. In a standard organic reaction, spectroscopic methods like nuclear magnetic resonance spectroscopy (NMR) or gas chromatography (GC) can be applied, or thin layer chromatography (TLC) to see, if all reagents have been consumed.

In Stöber synthesis it is convenient that a solid is created out of only liquid reagents. This results on the one hand in facile separation of solid and liquid *via* (ultra) centrifugation, and on the other hand enables easy determination of reaction conversion *via* solid content measurement. Briefly, a sample of the crude reaction mixture is taken and weighted. Subsequently, the liquid is evaporated and the mass of the dry residue is determined. This solid content is divided by the theoretical solid content at 100 % conversion to give the actual conversion in percent.

$$conversion = \frac{m(SiO_2)_{dry}}{m(SiO_2)_{theo}} \tag{2.1}$$

For more automated procedure, this can be done on a special solid content balance which automates the drying and weighing steps as well as documentation. In this work, an automatic Moisture Analyser from Sartorius (Germany) was used.

2.3.3.2 Particle size and size distribution

The most characteristic properties of colloidal particles are their size, size distribution and shape. These parameters are of special importance, when particles are to be used for CC assembly later-on, as it was targeted in this work. When particle sizes deviate too much from what can be used for Bragg diffraction in the visible range, or if their size distribution is too broad, they are of no practical use for CC assembly (cf. **section 3.1**).

Therefore, particle diameters and size distribution have to be well controlled and verified. For fast and robust particle size analysis, dynamic light scattering (DLS) is a good choice. Here, particle size is determined indirectly, over its correlation with diffusion due to Brownian motion in a known medium.[81, 82] More precisely, not particle size but hydrodynamic radius is the physical quantity, which is determined in this kind of scattering experiment. The relation of diffusion coefficient and hydrodynamic radius is defined in the *Stokes-Einstein-Equation*:

$$D = \frac{k_B T}{6\pi\eta R_0} \tag{2.2}$$

with D the diffusion coefficient, k_B the Boltzmann constant, T the temperature, η the viscosity of the medium and R_0 the hydrodynamic radius. When temperature and viscosity of the solvent are known, D and R_0 are the only unknown quantities. Thus, D has to be determined with the DLS experiment. This can be done by illuminating the sample with laser light of a defined wavelength. For detailed literature about DLS, consult the references.[83–86]

The particles in solution will scatter the laser light according to Rayleigh or Mie scattering (depending on the particle size). As the particles travel through the solution, the scattering intensity fluctuates as light source and detector are fixed at a certain angle. This fluctuation is caused by the Brownian motion of the particles, as the distance between particles, light source and detector changes when the particles move away from or to the light source/detector unit.

The change in scattering path length results in either constructive or destructive interference of light scattered at particles, which either increases or decreases the scattering intensity at the detector. So this is an effect caused by different moving speeds of particles, which is proportional to their size, which was shown above in **equation 2.2**.

To be able now to transform the measured scattering intensity fluctuations to particle size and size distribution, a digital auto correlator with a certain correlation function has to be applied. Here, scattering intensity I at time t is compared with the scattering intensity at later point, $t+\tau$, which is expressed in the following correlation function $G(\tau)$:

$$G(\tau) =< I(t)\, I(t+\tau) > \tag{2.3}$$

For a large number of monodisperse particles in a sample, this correlation function becomes

$$G(\tau) = A[1 + B\, exp(-2\Gamma\tau)] \tag{2.4}$$

with A the baseline of the correlation function, B the intercept of the correlation function and τ the correlator time delay. Γ is given as

$$\Gamma = Dq^2 \tag{2.5}$$

with D the diffusion coefficient and

$$q = \frac{4\pi n_D}{\lambda_0}\, sin\frac{\theta}{2} \tag{2.6}$$

with n_D the refractive index of the medium, λ_0 the wavelength of the laser and θ the scattering angle.

As all parameters in **equation 2.6** are known, with Γ being determined by the correlation function, D can be finally calculated. Since several particles with more or less different size are present in the solution, calculation of D and therefore R_0 becomes somewhat difficult again. For this reason, several different algorithms have been developed and are applied to yield a particle size distribution, which is obtained by splitting the different particle sizes into suitable size classes.

Nevertheless, DLS analysis has some advantages over other methods, most of all, its fast operation principle and its robustness. Especially in back-scattering mode, a broad range of sample concentrations can be tolerated and analysed in short time, making it also cost efficient. Only in more advanced systems, if non-common solvents or solvent mixtures are used, parameters like viscosity and refractive of the liquid have to be determined first, as those are needed to correlate diffusion rate with particle size (cf. **equation 2.6**). For standard systems, these parameters are either supplied by the measuring software or can be looked up in a textbook.

For particles with a charged surface, which is the case for Stöber particles, the hydrodynamic radius is usually bigger than the actual particle size due to the solvate shell around the particle surface. This lowers the diffusion velocity and therefore the particles might appear bigger, as they actually are. Therefore, particle sizes have to be double-checked with another technique, e.g. imaging methods like electron microscopy.

2.4 Synthesised Stöber particles

A variety of silica particles were synthesised following the method developed by Stöber *et al.*[65], which was introduced before in **section 2.3**. For simplicity, all syntheses were conducted as one-pot reactions with TEOS as silicon donor, ammonia as a base and anhydrous ethanol as the solvent.

The aim was to create monodisperse particles with a diameter of about 400 nm. This size is more or less the upper limit for CCs, which still reflect light in the visible region (see **section 3.1** for more details). Also, since inverse/hollow opals with the possibility for penetration of bigger molecules were targeted, the bigger the particles, the more space there will be in the hollow system for molecule diffusion. Therefore, recipes in literature were preferentially chosen, which reported to yield particles in the range of 400 nm.

Though, reproduction of given recipes is not as straight-forward as one might imagine. The influence of different parameters on the Stöber reaction was already mentioned in **section 2.3**. In practice this means, that not only the correct amount of all reagents has to be used, but already small deviations in the protocol, like a different addition rate of the TEOS part lead to completely different particle sizes and particle size distributions. If no additional dosage equipment like a syringe pump or a dropping funnel is used to dispense the TEOS solution, where addition velocity is quantifiable, it can be quite difficult to reproduce the results. Furthermore, often addition rate is not given at all in publications, and therefore, formulations have to be tested and adjusted so that the particles meet the desired criteria in the end.

To visualise the impact of different addition speeds, two different batches of silica particles, which were synthesised with the exact same composition of reagents but with different addition velocities, are shown in **figure 2.5**.

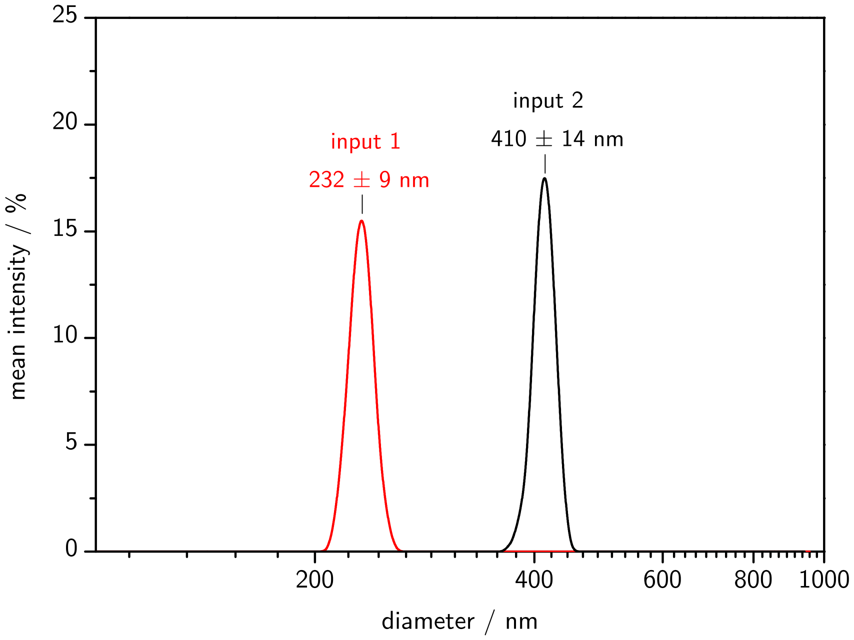

Figure 2.5: Size distribution graphs of two synthesised Stöber silica particle batches; prepared with identical recipes except for different addition speed.

In detail, for input 2 the solution comprising of TEOS and EtOH (131 mL in total) was added "at once" to a water/ammonia solution after equilibration temperature was reached. While for input 1, the exact same solution was added over an interval of two to three minutes, which corresponds to an addition velocity of about 33 to 50 mL min^{-1}. With slower addition velocity, smaller particles are produced. In this case, the slower addition velocity led to a reduction in size by half.

This contradicts the study of Nozawa *et al.*[74], which was presented in **section 2.3**. During their study, slower addition velocities led to larger particles. Yet, there is to note, that in general much slower addition velocities and also different concentrations of the reagents were used, which makes it hard to compare the results. In the case of Nozawa *et. al*, the very slow addition of TEOS only leads to constant particle growth, as nucleation takes place very early in the reaction.

This is not the case in this example, as nucleation might still not have finished as TEOS addition took place. This shows, how difficult it is to predict particle size in this type of reaction in general, although it is known for a long time and was already widely applied in colloid science.

By varying the concentration of the reaction partners, monodisperse spherical silica particles with diameters from 100 to 620 nm were obtained, according to DLS measurements. Details on the particles sizes are given later in **table 2.3**.

Table 2.2: Reaction parameters for the syntheses of selected SiO_2 particles.[a]

entry	T / °C	[TEOS] / mol L^{-1}	[NH_3] / mol L^{-1}	[H_2O] / mol L^{-1}
SP-1	35	seeded growth with multiple addition steps		
SP-2	30	0.06	2.75	18.0
SP-3	30	0.12	4.33	13.8
SP-4	30	0.08	2.51	10.4
SP-5	25	0.17	1.00	7.55

[a] Sorted by ascending particle size (cf. 2.6).

The entries in **table 2.2** are only a selection from the numerously synthesised silica particles during this work. The purpose of this representation is to visualise the diverse particle sizes with a narrow size distribution, which could be obtained with these recipes. As methodical studies correlating reagent concentration with particle sizes are available in vast number in literature, the focus was set on suitable particle size and narrow size distribution.

The different recipes for single-pot silica particle syntheses were taken from literature and applied as needed.[61, 65, 73, 87] With the exception of particles **SP-1**, which were produced by a seeded-growth approach, reagent addition was performed in one single step.

All particles were synthesised in one-pot experiments with direct addition of the complete amount of TEOS to a flask containing the aqueous ammonia solution, set at the respective temperature. In several cases particle sizes deviated from what was reported in literature. Possible reasons for this were already introduced earlier, in particular that in many publications the exact timing of the addition protocol is not given, and therefore the reaction cannot be reproduced precisely.

The conversion was determined after reaction times of at least four hours *via* solid content measurements, which typically gave results >90 %. This value is typical for Stöber reactions, as this reaction is rather fast and irreversible. The deviation from complete conversion originates at least in parts from coarse precipitates which settle at the bottom of the flask. Therefore a small part of the produced SiO_2 is not gathered for the solid content measurement, thus reduceing the calculated conversion.

The purification of the dispersions, which is a key step when aiming at CC assembly, was performed *via* (ultra)-centrifugation. In several cycles, particles were sedimented, washed with anhydrous EtOH and re-dispersed *via* ultrasonic treatment. In the end, dispersions were concentrated/diluted to useful amounts of $w(SiO_2) \approx 0.1$.

After at least six cycles of centrifugation and re-dispersion, particle diameter and quality were analysed *via* DLS. For details concerning the DLS instrument and measurement procedure consult the experimental part.

Table 2.3: DLS data of selected SiO_2 particles.

entry	d_m / nm	σ_{abs} / nm	σ_{rel} / %	FWHM / nm
SP-1	100	4.9	4.9	11.5
SP-2	250	9.3	3.7	21.9
SP-3	410	13.8	3.4	32.6
SP-4	490	12.0	2.5	28.3
SP-5	620	14.7	2.4	34.6

The synthesised SiO_2 particle dispersions presented here showed a sufficiently narrow particle size distribution (cf. **table 2.3**) according to DLS data. This is one important, if not the most crucial parameter when it comes to CC assembly. The upper deviation limit for monodispersely sized particles to be used for CCs is regarded to be approx. 8 % of total particle diameter[59], which is met by all synthesised particles which are presented here. If Stöber reactions are well controlled, narrowly distributed particle sizes are normally obtained in the size range, which was dealt with in this work.

Regarding the size distribution plots depicted in **figure 2.6** and the relative size deviation σ_{rel} from **table 2.3**, particular from the latter it can be seen, that the larger the particles, the narrower their relative size distribution. This fact is based on simple statistics, as the absolute size deviation is comparable in all samples (5 to 15 nm), the relative deviation becomes smaller with larger particles size (cf. **table 2.3**). This process is called self-sharpening and is based on the particle growth mechanism.

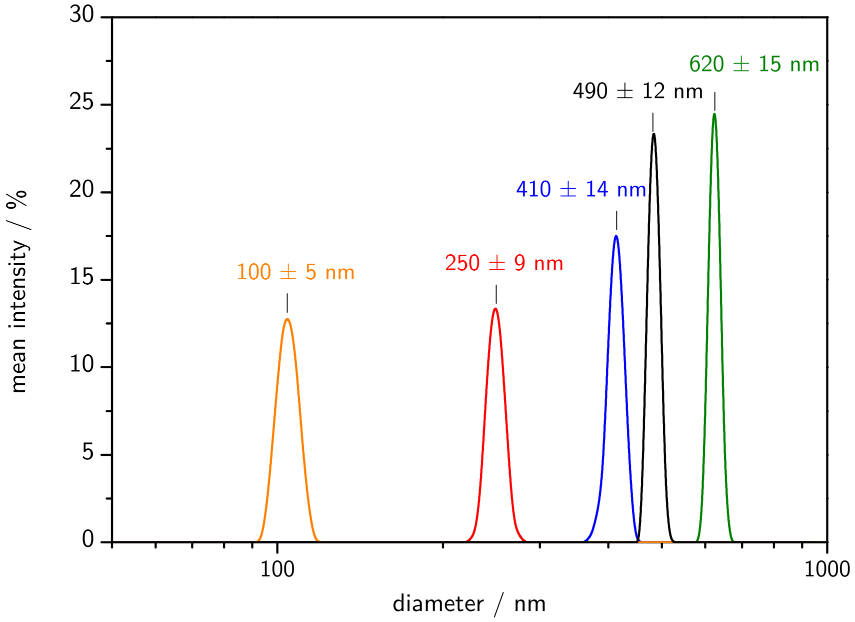

Figure 2.6: Size distribution graphs of the synthesised Stöber particles.

Nevertheless, not all particle samples were considered suitable for the purpose of preparing a CC (and later transformed to an inverse opal) for possible bio-medical sensing. On the one hand, the particles should be as large as possible, so that the pore size of an inverse opal would be wide enough to facilitate diffusion of larger bio-medical species like enzymes, viruses or bacteria. On the other hand, particles with a diameter above 500 to 600 nm are too large for two different reasons.

The first reason is of theoretical nature, regarding Bragg diffraction as such. CCs composed of particles above a certain diameter diffract light of longer wavelengths (e.g. infra-red light) and therefore will not reflect visible light, but only invisible infra-red light.[56] Yet, for a material which should permit readout by eye, reflection of light in the visible range is desired.

The second reason for not using too large particles for CC assembly is more of practical reason when it comes to assembly as such. Obviously, large particles sediment faster than small ones (especially in low-density liquids like ethanol), which depletes them from the surface of the suspension. This renders it difficult or even impossible to deposit the particles in a regular manner as a CC (cf. **chapter 3**). Therefore, particles with a mean diameter of about 400 nm were selected for further experiments in CC assembly.

3 Colloidal crystals

In this work, colloidal crystals are intended to be used as a template for the fabrication of inverse hydrogel opals. Colloidal crystals are a special kind of material, which posses unique optical properties as a result of near- and long-range order of nanoparticles. This orientation can be accomplished with various techniques.[59, 88–90] If the parameters are correctly set, structures with crystal-like arrangement are formed by self-assembly.[91] The evaluation of suitable conditions and parameters for the assembly is the difficult step in the process. A prerequisite for successful colloidal crystal fabrication with any of the established techniques is sufficient particle quality.[59] The specific requirements on particle quality were already mentioned in **chapter 2**, in summary they were mainly of defined particle size with a narrow size distribution.

To provide an overview over existing approaches to create colloidal crystals, various assembly methods as well as parameters which influence the assembly are presented in the following section.

3.1 Colloidal crystal assembly

Nearly all of the so-far reported assembly methods for colloidal crystals share one characteristic: a force of certain strength is applied to the particles, though their crystallisation is also characterised by a spontaneous character.

The spontaneous character is caused by two counteracting inter-particle forces: long-range attraction and short-range repulsion. These effects were already introduced in **section 2.3.2**, where the stability of Stöber suspensions was discussed. The long-range attraction is attributed to the thermodynamical endeavour to minimise the surface energy of the system, which pulls the particles together (Ostwald ripening). The actual agglomeration of the particles is prevented by the charges on the surface, which cause short-range electrostatic repulsion.

This means, that in principle the particles tend to be as close together as possible but the repulsive forces keep the colloids at a certain distance to each other. This is the basis for stabilising colloidal suspensions or emulsions of various kinds.

Concerning the different assembly methods and forces, that have to be introduced to crystallise the silica particles, the most widely applied force is gravitational force. The easiest way to observe this, is to leave an ethanolic silica particle suspension standing for several days/weeks. Due to the gravitational force and the pronounced difference in density between silica and ethanol, silica colloids in ethanol will settle on the ground of the flask over time, exhibiting opalescent colours (cf. **figure 3.1**).

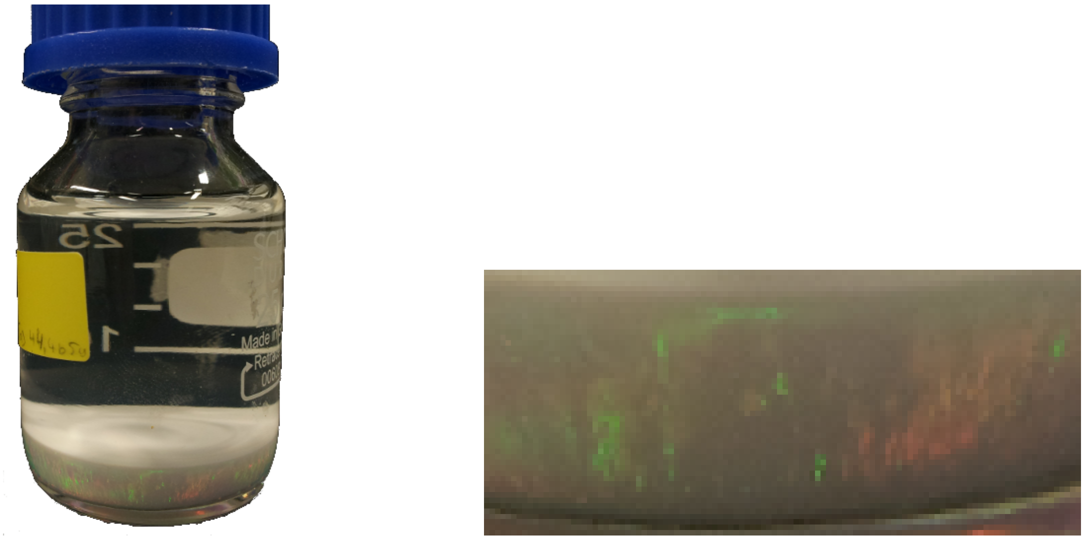

(a)

(b)

Figure 3.1: a) Silica particles sedimented from ethanol suspension, b) magnification of the iridescent light interference in sedimented silica layer.

As it is generally not very convenient to wait several days until the particles are crystallised,[92] scientists exerted stronger external forces to speed up the process and to crystallise particles onto selected substrates. A selection of various methods that have already been used successfully for particle crystallisation, is given in the next sections, starting with the most commonly used approach: vertical deposition (VD).

3.1.1 Vertical deposition

One of the most frequently used colloidal crystal assembly methods is the so-called “vertical deposition” (VD).[59] Here, the desired substrate is placed vertically in a flask filled with the particle suspension, as shown in **figure 3.2**. As the solvent evaporates, the particles gather at the line, where the meniscus of the liquid touches the substrate. With elapsing time, the particles are deposited onto the substrate as a dry film.

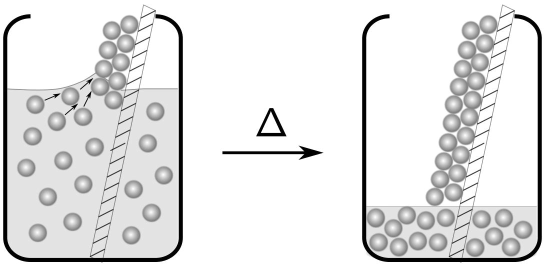

Figure 3.2: Scheme of the vertical deposition procedure

The deposition of colloids *via* the VD technique is driven by capillary forces and convex flow, induced by fast solvent evaporation at the meniscus.[93] If the parameters like temperature, solvent, particle concentration as well as particle size and size distribution are well-matched, then regular particle arrays with a dimension of several square centimetres can be produced by this method. Preferentially, the particles are closely packed,[59] though deviations are also documented.[53]

The main advantage of the VD process is the relative simple execution of the deposition experiment compared to other colloidal crystal assembly methods. Here, the desired substrate is placed vertically in the particle suspension and the solvent is subsequently evaporated.[51, 53–56, 58, 59] Alternatingly, the substrate is drawn out of solution,[52, 57, 94] or the suspension is drained from the vessel[93] to deposit the particles onto the substrate in a regular fashion.

The process can be used with various types of spherical particles. Mostly, spherical colloids either composed of PS, PMMA and their copolymers,[51–57] or silica particles[58–64] have been applied in VD experiments to form colloidal crystals. Recently, successful deposition was also reported for non-spherical particles,[95] but this part of research is still in the beginning as it is much more difficult to crystallise non spherical particles. This is partly attributed to the fact, that it is already quite difficult to synthesise monodisperse non-spherical particles, as this is not generally the energetically favoured geometry.

With vertical deposition, it is possible to use a variety of substrates, including regular glass slides. This ensures for an inexpensive and robust substrate, but also a substrate which is penetrable for UV-light, at least in the UV-A region, which will be important for analysis as well as for polymerisation of matrix polymer later on. Glass also permits to release the matrix polymer film after polymerisation, when it is treated with aqueous HF.

Glass slides are not only easy to handle and to clean, they also offer a very even surface, which is beneficial for deposition as well as for reproducibility reasons. Silicon wafers offer a comparably even surface and would allow surface etching with HF, but due to the higher price and the brittleness of silicon, this material was considered a less suitable substrate. In fact, silicon has been very rarely used in literature so far, presumably due to the given drawbacks, except for when spin-coating is used for colloidal crystal assembly.[88]

The main drawback of the VD approach is the limit in dimensions of the final colloidal crystals. Normally, the size is restricted to several square centimetres. This is an inherent problem of the experimental setup itself, which has not been fully overcome since VD was developed in the late 1990s. This appears to be the main reason, why the commercial application of colloidal crystals is very limited so far.

One of the reasons for the size restriction experimentally encountered, is that depending on the particle size and density of the liquid, the particles start to sediment and therefore move away from the surface of the liquid phase, where the deposition occurs. As there are less particles at the surface, the deposited colloidal crystal obviously becomes thinner, until crystallisation finally stops, simply because there are not enough particles to be deposited.

Unfortunately, this issue cannot be overcome by speeding up the deposition. High deposition rates induce defects in the CCs because there is not enough time for the crystallisation to equilibrate in the close-packing.[51] In general, in every VD experiment, a certain degree of defects cannot be avoided, regardless of how narrow the particle size distribution is. Slightly bigger or smaller particles, that are built into the crystal lattice, induce a change in crystal orientation and therefore a defect in the crystal structure, as illustrated in **figure 3.3**.

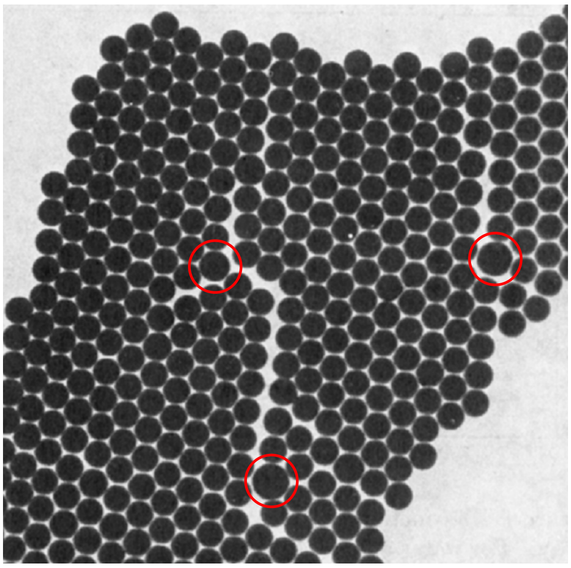

Figure 3.3: Electron micrograph of a colloid crystal consisting of PS colloids. Particles marked in red are non-uniformly sized, causing defects in the crystal structure. Reprinted (adapted) with permission from P. A. Hiltner et al., *The Journal of Physical Chemistry* **1971**, *75*, 1881–1886. Copyright 1971 American Chemical Society.

The particle deposition process is influenced by several parameters, with which it is possible to tune the assembly in a certain margin. Main parameters influencing the VD procedure are temperature, composition of the liquid phase, as well as particle size, quality and concentration. The first two parameters mainly influence the evaporation rate of the liquid and therefore the velocity of deposition. As discussed above, a too high evaporation rate leads to irregular and therefore amorphous particle deposition, while too slow evaporation rates might result in a sedimentation of particles.

With the variation of particle concentration, the outcome is rather similar to temperature variation. High particle concentration produces thicker layers with a propensity to become amorphous, while low concentrations normally result in very thin layers, potentially irregularly oriented (cf. particle sedimentation). Particle size and quality are key factors in all CC assembly methods.

For a successful VD experiment, parameters have to be thoroughly examined and adjusted until suitable combinations are determined. Despite weaknesses, VD is a CC assembly method that shows good compromise between relatively easy setup and satisfactory outcome. Hence, this method was applied in this work, as the aim was not to develop a new method, but to apply an established principle to develop a new material.

3.1.1.1 Various other assembly methods

Apart from VD, various other methods to crystallise colloids have evolved. Some of them tried to overcome the drawbacks of VD for creating larger colloidal crystals. Other methods came up, because they were either giving access to crystallisation of particles that could not be crystallised *via* VD, or because more perfect crystalline structures could be prepared. The presented methods are only exemplary, as scientist have been rather creative in generating new crystallisation methods over the years.

Colloidal crystallisation *via* centrifugation can be considered a more rapid approach to self-assembly *via* sedimentation that was discussed above. Here, particles are deposited in a regular array by controlling initial particle concentration as well as centrifugation speed and time.[96–99] With increasing gravitational force, particles are forced into a regular array.

A similar outer force procedure is achieved *via* spin coating. Here, particle suspensions with a stabilising matrix material are rotated on a silicon wafer to yield brilliantly coloured colloidal crystal materials over an area over $100\,\mathrm{cm}^2$ within minutes.[88, 100] However, it is not possible to spin coat particle suspensions without a matrix monomer, because the viscosity of the solvent is too low and the pure solvent would evaporate to quickly. Therefore the particles would not have enough time to settle regularly. Important parameters to tune crystallisation are viscosity of the medium as well as rotation speed and time.

With similar prerequisites concerning viscosity and stabilisation with matrix monomer, another crystallisation technique was developed: doctor blade coating.[34, 89] Here, a doctor blade is moved horizontally parallel to the substrate, while the particle/monomer suspension is spread in even film thickness. With this technique it is theoretically possible to create much larger crystals than with the other techniques, making it more interesting towards industrial applications.

However, none of the presented methods suits universally for all applications. In any technique, the parameters of deposition have to be set very precisely and all techniques have their weaknesses and strengths. Therefore various techniques were developed, which are all suitable for certain applications.

3.2 Opals and light

In the following section, the crystal structure in CCs is discussed. Optical effects are discussed based on fundamental theory.

Note: all angles given in this work refer to the angle between material surface and light beam.

3.2.1 Crystal structure in colloidal crystals

When particles are assembled into a CC, a face-centred-cubic (fcc) lattice is formed, which is depicted in **figure 3.4(a)**. The most important crystal planes for CCs are the four $(1\,1\,1)$ planes, lying perpendicular to the space diagonal. The $(2\,2\,0)$ and $(2\,0\,0)$ are also optically active in CCs, but are much less important.

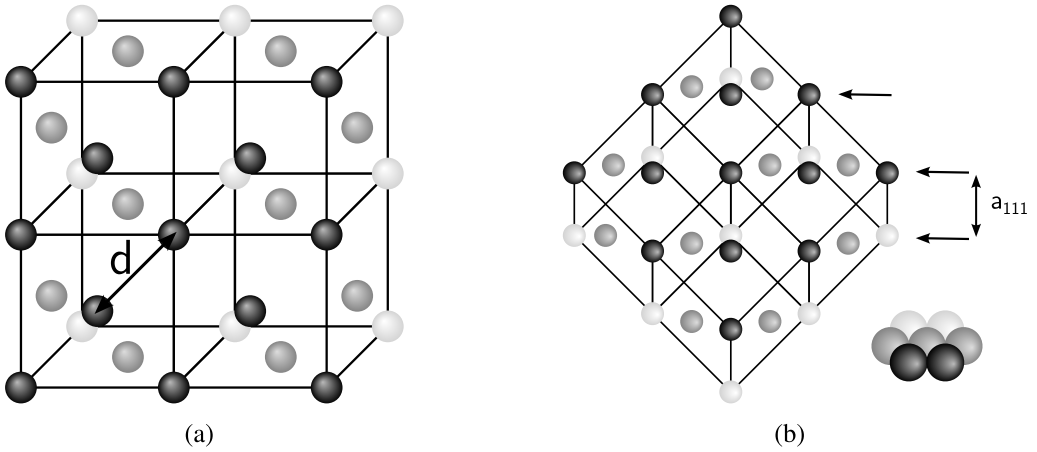

(a) (b)

Figure 3.4: Crystal structure in opal layers a) common crystal representation; b) crystal orientation in horizontal opal films.

In a horizontal opal, the lattice is aligned as shown in **figure 3.4(b)**. Here, the $(1\,1\,1)$ planes are parallel to the surface. In this orientation, the colloid spheres form closely-packed hexagons with a distance d relative to each other.

In **figure 3.4(b)**, the lattice constant a_{111}, which is the distance between two planes of the $(1\,1\,1)$ family, is indicated. In an fcc lattice, a_{111} is defined as

$$a_{111} = d\sqrt{\frac{2}{3}} \tag{3.1}$$

with d the diameter of the assembled spherical particles.

The other (hkl) planes in opal layers are oriented in angles φ_{hkl} and with lattice constants of a_{hkl}, calculated in the following way

$$cos\varphi = \frac{h+k+l}{\sqrt{3(h^2+k^2+l^2)}} \qquad a_{hkl} = d\sqrt{\frac{2}{h^2+k^2+l^2}} \tag{3.2}$$

As mentioned earlier, planes other than $(1\,1\,1)$ play a less distinct role for Bragg diffraction.

3.3 Light scattering

Light is reflected and diffracted at all dielectric surfaces, while in the inner part of most non-ordered films light is scattered more or less diffusely. For opal layers this behaviour is different. Here, another effect is added, which dominates the light scattering: light is diffracted in a regular fashion at the crystal lattice planes.

For light diffraction and reflection, fundamental theories were postulated by Snellius, Fresnel[5] and Bragg. The applicability of these theories for CCs with a moderate refractive index contrast ($\Delta n < 0,5$) has been proven in earlier works.[91, 101, 102]

---

[5] Fresnel's law describes reflection of light at glancing surfaces. As glance has not been studied in this work, his theory is not discussed in detail.

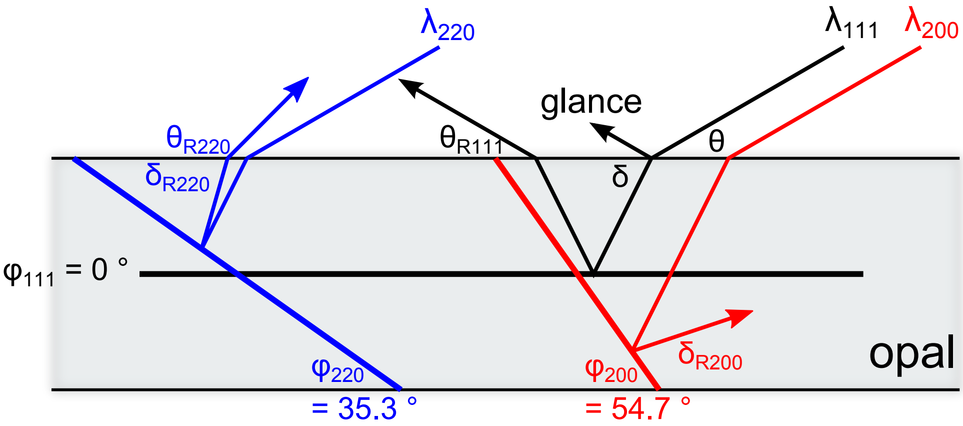

Figure 3.5: Optical pathways of light beams λ_{hkl} in an opal lattice at an angle of incidence of $\theta = 30°$. Diffraction is illustrated at the lattice planes $(1\,1\,1)$ (black), $(2\,0\,0)$ (red) and $(2\,2\,0)$ (blue) visualising the final direction of the refracted light beams (adapted from [103]).

3.3.1 Snellius' law

When light travels through media with different refractive indices, it gets refracted at the interface of both materials. The angle δ, under which light travels inside of the opal, is described by Snellius' law.

This correlation is illustrated in **figure 3.5**. The refractive angle δ follows from the angle of incidence θ and the refractive index n. For colloidal crystals, being non homogeneous materials, a volume-based approximation is generally accepted.[91, 104]

$$\cos\delta = \frac{\cos\theta}{n} \qquad n = \sum \phi_i n_i \tag{3.3}$$

3.3.2 Bragg's law

When light hits the surface of an opal with the wavelength λ at conditions satisfying Bragg's law,

$$m\lambda = 2n\, a_{hkl}\, sin(\varphi_{hkl} + \delta) \tag{3.4}$$

the light is diffracted at the $(h\,k\,l)$ planes and redirected to the angles δ_{Rhkl}, which are depicted in **figure 3.5**:

$$\delta_R = 180^\circ - \delta - 2\varphi_{hkl} \tag{3.5}$$

When the light beams that have been diffracted at the crystal planes $(1\,1\,1)$ and $(2\,2\,0)$ leave the opal again, refraction occurs at the air interface and the light beam is reflected at the final angles δ_{R111} and δ_{R220} respectively. Light diffracted at other crystal planes like $(2\,0\,0)$ is trapped inside the opal because of total reflection at the opal/air interface.[6] Light beams reflected at these planes obviously generate no reflection at all.

3.3.3 UV/vis-spectroscopy in reflection mode

The colourful appearance of opals is mostly attributed to reflection at the $(1\,1\,1)$ planes. Reflections at $(2\,2\,0)$ planes only occur at very acute angles (cf. **figure 3.5**) and the peak of the reflected light is only in the visible region, if very big particles are used. This is due to the small distance a_{220} (**equation 3.2**) between these planes.

Figure 3.6 shows the measuring setup of the reflectance analysis applied during this work. As the $(1\,1\,1)$ planes are aligned parallel to the surface, their reflectivity is measured at or near the glancing angle at $\theta_R = 180 - \theta$.

With this setup it was possible to scan an angle range from 22° to 82° and measure the reflectivity in dependency of the wavelength. Detector and input mirror are movable for adjustment of the angle of incidence. The path length compensator ensures a steady length of the beam's pathway, so that results are comparable.

The reflected wavelength ergo the reflected colour can be described with a combination of **equation 3.3** and **equation 3.4**:

$$\lambda_{111} = 2n\,a_{111}\,sin\delta = 2a_{111}\sqrt{n^2 - cos^2\,\theta} \tag{3.6}$$

---

[6] This effect occurs also at other crystal planes apart from $(2\,0\,0)$.

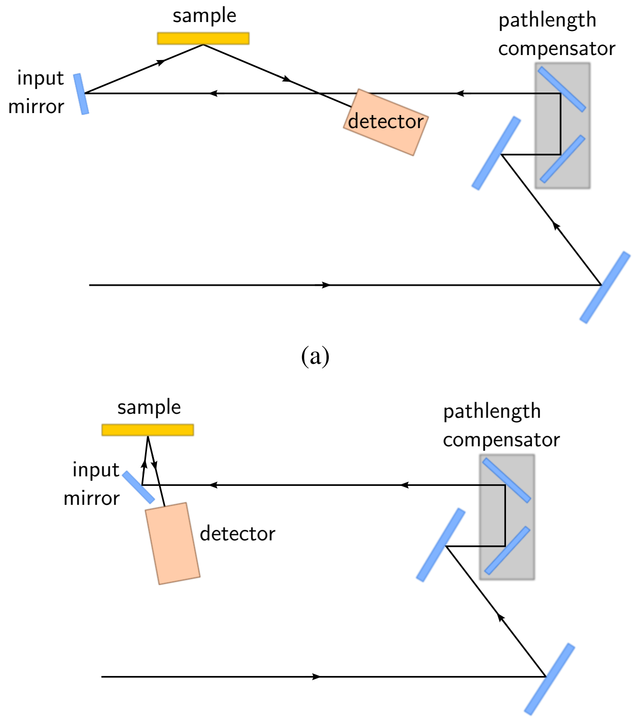

(a)

(b)

Figure 3.6: Measurement setup of the used UV spectrometer in reflection mode (Perkin Elmer Lambda 950 with universal reflectance accessory). Visible are the lower and upper angular extremities, a) 22° and b) 82°.

3.3.4 UV/vis-spectroscopy in transmission mode

The analysis of CCs or IHOs *via* transmission UV/vis-spectroscopy is similar to reflection mode. Only here, UV/vis light is shined through the sample at straight 90°. In this setup, light of a certain wavelength is reflected at the sample's surface and does not travel to the detector behind the sample. The difference in light intensity shined at the sample (I_0) and light intensity, which is collected at the detector (I), is quantified as absorbance (E_λ)

$$E_\lambda = -\log_{10}\frac{I}{I_0} \tag{3.7}$$

Though this is technically similar to absorbance behaviour of dye molecules, the extinction of light in these experiments is solely based on reflection processes at the crystal planes. An exception is the absorption of UV-light of SiO_2 itself, at wavelengths below 400 nm.

3.4 Assembly of SiO_2-based colloidal crystals

As already previously stated, VD was chosen as the method for colloidal crystal assembly due its versatility and relative robustness compared to other methods.

For a successful colloidal crystal assembly, first of all the substrate has to be thoroughly cleaned to remove all impurities on the surface. This was done with the strongly oxidising *piranha acid*, a 1:1 v/v mixture of H_2SO_4 and H_2O_2. This does not only oxidise all impurities, but it also etches the silicates on the glass surface. This induces negative charges, making the glass very hydrophilic and very clean.

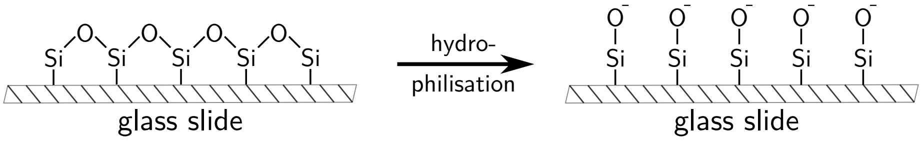

Figure 3.7: Scheme of the hydrophilisation of a glass surface.

The hydrophilicity of the substrate is necessary to ensure a homogeneous spreading of the liquid film on the substrate, when aqueous dispersions are used. Otherwise the surface of the liquid, with it's meniscus touching the substrate, would not evenly cover the substrate and thus a colloidal crystal could not grow in a controlled way.

In **table 3.1**, an overview over some of the deposition experiments performed with 400 nm SiO_2 particles (**SP-3**) is given. All deposition experiments were conducted in a drying oven at ambient pressure to accelerate the evaporation of the solvent. The ventilation of the oven was opened, to ensure an exchange of saturated air to facilitate permanent evaporation of the suspension medium.

The hydrophilised glass substrates were placed vertically in a plastic beaker, which was cleaned with aqueous HF (2 wt.-%) before use in order to remove all silicate impurities, that might interfere in the CC assembly. Subsequently, the particle dispersion was injected through a syringe filter (pore diameter 1 µm) into the flask, where the glass slide was already placed for easier handling.

The composition of the particle dispersion had to be adjusted prior to the deposition

Table 3.1: Overview over selected vertical deposition experiments of SiO_2 particles (**SP-3**) with $d \approx 400\,\text{nm}$. Concentrations were adjusted with absolute ethanol ($w_{EtOH} = 100\,\% - w_{SiO_2} - w_{H_2O}$).

sample	w_{SiO_2} / wt.-%	w_{H_2O} / wt.-%	T / °C	appearance
CC-1	0.1	0	30	thin amorphous layer
CC-2	0.5	0	35	small thin CC[a]
CC-3	2.0	0	35	CC covered by amorphous layer
CC-4	3.0	0	35	thick amorphous layer
CC-5	1.0	20	50	irregular layer
CC-6	1.0	40	50	irregular layer[c]
CC-7	2.0	20	40	iridescent CC[b]
CC-8	2.0	40	40	iridescent CC[b]

[a] Particles sedimented too quickly.
[b] Layers partly iridescent, partly amorphous.
[c] H_2O not evaporated.

experiment. As discussed in **section 3.1.1**, the vertical deposition process is mainly influenced by particle concentration and evaporation velocity of the solvent. The concentration was simply tuned by diluting with suitable solvent.

First, a broad range of particle concentrations in pure absolute EtOH from 0.1 to 3.0 wt.-% were tested (entries **CC-1** to **CC-4** in **table 3.1**) with moderate success. Lower and upper limit of the particle concentration for the successful deposition was found to be between the two extremes. A concentration below 0.5 wt.-% yielded a very thin and amorphous layer of silica, as the concentration of particles was not high enough to keep enough particles at the meniscus, where the deposition takes place (cf. **figure 3.2**).

Particle concentrations over 2.0 wt.-% led to a rather brittle yet also amorphous silica layer, reminiscing of dried white paint (which is also made from suspended particles (here TiO_2)). This is the result of the opposite effect, that was seen before. Here, an oversupply of particles was deposited too fast and in a too large amount to yield regularly oriented particle arrays.

At an intermediate particle concentration of 0.5 wt.-% the successful crystal assembly could be observed by the emergence of brilliantly iridescent blue-greenish colours, although the layer appeared to very thin, as the concentration was still rather low. Also, only CC with limited vertical spread were formed under these conditions.

It turned out, that the particles with an average diameter of 400 nm settled too fast in pure ethanol for the deposition of larger area colloidal crystals (more than 0.5 cm in vertical dimensions), as the surface of the dispersion depleted from particles and therefore the colloidal crystal could not be deposited any more.

Therefore, (ultra-pure) water was added to the suspension. This influences the deposition in several ways. First of all, water is denser than ethanol ($1.0\,\mathrm{g\,mol^{-1}}$ compared to $0.789\,\mathrm{g\,mol^{-1}}$), which lowers the sedimentation velocity (v_p) of the silica particles. This can be understood by considering the Stokes' law, which describes the sedimentation of spherical solids in a liquid

$$v_p = \frac{2r^2 g(\rho_p - \rho_f)}{9\eta} \tag{3.8}$$

with ρ_p and ρ_f the density of the particle and fluid respectively, g the standard gravity, r the radius of the particle and η the dynamic viscosity of the liquid medium. By adding water to the mixture, ρ_f as well as η are increased and therefore the overall sedimentation velocity is lowered.

While the increase in density might be straightforward, this is not the case for the increase in viscosity. Neat water possesses a lower viscosity (0.89 mPa s) compared to neat ethanol (1.074 mPa s) at standard conditions. But as there are molecular interactions between water and the hydroxyl groups of ethanol, which also result in a decrease in volume when mixed, the viscosity of a water-ethanol-mixture increases until a maximum at 0.6 share of water is reached.[105] For example, at 20 °C the viscosity increases from 1.2 to 2.0 mPa s when 20 wt.-% of water is added.

In total, adding 20 wt.-% of water to the ethanolic particle suspension halves v_p and therefore leads to a much more stable dispersion, from which it is possible to deposit larger colloidal crystals.

After the introduction of water to the liquid phase, the system was more robust towards sedimentation, though still other factors influenced the particle assembly negatively. Entry **CC-5** and **CC-6** of **table 3.1** show water-stabilised dispersions with intermediate particle concentrations of 1.0 wt.-%. Assembly was performed at an elevated temperature of 50 °C for fast deposition to overcompensate particle sedimentation.

As previously shown, higher temperatures lead to faster evaporation of the liquid and therefore quicker particle deposition. Here, the delicateness of the VD experiments can be nicely seen. Though particle sedimentation was suppressed by quicker particle deposition, the deposition velocity was too fast in the end. The oversupply of particles, that was previously explained for entry **CC-4** with a high colloid concentration, was also present when working at elevated temperatures, and resulted in a similarly bulky amorphous silicate layer.

So with lower temperatures of 40 °C, though higher particle concentrations of 2.0 wt.-% were used, nicely iridescent CCs could be deposited from 400 nm SiO_2 dispersions. Photographs of **CC-7** are shown in **figure 3.8**.

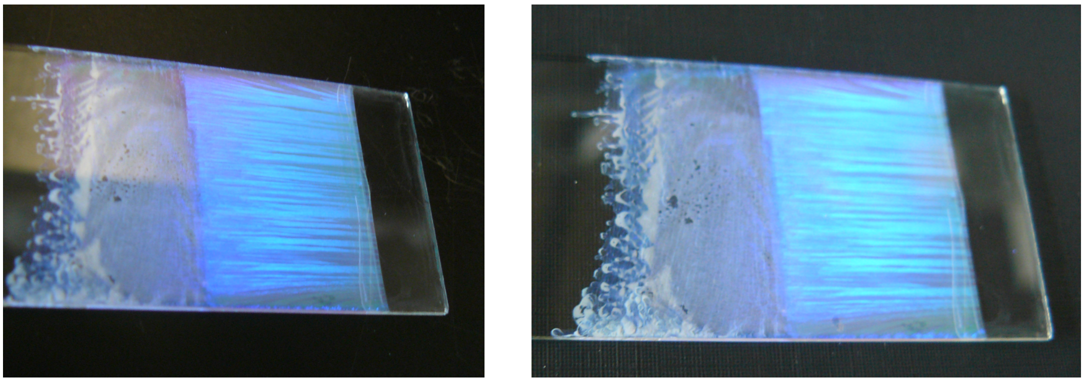

Figure 3.8: Photographs of a colloidal crystal **CC-7** deposited from 400 nm SiO_2 particles observed under different arbitrary angles.

According to Bragg's law (**equation 3.4**), the wavelength which is reflected by the CC is depending on the angle of incidence. This correlation is responsible for the different colours, which can be seen in **figure 3.8**. The glass slide onto which the CC was deposited, was tilted and therefore different colours were observed for the same material, in this case blue and turquoise.

The upper part of the deposited material appears rather amorphous without a noticeable reflection pattern. This seems to be due to the experimental setup. This part of the deposit was closest to the surface of the particle dispersion in the beginning. As mentioned earlier, for better handling the glass slide was set first in the plastic beaker and the suspension was injected afterwards. So particles might still have been moving much faster than in equilibrium state, due to the force applied when the dispersion was injected with a syringe to the beaker. But since deposition already started due to evaporation of EtOH in the oven, the first part of the deposit is of random amorphous nature. Nevertheless, after equilibration of the dispersion, the major part of substrate was covered with a regular colloidal crystal array.

3.5 Structural elucidation

The colourful reflections of the assembled SiO_2 particles were only a first hint, that a regularly ordered material was deposited. And since it is known, that SiO_2 particles assemble into fcc lattices,[59] some information about the spatial arrangement of the particles in the CC was already known.

3.5.1 Scanning electron microscopy of colloidal crystals

Nevertheless, parameters like total layer thickness cannot be guessed or assumed, so scanning electron microscopy (SEM) micrographs were recorded.

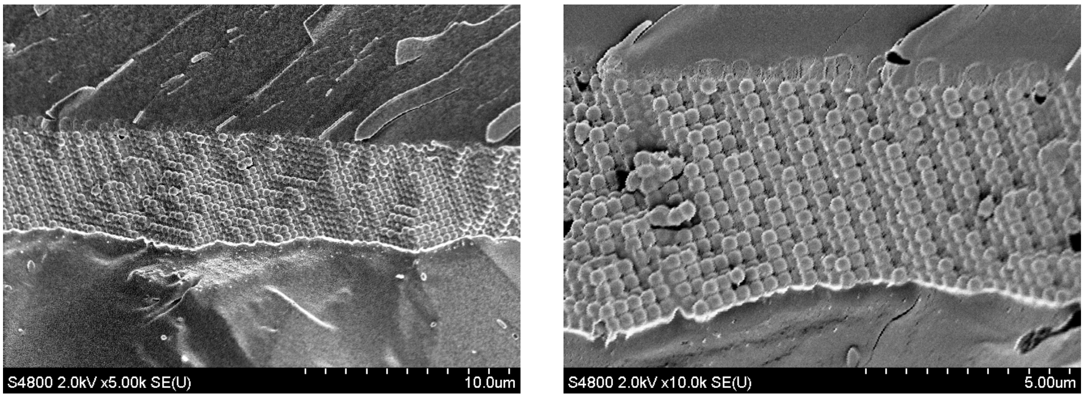

(a) (b)

Figure 3.9: SEM micrographs of SiO_2 CCs (with hydrogel matrix) after platinum sputtering. Scale bar is given below the micrographs.

In **figure 3.9**, SEM micrographs of sample **CC-7** are presented. The samples already included hydrogel matrix, which can be seen as "corona" around the particles. For better contrast, samples were sputtered with platinum, freeze dried and fractured prior to the measurements (mainly due to the hydrogel matrix). The first information, which can be derived from the micrographs, are the size of individual particles and the total thickness of the CC.

The diameter of an individual particle is 390 nm determined by SEM. This is in very good agreement with the particle size determined by DLS measurements. With a total number of 14 SiO_2 particle layers, the thickness of the CC adds up to approx. 4.8 µm. Also, it is nicely visible that the particles are regularly aligned, in a closely-packed order. From this angle, it was not possible to determine, whether the particles were packed in a face-centred cubic (fcc) or hexagonal close-packing (hcp). But as mentioned earlier, fcc packing is expected for vertically deposited CCs.[59]

3.5.2 Atomic force microscopy of colloidal crystals

In addition to SEM, the structure of assembled CCs was additionally investigated with atomic force microscopy (AFM). Here, in contrast to SEM, the sample was imaged from the top, visualising the position of the colloids relative to each other.

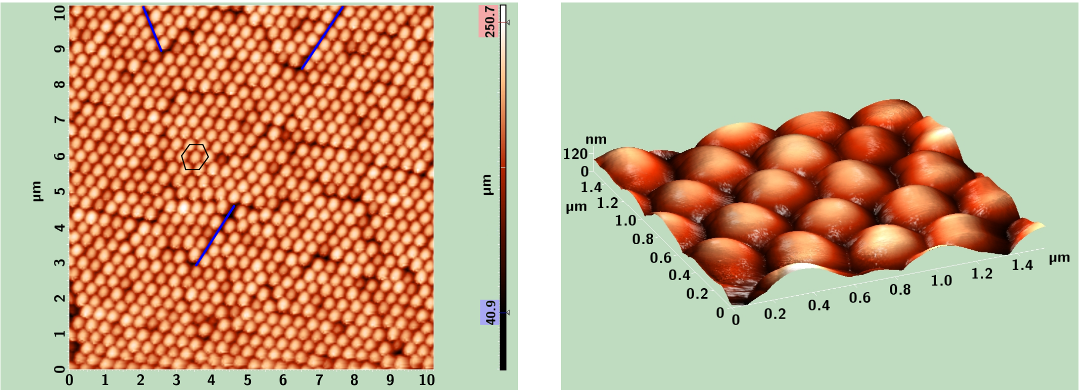

(a)

(b)

Figure 3.10: Atomic force micrographs of a CC. a) image from top, defects marked in blue, hexagonal unit in black; b) 3D representation. Scales are depicted in the micrographs.

A micrograph of a randomly chosen section of a CC is presented in **figure 3.10(a)**. First of all, the regular order of the particles, which was already determined in the

SEM micrographs, is also visible here. Every particle is surrounded by six other colloids, which is typical for close-cubic packing (marked with a black hexagon in **figure 3.10(a)**).

However, also some defects in the colloidal crystal structure are present (blue lines in **figure 3.10(a)**). These defects are the result of either a) deviation in particle diameter of the used colloids or b) irregularities during the assembly process (cf. **section 3.1.1**). In the micrographs, defects of varying severity are visible. For the defects marked in blue, the hexagonal particle array is not given any more. While for other defects, this order is often still maintained, though a narrow gap between the particles is visible. The more defects are present in the assembly, the worse the regular array, and therefore, also quality of Bragg diffraction suffers. Nevertheless, a certain number of defects often cannot be prevented, in particular in the case of the applied large, fast sedimenting silica particles, where deposition has to be done at a higher rate.

A strong deviation in particle diameters is not visible, though also small deviations can already lead to minor defects. Comparing individual particle diameters with those determined by the other methods, average sizes of 385 nm determined by AFM are again in good agreement with those determined by other methods. A possible explanation for the minor deviation of the particle size obtained from DLS measurements is the presence of the electric double layer around the silica particles (cf. **chapter 2**). Since this double layer is affecting the diffusion velocity, which is detected in DLS, the particles may appear larger in DLS than they actually are. Comparing the diameters determined with the different methods, the size of the electrical double layer is estimated to be 20 nm or approx. 5 % of the total particle size.

Table 3.2: Overview over average silica particle (**SP-3**) diameters determined *via* various methods.

DLS[a]	SEM[b]	AFM[b]
410 nm	390 nm	385 nm

[a] peak average
[b] measured average from micrographs

In summary, short- and long-range order in the assembled silica colloid crystals are of satisfactory quality. Closely-packed arrays with minor amount of defects and total thickness of 14 layers account for pronounced interference with incident light (i.e. Bragg diffraction). More details about light interference will be given in the following section.

3.6 Interference with Light

The regular particle orientation in sample **CC-7** was successfully evaluated using SEM and AFM. For the application as colloidal crystals, optical properties are an important parameter. An indication for pronounced Bragg diffraction is the colourful iridescence, which can be seen by bare eye when light is shined onto the CC. To quantify the Bragg diffraction and to study the angular dependence of the reflection, both UV/Vis transmission and reflection measurements were performed.

3.6.1 Transmission UV/Vis spectroscopy of colloid crystals

The transmission spectra of the various CCs prepared all look very similar. Unsurprisingly, the position of the band gap is around 800 nm for all samples. The deposition parameters do not seem to affect the interparticle distance significantly, which defines for the position of the Bragg peak. However, the intensity and width of the different Bragg peaks differ notably between the samples.

While the transmission UV/Vis spectrum of **CC-7** in **figure 3.11** is characterised by a rather narrow intense peak, the other samples show broad and fairly weak signals. The difference can be attributed to different total layer thickness of the CCs. It was shown by Hiltner and Krieger, that band gaps tend to broaden, when thin CCs are examined.[91, 102] Thin CCs also result in peaks with low intensity, because not all light is reflected by the colloidal crystal lattice, but a substantial part travels right through the material without any diffraction.[106] This suggests, that among all tested CC samples, **CC-7** with the most intense peak is the thickest regular particle assembly, which was achieved in this work.

When comparing the recipes from **table 3.1** with the respective spectra of the resulting CC samples in **figure 3.11**, a statement on the limitations of the VD process with the synthesised silica particles (**SP-3**) can be made. The limit in thickness of

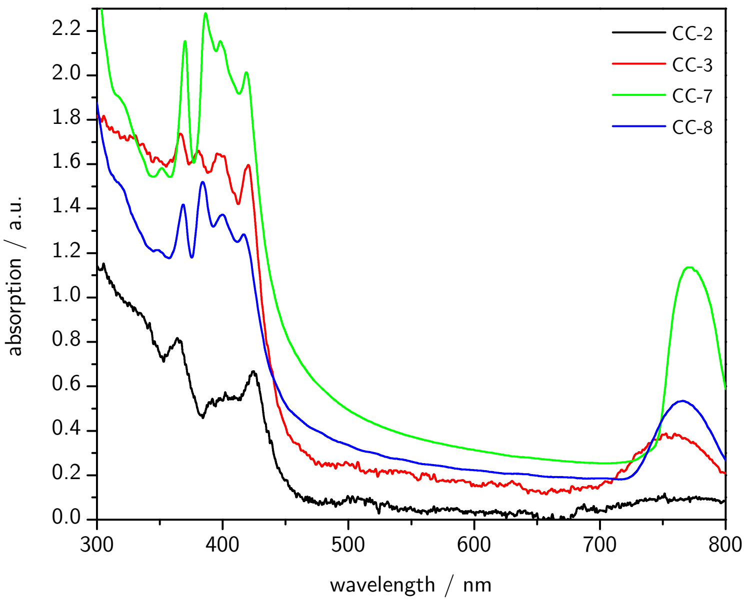

Figure 3.11: Plots of UV/Vis transmission measurements of various colloidal crystals deposited on glass slides.

the CC assembly seems to be reached with **CC-7**. Increasing particle concentration as well as decreasing deposition velocity, which would normally increase the layer thickness, either lead to an amorphous material (**CC-4**) or a reduction in layer thickness (**CC-8**).

When parameters are precisely determined and followed, the deposition of the CCs is reproducible and results in very similar optical properties, like peak width, intensity and wavelength. From the various parameters, the deposition environment is the most difficult to reproduce. Ovens with a different volume or ventilation system possibly result in a different evaporation velocity, which will also affect the particle assembly. Hence, all CC depositions in this work were performed in the same oven (see **chapter 7** for more details).

3.6.2 Reflection UV/Vis spectroscopy of colloid crystals

The theory of Bragg diffraction describes an angular dependence for the wavelength of light, which is reflected from a crystalline ordered material (cf. **section 3.3**). For evaluation of the angular behaviour of the deposited CCs, UV/Vis measurements in reflection mode were performed (for details on the measurement setup, see **section**

3.3.3). Reflections were scanned from 82 to 22°, relative to the perpendicular. These angles were the limits for the used equipment.

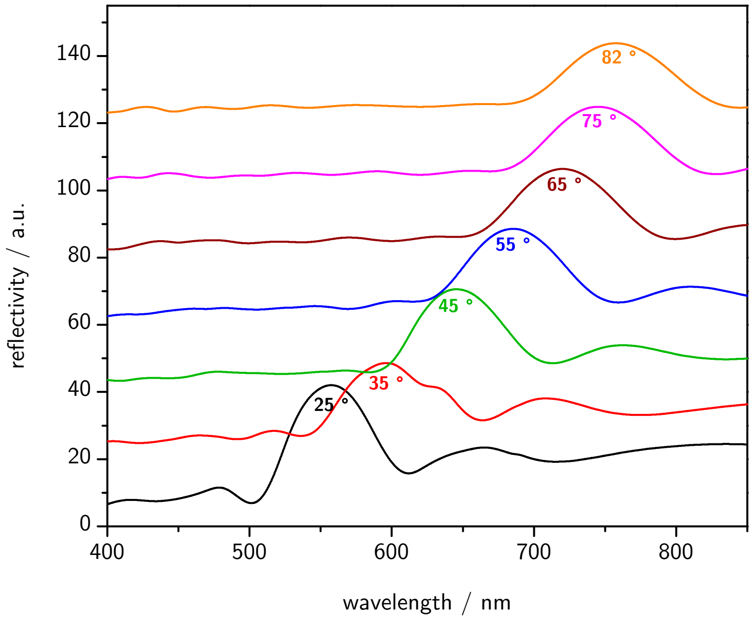

Figure 3.12: Angular dependent UV/Vis reflection spectra of **CC-8**. Spectra are staggered for better viewing.

As expected, reflection UV/Vis spectra show a linear angular dependence (cf. Bragg's law, **equation 3.4**), depicted in **figure 3.12**. Here, the reflection spectra of **CC-8** are depicted exemplary for all colloidal crystals, the spectra of the other CCs only differ in intensity (cf. **figure 3.11**). The band gap from transmission experiment presented earlier, which resembles an angle of 90°, is in good agreement with the reflection measurement. The reflections at 82 and 75° lie clearly out of the visible range for the human eye, i.e. in the infrared region. Beginning from 65°, reflections at smaller angles shift from red (65°) to green (25°). The blue colour, shown in **figure 3.8** occurs at even lower angles. For thermo-responsive sensors that shrink at elevated temperature, the band gaps will be eventually blue-shifted, because interparticle distance is reduced. This will be presented more detailed later, in the IHO section.

4 Thermoresponsive polymers and hydrogels

The colloid crystals, which were described in **chapter 3**, do not posses any responsive properties. Meaning, apart from their ability to interact with light to yield colourful interferences, there is no possibility to manipulate their colour in any other way, after the material was deposited. Thinking about the idea of detecting temperature shifts or presence of (bio)molecules, there is the necessity to embed the colloidal crystal into a matrix, which would make it possible to identify analyte molecules and respond to a binding event by distortion of the colloid crystal.

To fulfil the demands stated above, thermoresponsive polymers were selected as a suitable material. For mechanical and solvent resistance, cross-links between the polymer chains need to be established. Because of the delicate hydrophilic/hydrophobic balance of thermoresponsive polymers, it is possible to induce a shrinking or swelling of the material. This effect can be either induced by a change of ambient temperature, or by binding of an analyte molecule to a suitable targeting unit, which was coupled to the polymer chain. A contraction or expansion of the polymer affects the plane distance of the inverse opal and therefore the colour feedback (see chapter 5 for more details).

As a starting point, thermoresponsive linear copolymers were synthesised and their cloud points analysed. Pretests with linear copolymers were considered necessary, as cloud point determination in cross-linked polymer networks is more difficult. With the experiences from these pretests, cross-linked hydrogels were produced and their swelling analysed.

4.1 Theoretical view on thermoresponsive polymers

Thermoresponsive polymers are a class of polymers, which is defined by their special behaviour in (aqueous) solution. Solutions of these polymers react to a change in temperature, by a discontinuous change of their solubility. This polymer class is divided in two sub-groups, exhibiting either an upper critical solution temperature (UCST) or lower critical solution temperature (LCST). Polymers belonging to the former group are characterised by insolubility below a certain temperature (the UCST), while the others are only soluble up to a certain temperature, the LCST.

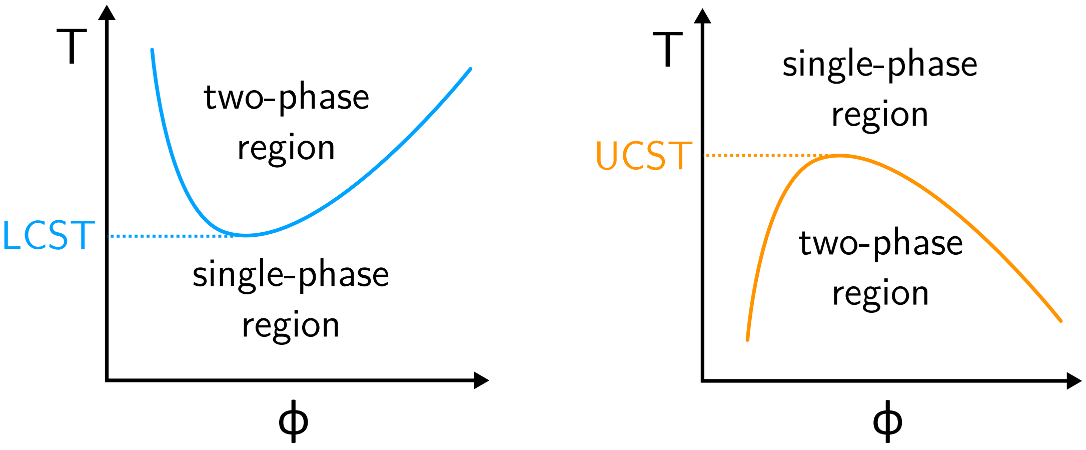

(a) lower critical solution temperature (LCST)

(b) upper critical solution temperature (UCST)

Figure 4.1: Schematic illustration of phase diagrams for polymer solution behaviour (temperature (T) v. polymer volume fraction (ϕ)).

A schematic representation of the phase diagrams for LCST and UCST polymers is given in **figure 4.1**. It is visualised, that by increasing the temperature at a certain molar fraction ϕ of a polymer in a solvent (here water), the border between a one and two phase system is crossed. This results in either a precipitation, in case of an LCST-polymer or a dissolution, when dealing with a UCST-polymer. The actual LCST or UCST are marked in the diagram. The LCST is the point in the phase diagram, which is the lowest temperature at a certain molar fraction of polymer, where the discontinuous change in solubility takes place (for UCST it is the highest temperature). All other points on the parabolic phase boundary are called phase transition temperature. In practice, these phase transition temperatures are not always identical with the cloud point, which is the temperature at which polymer agglomerates are detectable (cf. **section 4.1.1**). Thus, cloud points are the characteristic value, which is used in this work.

The solution properties of the thermoresponsive polymers can be explained regarding their structure. The structural formulae of several oligo(ethylene glycol)-methacrylate (OEGMA)-based monomers are depicted in **figure 4.2**. Most of the thermoresponsive monomers are consisting of a hydrophilic and a hydrophobic part. In **figure 4.2**, the hydrophobic part of the monomers, which is later transformed to the polymer backbone, is marked in red. The hydrophilic side chains are depicted in blue.

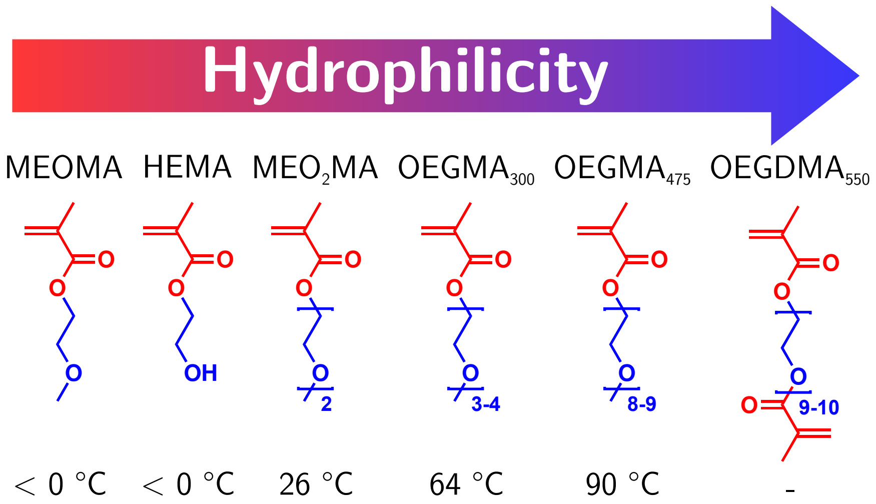

Figure 4.2: Overview over a selection of oligo(ethylene glycol) methacrylates, sorted by hydrophilicity of the corresponding homopolymers (CPs from literature[107–113] denoted below).

The balance between hydrophilic and hydrophobic groups determines the solubility behaviour of the polymers. If a polymer only consists of hydrophilic units (e.g. poly(phosphates)), then it is always soluble in water, regardless of the temperature. The opposite is true for polymers synthesised from only hydrophobic monomers (e.g. poly(styrene)). Poly(styrene) is insoluble in water at any temperature.

Nevertheless, hydrophilic side groups on a hydrophobic backbone do not necessarily provide thermoresponsive properties. If the influence of one of the groups is much stronger than the other, either a soluble or insoluble polymer is obtained. This special behaviour can be observed e.g. for ionic polymers like poly(acrylic acid) or poly(styrene sulphonate). The ionic side groups of these two polymer are so hydrophilic, that they are always soluble in water, regardless of temperature.

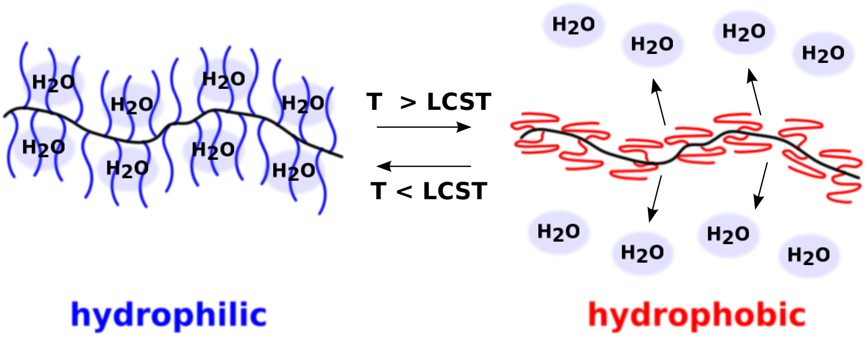

Figure 4.3: Schematic representation of a polymer chain below and over the LCST.

For the explanations of the LCST phenomenon, a thermodynamic consideration is one of the possibilities.[114] At T $<$ LCST, the hydrophobic side chains of the polymer are surrounded by water molecules, while the hydrophilic moieties of the polymers are linked over hydrogen bridges. Both contributions provide for the solvation of the polymer in water. This implies, that ΔS_{mix} becomes negative in this process, because of the arrangement of the water molecules around the hydrophobic moieties. In total, the contribution to the Gibbs free energy of mixing ΔG_{mix} is positive (cf. **equation 4.1**. The enthalpy of mixing ΔH_{mix} is also negative and therefore contributes to $\Delta G_{mix} < 0$ at all temperatures:

$$\Delta G_{mix} = \Delta H_{mix} - T\Delta S_{mix} \tag{4.1}$$

When elevating the temperature, the entropic term prevails after reaching the critical temperature. ΔG_{mix} becomes positive, polymer and water demix. Additional to this purely entropic based explanation, the temperature dependence of ΔH_{mix} is also considered. Depending on the polymer system, the phase transition is not necessarily only entropy driven.[115]

This is valid as long as $\Delta G = \Delta H - T\Delta S$ is zero (with ΔG the free energy of dissolution, ΔH the enthalpic contribution and ΔS the entropic input).

At low temperatures, the dissolution of the polymer is driven by a strong negative enthalpic component ΔH, originating from the hydrogen bonding between water and the corresponding polar moieties of the polymer. However, the entropic ΔS term is unfavoured for dissolution, as hydrogen bonding between the polymer's hydrophilic moieties and water, as well as the hydrophobic moieties of the polymer, require an organization of water molecules.

At higher temperatures, water molecules are becoming more mobile, which weakens the hydrogen bonds of water to the polymer. Following, water is expelled from the system because polymer-polymer interactions are favoured over polymer-water interactions. Hence, the polymer collapses and precipitates from solution, which is observable with the bare eye. For better understanding, this process is briefly illustrated in **figure 4.3**. The precipitation of the polymer from solution at the CP is also exploited in some of the analytic tools, which are described later in **section 4.1.1**.

A non-exhaustive list of LCST-polymers contains poly(*N,N*-diethylacrylamide), poly(*N*-vinyl caprolactam), poly(2-(dimethylamino)ethyl methacrylate), poly(ethylene glycol) and poly(*N*-isopropylacrylamide).[114]

Most studies in literature deal with poly(*N*-isopropylacrylamide) (PNiPAam), since its discovery by Heskins and Guillet in 1968.[116] Poly(NiPAam) displays a CP around 32 °C while showing a very sharp transition between dissolved and non-dissolved phase.[117] Since PNiPAam belongs to the group of acrylamides, it is also possible to (co)polymerise PNiPAam with a range of different techniques and a large number of other (meth)acrylates or -amides.[118]

Nevertheless, working with PNiPAam also entails disadvantages. First of all, due to its chemical nature, PNiPAam shows a distinct hysteresis in its cooling cycle, which is affected by the heating/cooling cycle.[119–121] Also, PNiPAam's transition temperature is dependent on molecular weight and type of end-groups of the polymer.[122, 123]

With the synthetical work of Han *et al.*[109], Ali *et al.*[124] and Kitano *et al.*[125], a new group of thermoresponsive (co)polymers based on oligo(ethylene glycol) methacrylates was established. These (co)polymers did not show any hysteresis while cooling and additionally, their cloud point could be tuned by varying the copolymer composition, as comonomers of different hydrophilicity were incorporated in the polymer. The longer the oligo(ethylene glycol) side chains of the methacrylate units are, the higher will be the corresponding CP. This can be accounted to the increasing hydrophilicity with more of the ethylene glycol units in the side chain.

Lutz *et al.* performed additional studies, with controlled radical copolymerisation of poly(MEO_2MA-stat-$OEGMA_{475}$) copolymers.[108, 126] With increasing share of oligo(ethylene glycol) methylether methacrylate M_n = 475 g mol^{-1} ($OEGMA_{475}$) in the copolymer, the CP is increasing linearly, making it comfortable to tune the cloud point in a wide range (cf. **figure 4.4**). If e.g. a CP around body temperature (37 °C) is desired, a monomer composition of 8 mol-% $OEGMA_{475}$ and 92 mol-% di(ethylene glycol)methylether methacrylate (MEO_2MA) is the right choice.

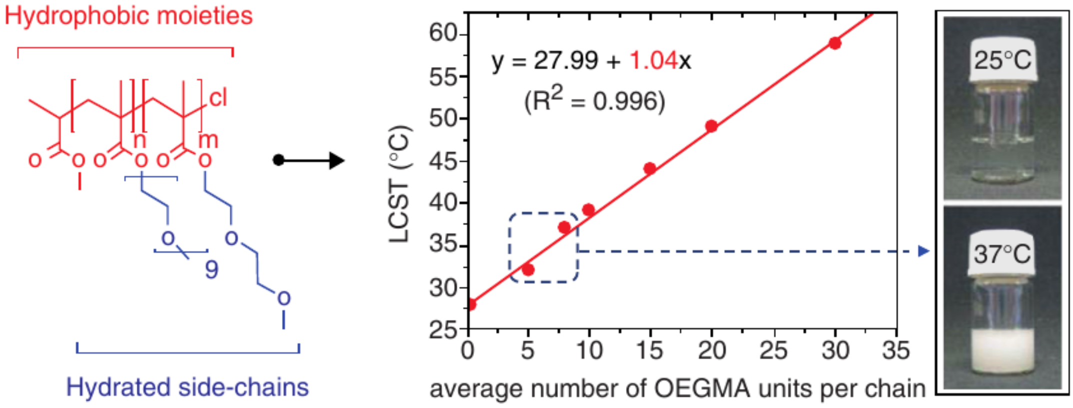

Figure 4.4: Plots of measured CPs as a function of average amount of incorporated $OEGMA_{475}$ units per chain of poly(MEO_2MA-stat-$OEGMA_{475}$) copolymers with varying composition. (From [127] used with permission.)

This combination of comonomers also works with the other representatives of the OEGMA family (cf. **figure 4.2**), since they are all methacrylic monomers and therefore copolymerise in a nearly random fashion, because their reactivity is not influenced by the length of the OEGMA side chains very much.[108, 127]

In **figure 4.2**, different ethylene glycol based methacrylates and there respective CPs as homopolymers are depicted. Starting from the left, the shortest representative p(MEOMA) is considered to be hydrophobic and is not soluble in water under standard conditions. When the methyl ether endgroup is substituted by a hydroxyl group, the obtained polymer is more hydrophilic but still not soluble in water Nevertheless, p(HEMA) is able to swell and take up a considerable amount of water, making it very interesting as a material for soft contact lenses.[128–131] In this work, hydroxyethyl methacrylate (HEMA) was incorporated into the copolymers because of the functional hydroxyl group, at which polymer-analogous reaction can be performed.

Beginning from homopolymers of di(ethylene glycol)methylether methacrylate (MEO_2MA), the rest of the series are water-soluble at room temperature, though displaying LCSTs at some point. When at least two monomers of the OEGMA series are combined in one copolymer, the CP is adjustable from below room temperature to nearly boiling point.

Comparing the CPs of OEGMA-type homopolymers in **figure 4.2**, an increase of nearly 40 °C in CP temperature from MEO_2MA to oligo(ethylene glycol) methylether methacrylate $M_n = 300\,\mathrm{g\,mol^{-1}}$ ($OEGMA_{300}$) is the most pronounced in this selection. Adding only one to two ethylene glycol side chain units accounts for this massive increase in hydrophilicity and therefore also in the resulting CP of the polymer. When advancing to $OEGMA_{475}$, with an average increase of five ethylene glycol side chain units, an increase of the CP of "only" 25 °C is obtained. Due to design of the synthesis, the side-chains of the $OEGMA_{300}$ and $OEGMA_{475}$ are not precisely defined in length but a mixture of several oligomers is present, with the displayed numbers being the average. This leads to a thermal transition of shorter oligomers at temperatures which are lower than expected for the average number of e.g. eight EO side-chains.

In summary, oligo(ethylene glycol)-based monomers were considered to be well suited to fulfil the desired task as a responsive matrix material for inverse hydrogel opals. OEGMAs are hydrophilic, biocompatible, their LCST is adjustable, they are commercially available as mono- an bi-functional methacrylates and therefore OEGMAs are easily polymerisible and cross-linkable by various radical polymerisation techniques.

4.1.1 Cloud point determination

There are several methods to characterise the thermoresponsive properties of (co)-polymers. For polymers in solution, light scattering techniques like turbidimetry[132] or DLS[133] are the most frequently applied approaches.

For cross-linked hydrogels, determination of mass or volume swelling is most common. Alternatively, differential scanning calorimetry (DSC) can be applied to measure the enthalpic fluctuation around the CP.[134–137] Applying DSC for cloud point determination of cross-linked OEGMA polymers is difficult, since only very weak heat fluxes are obtained. Both DSC and DLS were not applied for CP determination in this work, so these methods are not explained in detail here (DLS was already introduced in **section 2.3.3.2**).

4.1.1.1 Turbidimetry

The determination of cloud points *via* turbidity measurements is relatively simple. In a temperable cell, (laser) light is passed through a solution of the (co)polymer onto a light detector. Below the CP, (nearly) 100 % of the light is transmitted, as virtually no scattering by the solution occurs. When the temperature is elevated and finally the CP is reached, the polymer coils collapse, agglomerate and thus generally form mesoglobules or precipitate from solution. The polymer aggregates scatter incoming light and the transmission drops to nearly zero.

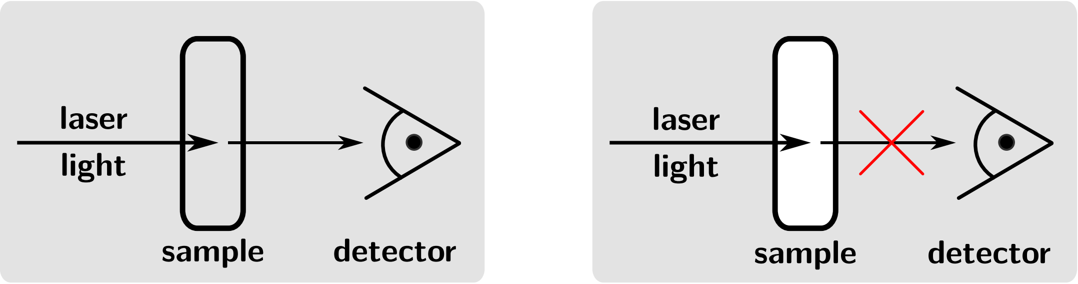

(a) (b)

Figure 4.5: Schematic representation of a turbidity measurement of a (co)polymer a) below and b) above the LCST.

The CP is normally determined as the onset of the turbidity curve, as this is the point, where the first visible agglomeration occurs. When working with polymers, which are characterised by a broader transition region from 100 % to 0 % transmittance, which is often the case for oligo(ethylene glycol)s, it is more usefull to use the inflection point of the curve at 50 % transmission. This allows to compare polymers with a sharp transition point with those having a broad transition. In this work, all cloud points were determined at the inflection point, which are denoted as CP_{50} to avoid any confusion.

4.1.1.2 Swelling ratio

For cross-linked hydrogels, the CP often cannot be determined by turbidity measurements, because not all hydrogels become turbid when collapsed. For this reason, the swelling ratio is determined as a function of temperature alternatively. For cross-linked thermoresponsive polymers (hydrogels), the hydrophilic/hydrophobic balance is the same as for their linear counterparts. As previously described, water is kept in the polymer system below the CP. When temperature is elevated and the phase boundary is crossed, water is expelled from the hydrogel and the hydrogel shrinks. The opposite is observed, when temperature is lowered below the CP. This gain or loss of water in the system can be quantified *via* the swelling ratio.

The swelling raio (SR) of a cross-linked hydrogel can be either determined by weight or by volume. For both approaches, first the hydrogel is equilibrated in water at the temperature, that is to be examined. For weight determination, the hydrogel is taken out of water, excess liquid is removed and the sample is weighed at a regular fine balance. To determine the swelling ratio, also the dry weight has to be known. Then, the swelling raio (SR) at a certain temperature can be calculated with the following simple expression:

$$SR = \frac{m_{swollen}}{m_{dry}} \tag{4.2}$$

So basically, the swelling ratio expresses the amount of water, which the hydrogel is able to retain at a certain temperature. For example, a value of $SR = 2$ implies, that the corresponding hydrogel is able to take as much water as its own dry weight. In principle, when a temperature near the CP is reached, the SR is expected to drop significantly, as water is expelled from the system when it switches to its hydrophobic state. However, recent findings indicate, that p(OEGMA) networks in principle show broader transitions than their respective linear counterparts.[138]

The determination of swelling ratios by volume works after the same principle. However, the hydrogel is not weighed, but the dimensions of the film are measured and the shrinkage or swelling in volume is evaluated. Since it can be difficult to measure small dimensional changes, weighing the sample is the more straightforward method.

4.2 Linear HEMA/OEGMA copolymers

During this work, linear copolymers consisting of HEMA, OEGMA and MEO_2MA were synthesised *via* free radical polymerisation. The idea behind this combination of thermosensitive comonomers was to be able to create a copolymer with a pronounced number of reactive groups (hydroxyl groups from HEMA), which is still able to undergo a phase transition in a suitable temperature range.

All of the linear copolymers were used to estimate the CPs of the various compositions. Suitable formulations were later used for the synthesis of cross-linked hydrogels, which were intended to be used as a matrix material for inverse hydrogel opals (IHOs). After polymerisation, functionalisation of the hydroxyl groups with targeting groups for biomolecule recognition should be possible.

Additionally to their thermoresponsive nature, OEGMA polymers are predestined for the use in biomolecular applications, because they posses excellent bio-compatibility. [108, 126, 127] Biomolecules, e.g. even human or mammalian cells, survive when they are subjected to an OEGMA surface. Moreover, there are no unspecific interactions between OEGMA polymers and biomolecules, which is also known for poly(ethylene glycol) (PEG) for quite some time. Especially the last fact makes OEGMA polymers suitable for biomolecular sensing applications. If a specific analyte molecule is to be bound with a targeting unit, then unspecific interactions with other biomolecules have to be avoided.

4.2.1 Synthesis and cloud point determination of linear HEMA/OEGMA copolymers

All linear copolymers were synthesised *via* free-radical polymerisation in ethanol with an azo-based initiator. Two series of copolymers with varying composition, for the estimation of CPs, were prepared. The first series comprised of poly(HEMA-stat-$OEGMA_{300}$), while the second was made of poly(HEMA-stat-$OEGMA_{475}$-stat-MEO_2MA). With the first series it was possible to incorporate a high number of functional hydroxyl groups in the copolymer ($\geq$ 65 mol-%), while for the second series a lower amount of HEMA ($\approx$ 10 mol-%) was used. An overview over the composition of these linear copolymers is given in **table 4.1**. The molar fraction χ of the monomers was calculated from the feed.

Table 4.1: Composition and CP_{50} of various synthesised linear copolymers.[a]

	χ_{HEMA}[b]	$\chi_{\text{OEGMA}_{300}}$[b]	$\chi_{\text{OEGMA}_{475}}$[b]	$\chi_{\text{MEO}_2\text{MA}}$[b]	$\overline{N}_{EG}$[c]	CP_{50}[d] / °C
LCP-1	80	20	-	-	1.7	26
LCP-2	75	25	-	-	1.9	31
LCP-3	70	30	-	-	2.1	42
LCP-4	65	35	-	-	2.2	45
LCP-5	10	-	10	80	2.6	34
LCP-6	10	-	20	70	3.2	45
LCP-7	7	-	34	59	4.1	67

[a] Conditions: Initiator V-501, [I]/[M] 1:100 in EtOH at 60 °C. Solvent/monomers 4:1 v/v. Purification: precipitation in Et_2O.

[b] Molar fraction in monomer feed.

[c] Calculated mean number of EG side chain units per monomer unit. See experimental part for details.

[d] $2.0\,\text{g}\,\text{L}^{-1}$ in ultra-pure water; heating rate $1.0\,°\text{C}\,\text{min}^{-1}$.

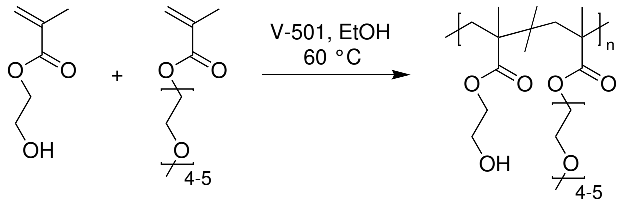

Figure 4.6: Scheme of the radical copolymerisation of binary copolymers **LCP-1** to **LCP-4**.

The first series of copolymers, **LCP-1** to **LCP-4**, was designed to carry a vast number of hydroxyl moieties, while OEGMA_{300} was used to counter-balance the relatively low hydrophilicity of HEMA. The aim was to obtain a CP in the region of body temperature.

The second series, **LCP-5** to **LCP-7**, consisted of much less HEMA than the first series. For functionalisation experiments, this series represented a copolymer with a low content of functional groups. It was to explore, whether a copolymer with such a low biotin content is still able to bind enough avidin to manipulate the LCST of the polymer. The comonomer pair of MEO_2MA and OEGMA_{475} was applied in the second series to adjust the cloud point of the respective copolymers.

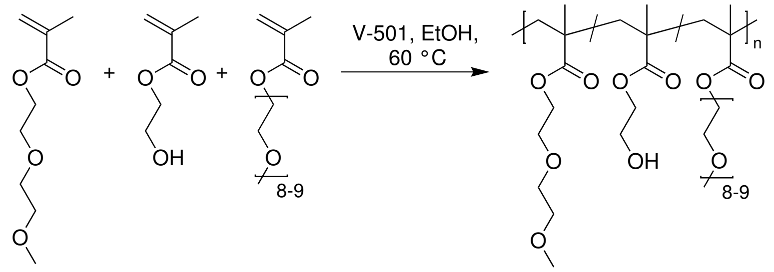

Figure 4.7: Scheme of the radical copolymerisation of ternary copolymers **LCP-5** to **LCP-7**.

From $\overline{N}_{EG}$ in **table 4.1** it is evident, that the cloud points of the polymers of the second series are designed to be quite higher than those of the first series. As previously described, cloud points of OEGMA copolymers are mainly determined by the number of ethylene glycol (EG) units in the side chain.[108]

Cloud points of all copolymers were determined using turbidimetry. The obtained CPs of the linear copolymers were used for estimating the thermal transition properties of the cross-linked hydrogels, which cannot be analysed with this simple analytical method due to their insolubility.

Plots of transmittance versus temperature for copolymers **LCP-1** to **LCP-7** with increasing number of $\overline{N}_{EG}$ in the copolymers are shown in **figure 4.8**. All selected samples displayed sharp transitions with or without minimal hysteresis.

When increasing the ratio of OEGMA$_{300}$ from 20 to 35 % (**LCP-1** to **LCP-4**), CP_{50} was shifted from 26 to 45 °C, as expected. Considering the second series in itself, transition temperatures from **LCP-5** to **LCP-7** also increased with increasing $\overline{N}_{EG}$ content.

Nevertheless, $\overline{N}_{EG}$ is not the only parameter determining the CP (cf. **section 4.1**). When comparing both series with each other, **LCP-5** with a higher $\overline{N}_{EG}$ than **LCP-3** and **LCP-4** still showed a lower CP. Other characteristics, such as end-groups of the EG side-chains can also influence the thermoresponsive behaviour. Such effects have already been discussed in literature.[107] The influence of end-groups of the side-chains is most pronounced when including a high amount of HEMA in the copolymer, as the hydroxyl end-group enhance the hydrophilicity compared to the methoxy end-group of MEO$_2$MA and OEGMA.

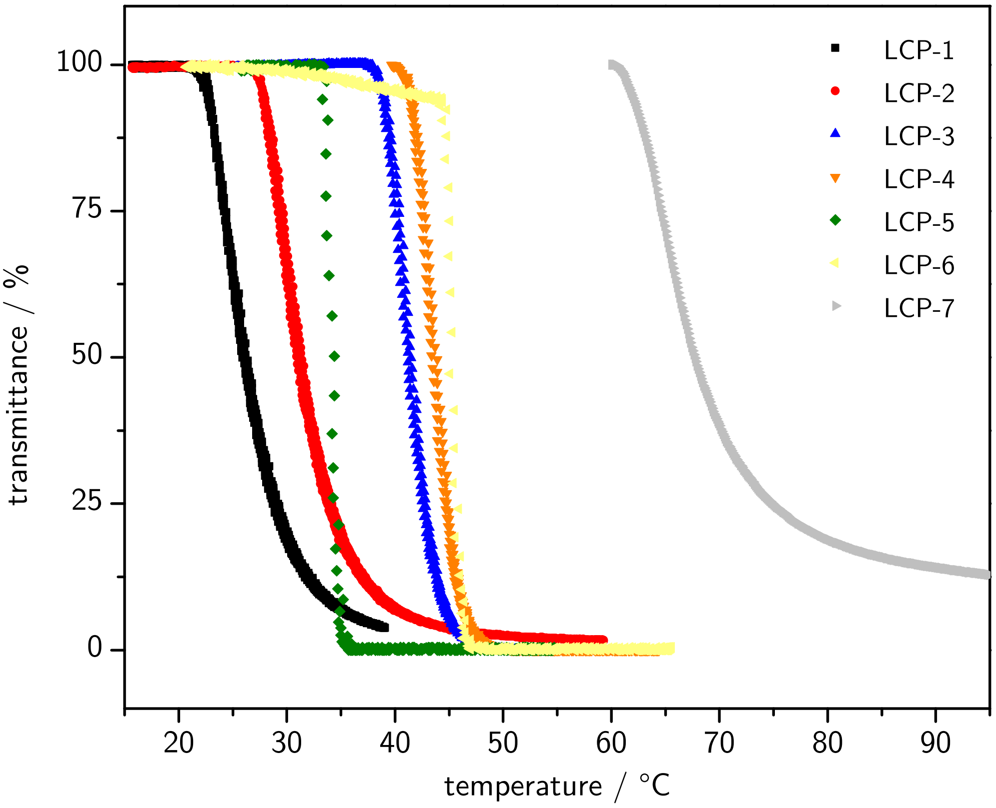

Figure 4.8: Plots of transmittance as a function of temperature (670 nm, 1 °C min^{-1}) measured for aqueous solutions (2 g L^{-1}) of a series of linear copolymers (**LCP-1** to **LCP-7**) of varying copolymer composition.

Suitable copolymer compositions out of these series were selected for the next synthetical step, namely the synthesis of cross-linked hydrogels. Copolymers with a CP over 40 °C were considered to be most suitable, as coupling of the hydrophobic biotin is going to lower the CP after polymerisation.[139] Also, varying amounts of HEMA would allow to study hydrogels with different composition and possibly different degree of functionalisation. In summary, **LCP-3** with a high HEMA-content of 70 mol-% and **LCP-7** with 7 mol-% of HEMA were chosen as candidates for hydrogel synthesis. The related experiments with cross-linked hydrogels, are described in the following section.

4.3 Cross-linked HEMA/OEGMA hydrogels

The experiences and successful preparations from linear copolymer development served as basis for the synthesis of chemically cross-linked hydrogels. Hydrogels with varying cross-linker content were prepared to study structure-property relationship properties of swollen polymer networks. Subsequently, the optimised hydrogel formulations were to be used as a matrix for the previously synthesised colloidal crystals (**chapter 3**), to produce inverse hydrogel opals.

4.3.1 Synthesis of cross-linked HEMA/OEGMA hydrogels

As a starting point for hydrogel (HG) synthesis, formulations based on **LCP-4** and **LCP-7** were selected. To adapt the synthesis from linear to cross-linked copolymers, several parameters had to be adjusted. To create polymer networks, bifunctional methacrylates were introduced to the reaction mixture as cross-linking agents.

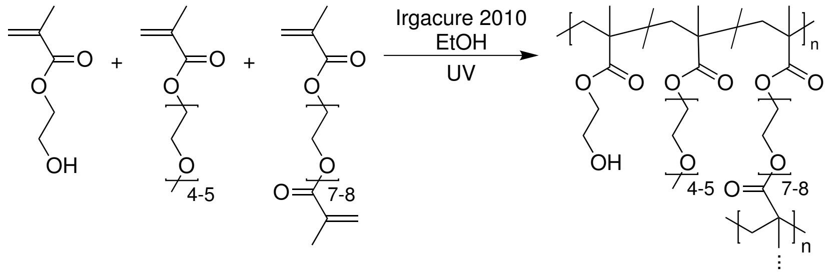

Figure 4.9: Scheme of the UV-induced radical copolymerisation of ternary hydrogels **HG-1** to **HG-6**.

To keep the desired properties of the polymer, e.g. thermoresponsive behaviour and bio-compatibility/anti-fouling properties, a cross-linker was chosen, which is chemically related to the applied comonomers. A variety of bifunctional oligo(ethylene glycol)dimethacrylates (OEGDMAs) are commercially available. OEGDMAs possess the same properties as their monofunctional equivalents, bearing hydrophilic (ethylene glycol) and hydrophobic parts (two methacrylate moieties). Therefore, polymers networks prepared with these cross-linkers maintain their thermoresponsive properties, yet the CP might be shifted. Their influence on the LCST has to be taken into account, when a hydrogel including these components is created. With these prerequisites, medium-length cross-linkers oligo(ethylene glycol) dimethacrylate M_n

= 400 g mol^{-1} ($OEGDMA_{400}$) and oligo(ethylene glycol) dimethacrylate M_n = 550 g mol^{-1} ($OEGDMA_{550}$) were selected. Although longer cross-linkers would result in more flexible hydrogels with better swellability, more EG would increase the LCST dramatically (cf. **figure 4.2**).

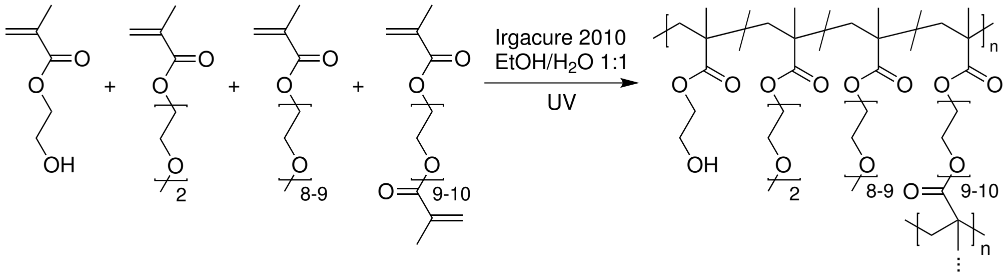

Figure 4.10: Scheme of the UV-induced radical copolymerisation of quaternary hydrogels **HG-7** to **HG-10**.

To control the dimensions of the polymer film, all polymerisations of cross-linked hydrogels were conducted in a self-built polymerisation mould. This mould was a simple assembly of two regular glass slides, which were separated by a spacer made of Parafilm® (Pechiney Plastic Packaging, USA), providing a gap of approx. 125 µm.

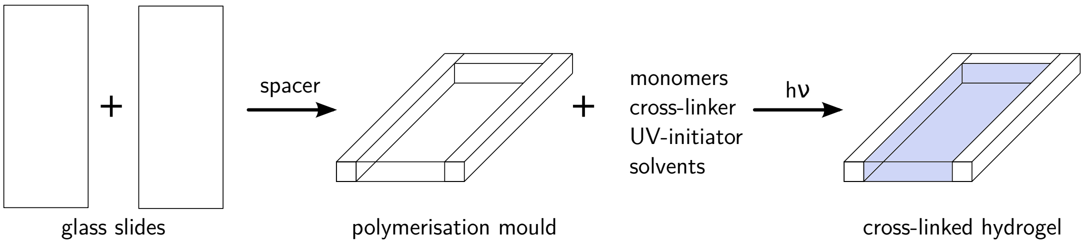

Figure 4.11: Schematic drawing of the assembled polymerisation mould and procedure used for hydrogel synthesis.

The transparent glass slides made it possible to use a near UV-initiator (Irgacure 2010, Ciba) to start the polymerisations. Injection of the reaction solutions was realised by only covering three sides of the mould with Parafilm®, so that solutions could be introduced *via* the remaining open side. When the glass slides were cleaned and hydrophilised with piranha acid prior to use (cf. **section 7.2**), capillary forces between the glass slides ensured equal spreading of the liquid. Because both glass slides were easily separable from each other after curing of the polymer, a free-standing hydrogel film could be obtained after polymerisation.

Synthetic procedures were designed after the template of Asher et al[21], who synthesised hydrogel matrices made of p(HEMA). This recipe was applied using a combination of either HEMA and $OEGMA_{300}$ or HEMA, $OEGMA_{475}$ and MEO_2MA as thermoresponsive units, as it was evaluated before with linear copolymers.

The monomers were dissolved either in water or a water/ethanol mixture (w_{monomers} = 35 wt-%), to ensure that the hydrogel polymerises in a swollen state in the mould. Otherwise, the polymer would swell after the polymerisation, when it is introduced to water. As the hydrogel was intended as matrix material for inverse opals, a swelling of the hydrogel would increase the distance between the crystal planes and therefore maybe even destroy the regular orientation of the particles. So, intensive swelling after polymerisation had to be avoided. For all synthesises including MEO_2MA, water/ethanol mixtures were used, because MEO_2MA is only sparingly water-soluble.

A relatively concentrated solution with $m(monomers) \approx \frac{1}{3}\, m_{total}$ ensures a proper cross-linking of the polymer in any case, as low concentrated mixtures tended to polymerise incompletely.

With these prerequisites, series of poly(HEMA-stat-$OEGMA_{300}$-stat-$OEGDMA_{400}$) and poly(HEMA-stat-$OEGMA_{475}$-stat-MEO_2MA-stat-$OEGDMA_{550}$) hydrogels were synthesised in the described glass mould applying UV-light of 365 nm for one hour. An overview over the composition and properties of the hydrogels is given in **table 4.2**.

The proportion of the monomers relative to each other was kept constant for all hydrogels. In HEMA-rich gels **HG-1** to **HG-6**, an increasing amount of cross-linker was added to the respective formulations with a HEMA/$OEGMA_{300}$ ratio of 70:30. Same procedure was applied for HEMA-poor gels, **HG-7** to **HG-10**, with a proportion of HEMA/$OEGMA_{475}$/MEO_2MA of 10:85:15.

4.3.2 Stability and swelling of HEMA/OEGMA hydrogels

Mechanical stability of the free-standing films was highly dependent on the cross-linker content. While a cross-linker amount around 5 wt.-% produced very soft and flexible films, cross-linker proportions above 20 % resulted in hard and brittle films. Both extremes are not desirable due to several reasons.

The principle demand on an OEGMA-based hydrogel seemed to be fulfilled with

Table 4.2: Composition and appearance of various p(HEMA-stat-OEGMA$_{300}$-stat-OEGDMA$_{400}$) and p(HEMA-stat-OEGMA$_{475}$-stat-MEO$_2$MA-stat-OEGDMA$_{550}$) hydrogels cured by UV-induced polymerisation in a glass slide mould.[a]

	χ^b						
	HEMA	OEGMA$_{300}$	OEGMA$_{475}$	MEO$_2$MA	OEGDMA$_{550}$	SR[c]	appearance
HG-1	70	30	0	0	1.5	n/a[d]	soft
HG-2	70	30	0	0	3	n/a[d]	
HG-3	70	30	0	0	5	3.8±0.2	
HG-4	70	30	0	0	10	3.1±0.3	
HG-5	70	30	0	0	20	n/a[d]	brittle[e]
HG-6	70	30	0	0	30	n/a[d]	
HG-7	8.5	0	13	72	6.5	n/a[d]	soft
HG-8	8	0	12	70	10	n/a[d]	
HG-9	8	0	11.5	65.5	15	2.9±0.2	flexible
HG-10	7	0	11	62	20	2.3±0.1	

[a] Conditions: w_{monomers} = 35 wt-%, UV-initiator Irgacure 2010 (w = 1.5 wt-% relative to monomers), irradiation (365 nm, 400 W) for one hour.

[b] Molar fraction in monomer feed.

[c] Swelling ratio at room temperature.

[d] Not determinable, due to mechanically unstable film.

[e] No continuous film obtained.

cross-linker ratios between 5 and 20 wt.-%: a) a pronounced mechanical stability, so free-standing HG films can be handled without rupture; b) pronounced flexibility and swellability, so that a significant amount of water can be taken up by the hydrogel. Unfortunately, stability and swellability are opposing properties. The former is achieved by a high cross-linker content, while the latter is favoured by a low cross-linker amount. This relationship between cross-linker content and swellability was described e.g. in the Flory-Rehner-Theory[140, 141]. With the intermediate cross-linker proportions, a good compromise between stability and high water-uptake was achieved.

$\chi_{cross-linker} \leq 3$ mol-%	$\chi_{cross-linker} \geq 20$ mol-%
• highly flexible and swellable	• little flexible and swellable
• mechanically unstable (too soft)	• above 20 mol-% too brittle

Unfortunately, it was not possible to determine swelling ratios for all HGs. Since swelling ratios were determined gravimetrically (cf. **section 4.1.1.2**), a certain mechanical stability was needed to handle the films. On the one hand, film with cross-linker ratios below 5 mol.-% were too soft to be handled manually without destroying the samples. Highly cross-linked samples above 30 mol.-%, on the other hand, were already breaking apart, when the mould was removed. So it was not possible to reliably determine the weight of either of these samples.

For **HG-1** to **HG-6** with a high HEMA content, the intermediate cross-linker contents of 5 and 10 wt.-% resulted in swelling ratios of 3.8±0.2 and 3.1±0.3 respectively. As expected, the swelling ratio decreases with increasing cross-linker content, in this case by 25 %. A similar trend, but lower absolute swelling ratios were determined for **HG-7** to **HG-9**. Here, films with a cross-linker content $\leq$ 10 % were not mechanically stable enough to measure swelling ratios.

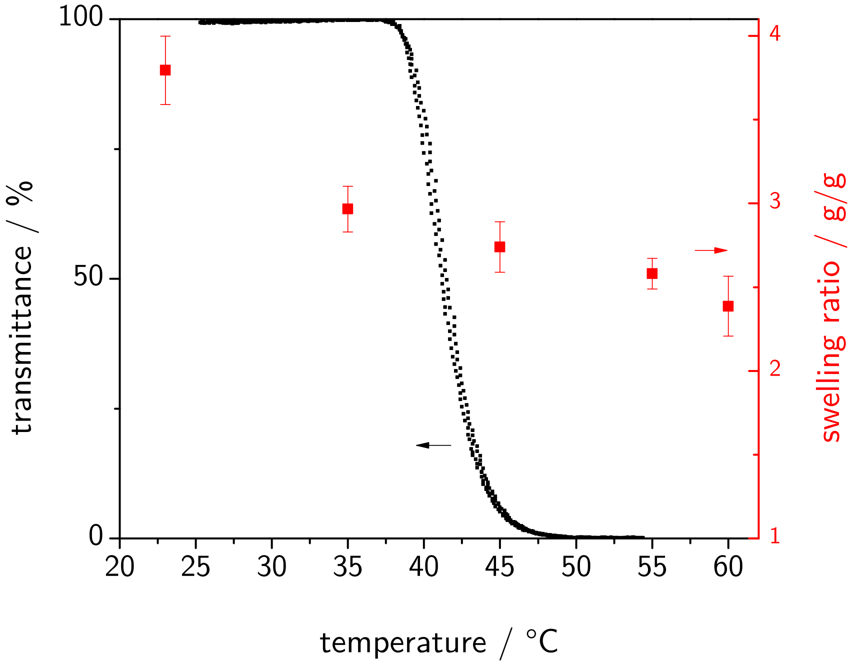

Figure 4.12: Comparison of the turbidity curve of **LCP-3** (black) with the swelling ratio plot of **HG-3** (red).

When comparing the swelling ratio of the cross-linked hydrogel **HG-3** with the CP of the linear copolymer **LCP-3** (cf. **figure 4.12**), it is obvious that the deswelling of **HG-3** with increasing temperature does not display a sharp transition, which is present in the case of the linear copolymers. A first hypothesis might attribute this behaviour to the cross-linked nature of the hydrogel, somehow interfering in the coil-to-globule transition, which can occur unimpeded in the linear copolymer.

Although this consideration might be comprehensible in the first place, the broad transition for cross-linked materials seems to be a special property of OEGMA (co)-polymers, which display a (de)swelling over a broad temperature range. Hydrogels prepared from PNiPAam instead of OEGMA, do not show this broad swelling transition, but also sharp deswelling at the CP.[142]

Ma and coworkers[137] described PNiPAam microgels cross-linked with 2 wt.-% OEGDMA, which showed a sharp thermal transition. The transition broadened, when the length of the cross-linker exceeded 14 ethylene glycol units. A similar observation was found be Cai and coworkers[143]. Here, the more OEGMA was incorporated in p(OEGMA-co-MEO$_2$MA) microgels, the broader the thermal transitions became.

These findings suggest, that the higher the EG content of the copolymer is, the broader its transition profile will be in the end. Recent results of loosely cross-linked p(OEGMA) films, which also show broad transitions, support this hypothesis.[138]

When comparing temperature dependant swelling ratios of representatives of either of the two hydrogel series, the trends are similar. Both (de)swelling curves in **figure 4.13** decrease over the entire temperature range that was examined, without an abrupt decrease in swelling ratio at the CP. For application in responsive IHOs, the broad transition period is not necessarily an exclusion criterion. A broad transition can even be advantageous. Instead of only switching at a certain temperature, a broader range of temperature can be sensed. When biomolecular sensing is targeted, one of the important parameters is the impact of the bound analyte molecule on the thermoresponsive properties of the matrix hydrogel. If binding of an analyte reduces or increases the hydrophilic nature to a sufficient extent and therefore is able to shift the Bragg signal of the IHO, then also a broad transition can be tolerated for this application. More details on applicability of the presented hydrogel films are described in the following chapter. The developed stable hydrogel films with high (**HG-3**) and low (**HG-10**) HEMA content were applied as a matrix material between the colloid

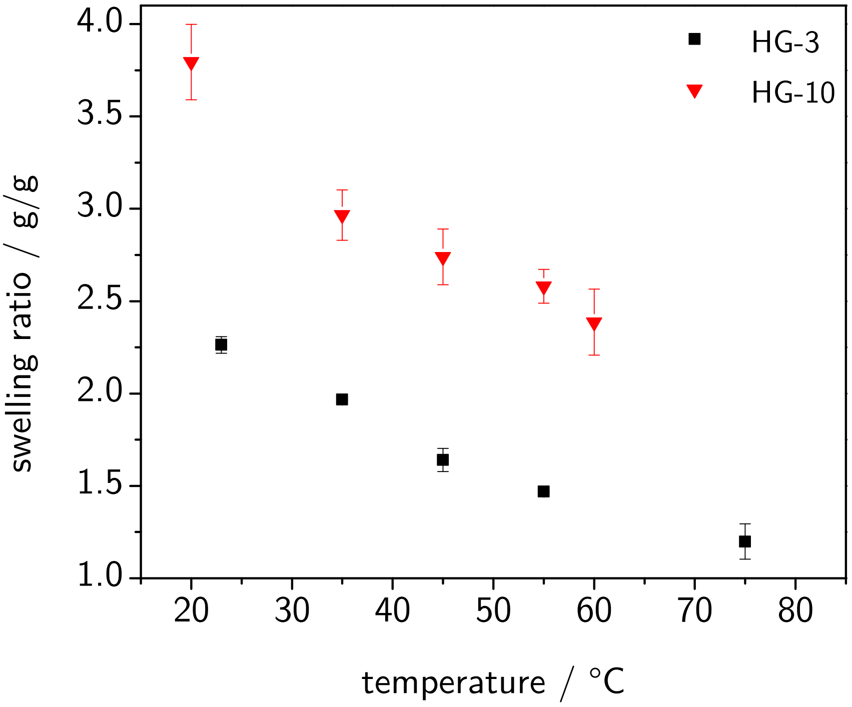

Figure 4.13: Comparison of temperature dependant swelling ratios of **HG-3** (black squares) and **HG-10** (red triangles).

crystals presented in **chapter 3**, for the assembly of inverse hydrogel opals.

5 Inverse hydrogel opals

It was described in the previous chapters, that there is a necessity to embed the assembled colloidal crystals in a hydrogel matrix for a) mechanical stability and b) for the introduction of a responsive material for the sensing of temperature and (bio)-molecules. For this purpose, responsive hydrogels with functionalisable hydroxyl groups were synthesised, which was described in **chapter 4**.

The following chapter describes, how colloidal crystals and responsive hydrogels are combined to obtain inverse hydrogel opal (IHO). The process of IHO preparation, their optical analysis as well as functionalisation with targeting units and the response to analytes is described.

5.1 Creating inverse opals

The optical properties of inverse opals are very similar to those of colloidal crystals, as shown in **chapter 3**. The main difference lies in the composition of the material. While colloidal crystals consist of organic or inorganic particles surrounded by air or solvent, the composition of inverse opals is the other way round, which is implied by the term *inverse*. In inverse opals, particles are etched and therefore replaced by either air or solvent, while the matrix around the cavities is mostly comprised of polymers, silica or other suitable materials. When hydrogels are used as scaffold material, the materials are called inverse hydrogel opals (IHOs).

As stated earlier, optical properties of IHOs are similar to colloidal crystals. This includes the possibility of Bragg diffraction of visible light, if the prerequisites are met (cf. **section 3.2**). One of the crucial parameters to satisfy Bragg conditions, is the refractive index contrast between the matrix and the cavities. In case of IHOs, which are to be used in aqueous media, this is especially delicate. Since both the hydrogel matrix and the cavities will contain water when the material is put into application, there is the danger that the refractive index contrast becomes too low. In the worst case, no Bragg diffraction will then occur.

The presence of water in the cavities improves properties like diffusion of (analyte) molecules through the porous system. Since the pores of such IHOs are in a size range of several hundreds of nanometres, even rather big molecules such as proteins or viruses can be expected to diffuse through the material. For the application as sensors this is advantageous, as analyte molecules need to be distributed to the actual binding sites inside the porous IHO to bind to a high number of targeting sides, which induces a change in the hydrogel state to manipulate the plane distances in the opal structure.

Another advantage of a porous architecture is the enlarged surface area. This is beneficial for the functionalisation with binding groups as well as for the recognition of analytes. Also, a diffusion of molecules into the interior of the hydrogel is supported. In contrast to non-porous materials, there are much more possibilities for molecules to penetrate into the dense hydrogel.

For the creation of inverse opals, there are in principle two different approaches, which are applied in literature:

1. one-step assembly processes, where the deposition of colloidal particles is performed in a suspension of the matrix material,[34, 88–90, 100]
2. two-step assembly processes, where previously assembled colloidal crystal are infiltrated with a solution of the matrix material.[19, 20, 26, 35, 37, 39, 47, 144–155]

In one-step processes, particles are directly suspended in a medium containing the matrix monomers. With this suspension, colloidal self-assembly and curing of the matrix material is done principally in one step. The principle of these assembly methods was described in **chapter 3**, as these methods also include a colloidal crystal assembly approach, which was covered in that chapter.

Two-step assembly methods are the more versatile approach. In this method, colloidal crystals are deposited first, e.g. by vertical deposition (cf. **section 3.1.1**). The assembled array of dry particles is subsequently infiltrated with a solution containing all compounds that are needed to created a stable matrix around the colloid crystal. This can be e.g. either methacrylic monomers and cross-linkers for organic polymer matrices or self-condensing silicon sources like TEOS for inorganic silica networks. When colloidal crystals have been successfully infiltrated with the matrix-solution, the cross-linking reaction is induced and binary materials of colloidal crystals embedded in a matrix network are obtained.

Typically when inverse opals are prepared, the matrix material is chosen to be of different chemical nature than the particles. Otherwise it is impossible to only etch/dissolve the particles after build-up of the surrounding matrix. Also, it is difficult to account for a refractive index contrast, if the materials are too similar.

When particles are etched, only the matrix material remains and the colloids are “replaced” by cavities. The cavities are filled with the surrounding medium, which is either air or a liquid, in which the inverse opals are placed. In the case of biomolecular sensing, mostly aqueous media are used.

In case of polymeric colloidal particles made from PS or PMMA, organic solvents such as chloroform or tetrahydrofuran (THF) are applied to etch the non-crosslinked particles (depending on the polymer type). Silica particles can be readily etched with aqueous HF solution. In all cases, the matrix material has to be resistant against the introduced etching chemicals. Chemically cross-linked organic polymer networks are resistant against both types of etching agents, which makes them a suitable matrix material for a variety of applications.

Polymer matrices have the advantage of high versatility compared to silica networks. With a wide range of possible monomers to choose from, material properties can be varied e.g. concerning hydrophilicity, mechanical properties or functionality, just to name a few. Also, matrices from polymers can be constructed to be “smart”, by selecting polymers which are able to react to outer stimuli (cf. **chapter 4**).

One of the advantages of the two-step process is its versatility. The restrictions for the one-step process are quite tight, as additional parameters such as viscosity have to be precisely met for successful particle assembly which makes it unfavourable for highly-diluted compositions. Because the infiltration process is much more tolerant towards compositional variations, this approach was chosen for this work. In the following section, the actual IHO development performed during this work starting from assembled CCs is shown and discussed.

The two-step inverse opal preparation is schematically visualised in **figure 5.1**, starting from an organised CC template, followed by precursor infiltration and curing. Finally, the particles are etched and an inverse opal structure is obtained.

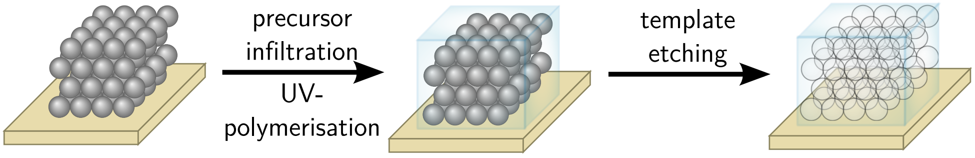

Figure 5.1: Scheme of the preparation of an inverse hydrogel opal *via* a two-step template infiltration and particle etching.

5.2 Synthesis of inverse hydrogel opals

Starting from self-assembled colloidal crystals, hydrogels with recipes previously developed were polymerised around the particles to create a responsive hydrophilic material. The IHOs were expected to show Bragg diffraction in a similar manner as its template material.

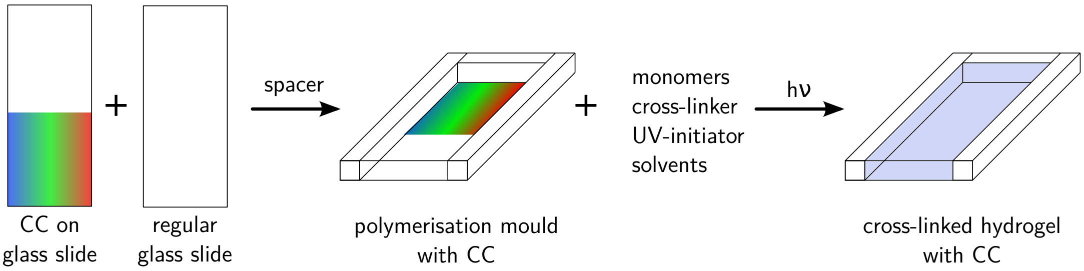

Figure 5.2: Schematic drawing of the procedure of monomer infiltration into a colloidal crystal followed by curing with UV light.

The synthesis was performed in the same polymerisation mould as the previously described hydrogel films. The only difference was, that one of the glass slides forming the mould, was coated with a colloidal crystal. When the polymerisation solution was injected into the mould, the free space in-between the silica spheres was filled by the polymerisation solution containing monomers, cross-linker and UV-initiator.

During injection of the polymerisation solution, the apparent Bragg diffraction vanished as soon as all the space between the particles was infiltrated with solution. The difference in refractive index between silica ($n \approx 1.45$)[156] and monomer solution was not pronounced enough and so the prerequisites for Bragg diffraction were not fulfilled anymore (cf. **section 3.2**). The same observation was made after UV-polymerisation of the hydrogel films, as the refractive index changes hardly after curing.

Table 5.1: Composition of prepared inverse hydrogel opals, assembled around **CC-7** templates.

	$d_{\mathrm{SiO}_2}{}^a$/			χ^b		
	nm	HEMA	OEGMA_{300}	OEGMA_{475}	$\mathrm{MEO_2MA}$	OEGDMA_{550}
IHO-1	400	70	30	0	0	5
IHO-2		7	0	11	62	20

[a] Average diameter of the silica template particles as determined by DLS, SEM and AFM.
[b] Molar fraction in monomer feed.

Table 5.1 presents the compositions of the synthesised inverse hydrogel opals. Both preparations are derived from recipes developed and described in **chapter 4**, namely HEMA-rich **HG-3** and HEMA-poor **HG-10**. The colloidal crystals, which were used as a template, were fabricated following the formulation of **CC-7**, described in **chapter 3**. Both types of IHOs were templated by the silica particles with a diameter of approx. 400 nm.

The absolute thickness of the synthesised IHOs was identical to previously created pure HG films with approx. 125 µm. Since the assembled colloidal crystal templates had a vertical spread of only approx. 5 µm, only the bottom 4 % of the IHO films consist of the structured, optically active part.

To restore the conditions for Bragg diffraction, the silica particles were etched using aqueous HF solution (2 wt.-%). Hydrogel films were placed in the HF solution overnight to remove all silica traces and were subsequently repeatedly washed with ultra-pure water.

Already during HF treatment, the opalescent reflections, which were visible on the dry colloidal crystals, were restored after removal of the silica colloids. The new refractive index contrast of water in the cavities of the porous IHO structure to the

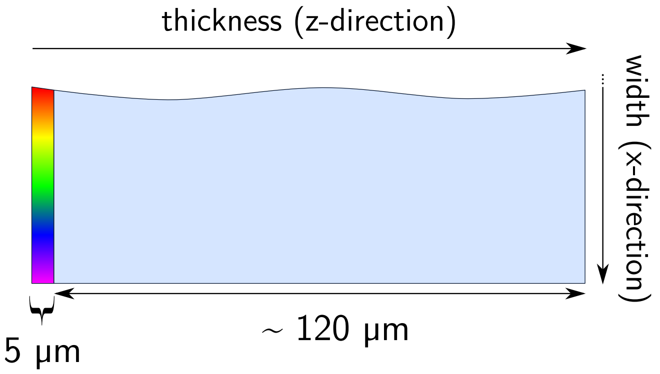

Figure 5.3: Schematic dimensions of the opalescent (multi-coloured) and sheer hydrogel (pale blue) part of an IHO film, which were synthesised in this work.

polymer/water mixture in the matrix hydrogel was sufficient for distinct opalescence.

The photograph in **figure 5.4** shows a cut sample from **IHO-2** floating on water. The IHO was illuminated from the side with a conventional LED flash light. The reflected blue colour of the IHO film originates from an acute angle, from which the sample was illuminated (cf. angular dependency of Bragg diffraction in **section 3.2** and **3.6.2**). The spectral properties of this bright opalescence were evaluated and are described in the following section.

5.3 Analysis of inverse hydrogel opals

5.3.1 UV/Vis transmission spectroscopy

Analogous to the UV/Vis transmission experiments with bare silica colloidal crystals (**section 3.3.4**), the optical absorption of chemically etched inverse hydrogel opals was evaluated in a measuring setup with the light beam orthogonal to the IHO surface. In contrast to the colloidal crystals, where the deposited materials on glass slides were analysed in ambient atmosphere, the analysis of hydrogel films was performed in water. First of all, measuring in water guaranteed a constant degree of swelling of the film, which is directly affecting the wavelength of the Bragg diffraction peak due to shrinking or widening of the IHO pores.

Secondly, the constant aqueous environment made it also possible to determine the

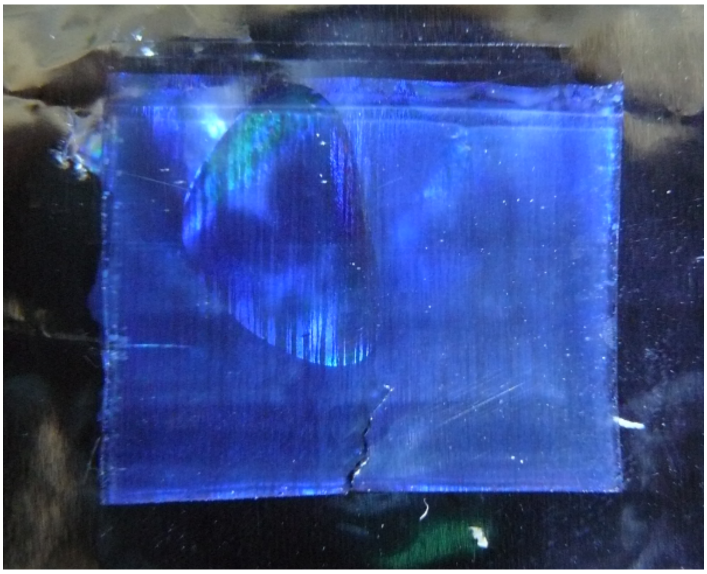

Figure 5.4: Photograph of **IHO-2** floating on water, illuminated from the side with white light. Size of the sample approx. 25 mm × 20 mm.

thermoresponsive behaviour of the material, following the shift of the Bragg diffraction peak with temperature. Keeping the hydrogel film in constant contact with water prevents a complete dry out and destruction of the film at elevated temperatures.

To facilitate the UV/Vis analysis in water, films were placed in a low volume cuvette consisting of two quartz windows with a recess in-between. With a distance of only 0.5 µm between the cuvette windows, it was possible to fix the films in an upright orientation, which ensured a measuring angle of 90° in respect to the film surface. This setup allowed to determine UV/Vis absorption properties of etched inverse hydrogel opals in water with respect to temperature (for details of the applied apparatus and tempering device consult the experimental part).

A plot of the temperature dependant UV/Vis absorption of HEMA-rich **IHO-1** is presented in **figure 5.5**. When the temperature is elevated from 10 °C to 80 °C, the band gap is blue-shifted by 70 nm from 835 nm to 765 nm. When increasing the temperature, more and more water is expelled from the thermoresponsive polymer network, which leads to a shrinking of the hydrogel. This effect was already evaluated with swelling ratio measurements for sheer hydrogel films (**section 4.3.2**). Shrinking of the hydrogel films reduces their size in all three spatial directions and therefore reduces the size of the cavities in the porous inverse opal part of the material.[157–159] The reduced pore diameter causes a blue-shift of the band gap wavelength, since

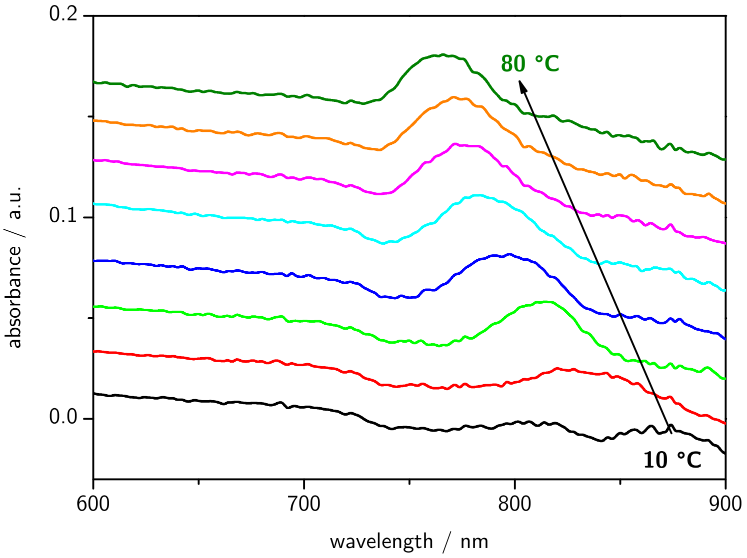

Figure 5.5: Plot of temperature dependant UV/Vis absorption measurements in ultrapure water of **IHO-1**. The spectra are vertically staggered for better readability.

the diameter directly influences the distance between diffraction planes (e.g. a_{111}) and therefore the Bragg diffraction wavelength (cf. **chapter 3**).

When comparing the intensity of the various absorption spectra, the absolute intensity is increased when increasing the temperature. This is an effect, which is also created by the thermoresponsive polymer network. At low temperatures, the hydrogel is highly swollen with water. In case of **IHO-1**, the system contains approx. 75 % of water at 20 °C, estimated from swelling ratios. The more water is present in the hydrogel, the closer the refractive index of the polymer/water system is to the refractive index of water and therefore, the lower the difference between these two. Since Bragg diffraction is depending on a refractive index contrast between the aligned particles (or cavities for inverse opals) and the matrix material, the refractive index pair which has to be regarded for inverse hydrogel opals in water, is water and a water/polymer mixture.

The effective refractive index of mixtures n_{eff} can be estimated from the volume fraction Ψ and refractive index n of the material components in the hydrogel:

$$n_{eff} = \sum_i \Psi_i \, n_i \tag{5.1}$$

From **equation 5.1**, the effective refractive index of a hydrogel comprising of 75 % of water is estimated as 1.37 ($n_{methacrylates} \approx 1.49$), which yields a refractive index contrast to water ($n_{H_2O} = 1.33$) of $\Delta n = 0.04$. With increasing temperature the water content of the hydrogel is lowered and therefore, n_{eff} shifts towards $n_{methacrylates}$. Thus, the band gap and the intensity of the absorption spectra increases.

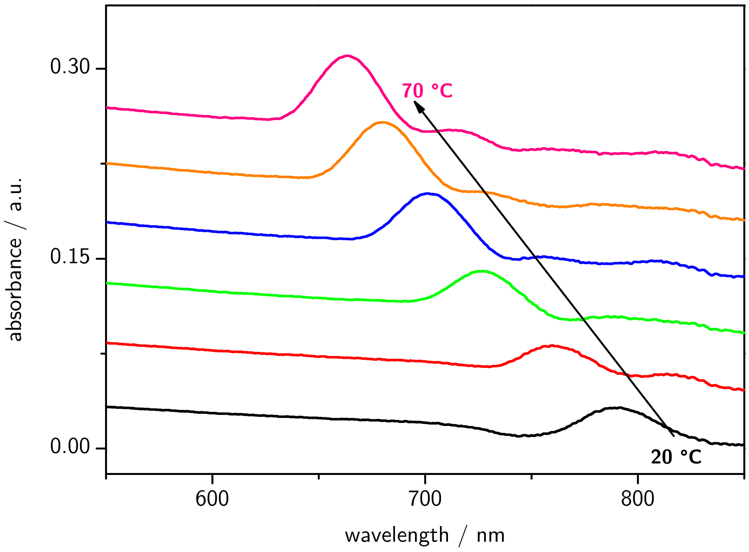

Figure 5.6: Plot of temperature dependant UV/Vis absorption measurements in ultrapure water of **IHO-2**. The spectra are vertically staggered for better readability.

The plot of temperature dependant UV/Vis absorption spectroscopy for HEMA-poor **IHO-2** is depicted in **figure 5.6**. The series evolves in the same manner as the HEMA-rich **IHO-1**, displaying a red-shift with increasing temperature. Though, some differences should be noted.

First of all, the absolute shift of the band gap wavelengths with temperature is more pronounced for **IHO-2** than for **IHO-1**, with a magnitude of 130 nm from 20 °C to 70 °C. Also, the intensity of the Bragg peak is higher for **IHO-2** than for **IHO-1**. The difference in refractive index between both IHOs is based on the same feature, which is also responsible for the increase in intensity within the **IHO-2** series: **IHO-2** possesses a higher refractive index compared to **IHO-1**, as it swells less than **IHO-1** (cf. **section 4.3.2**). Because the hydrogel matrix contains less water, the refractive index contrast Δn between **IHO-2** and water in the cavities is more pronounced.

The evolution of the band gap wavelengths of **IHO-1** and **IHO-2** with respect to temperature is depicted in **figure 5.7**. The absorption maxima are fitted with a cubic

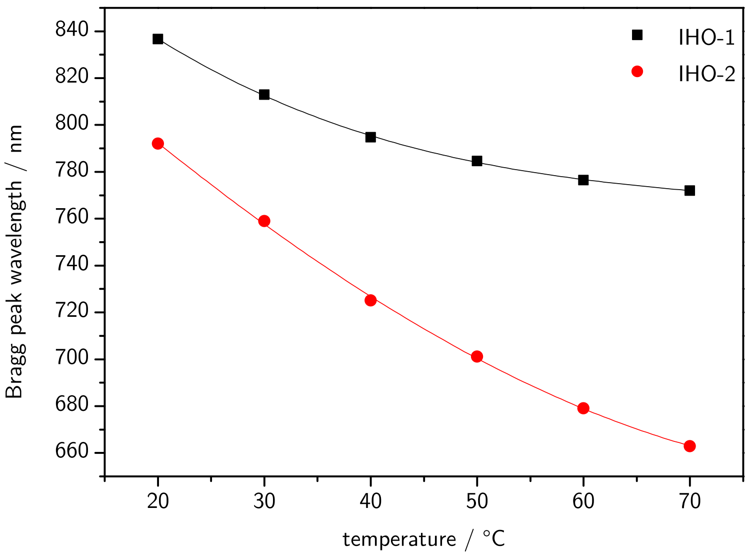

Figure 5.7: Plot of Bragg peak wavelength (λ_{max}) relative to temperature for **IHO-1** (black squares) and **IHO-2** (red circles). For both series, a cubic fit was applied.

polynomial regression, since swelling/shrinking of free-standing hydrogel films is supposed to occur equally in all three spatial directions.

Comparing the band gap wavelengths of both IHOs at room temperature with the absorption of the bare colloidal crystal (**figure 3.11**), which shows a band gap at 800 nm, especially **IHO-1** differs from this value (by approx. 40 nm), while the band gap of **IHO-2** is in the same range.

The shift of the band gap of **IHO-1** compared to the colloidal crystal template **CC-7** is an indication for swelling of the hydrogel after polymerisation around the silica template, which widens the pores of the inverse opal. Since **IHO-2** is less prone to extensive swelling due the higher cross-linker content, the diameters of the pores and therefore crystal plane distance a_{111} is steady compared to the template **CC-7**.

The second difference between the band gap wavelengths of both IHOs, is the magnitude of the decrease in Bragg diffraction peak wavelengths with increasing temperature. The absolute shift of the band gap wavelengths is smaller for **IHO-1** compared to **IHO-2** (70 nm compared to 160 nm) from 20 °C to 70 °C. Therefore, the evolution of **IHO-1** is much flatter and reaches a plateau after 50 °C. Such a plateau is not observed for **IHO-2**. The reason for this difference is the higher cloud point of **IHO-2** (cf. **LCP-3** and **LCP-7** in **section 4.2**), which possibly shifts the plateau over 70 °C and out of the range of the investigation. In summary, the higher CP of **IHO-2** leads to a more pronounced band gap shift with respect to temperature, without a noticeable plateau until 70 °C.

5.3.2 Scanning electron microscopy

The presence of Bragg diffraction peaks in UV/Vis absorption measurements as well as the opalescent appearance of the IHOs already indicated that the regular structure from the assembly of colloid crystals was preserved after etching of the particles. To verify the integrity of the structural order as well as to illustrate the hollow hydrogel network, scanning electron microscopy analogous to the investigations of the colloid crystal templates was performed.

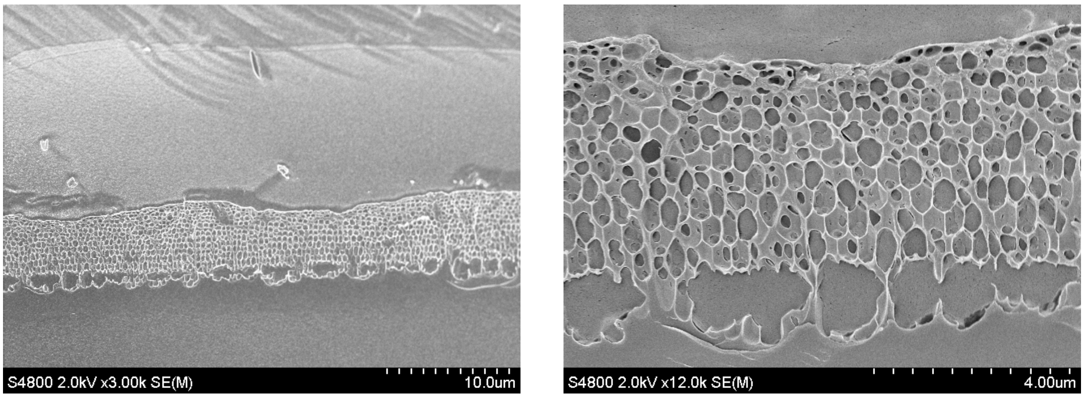

(a) (b)

Figure 5.8: SEM micrographs of an inverse hydrogel opal after platinum sputtering. Scale bar is given below the micrographs. For details on sample preparation and execution of the analysis see experimental part.

Looking first at the micrograph with the less magnified etched hydrogel in **figure 5.8(a)**, the structural order of the colloidal crystal template was preserved after etching. The pores are aligned regularly over a long range in the hydrogel film. Like in the colloidal crystals imaged before, this order is responsible for the opalescence of the hydrogel film.

When looking more into detail at the IHO in the micrograph with higher magnification in **figure 5.8(b)**, the identification of a regular alignment is more difficult than in the lower magnified **figure 5.8(a)**. As the film was first freeze-dried and then freeze-fractured, a rough fracture instead of a clear cut was generated. Therefore, instead of a single plane, several different "crystal" planes are visible (cf. **figure 3.9** for micrographs of unetched opals). This gives the impression of randomly distributed pores instead of an aligned material.

Regarding pore size of the IHO in the horizontal dimension, pore diameters are comparable around 400 nm. The size is in good agreement with the diameter of the template particles, which was determined *via* SEM, AFM and DLS (cf. **table 3.2**). A pore size which is similar to the size of the silica template proves, that there was no pronounced swelling of the film after polymerisation. This was one of the prerequisites when designing hydrogel synthesis, since a distinct swelling after polymerisation would have changed the distance between crystal planes and therefore the wavelength of Bragg diffraction patterns. Since particle size is already at the maximum for the chance of creating Bragg diffraction in the visible range, an additional widening of the pores due to swelling after polymerisation was strongly to be avoided.

When looking at the vertical distribution of the pores, the picture differs from the horizontal direction. Here, pores are increasingly elongated from top to bottom resulting in a change of pore geometry from a spherical to a hexagonal orientation. The pores in the lower part of the micrograph are stretched by nearly twice their diameter, resulting in pore diameters in vertical direction of 730 nm. The extension in the horizontal direction is much less pronounced, with a widening of only 5 % corresponding to 420 nm as a total pore size.

Since the extension of pore sizes is nearly only distinct in vertical direction, this distortion of the IHO is possibly attributed to a vertically oriented stress, which also created ruptures in the film at the very bottom of the hollow structure. The origin of the stress is not easily determined, so only assumptions can be made. The stress which led to film elongation and rupture must have occurred either when etching the silica template, or during sample preparation for SEM, since SEM micrographs of unetched samples did not reveal any film ruptures (cf. **figure 3.9**).

Potentially, introducing aqueous HF to the film and etching silica particles induces a stress on the film e.g. by swelling or shrinking of the film which damages part of the film. Nevertheless, the ruptures are only present at the hydrogel/air interface while most of the film is still intact, displaying pronounced Bragg diffraction.

In electron micrographs it is visible that the pores are not isolated from each other, but that they are interconnected. These connection points between the pores are possibly a result of silica particles touching each other during colloidal crystal assembly. At these touching points, all space is occupied by the silica particles and therefore the hydrogel cannot be formed at these connection points, leading to holes in the walls of the pores. The diameter of the connections varies from 170 nm to 290 nm, with higher propensity of larger sized connection point in the lower part of the IHO (referring to the SEM micrographs), possibly due to the vertical elongation of the film.

The interconnection of the pores is beneficial for the diffusion of the solvent and especially of dissolved (bio)-molecules through the material. If the hydrogel itself is too dense (cf. **section 5.3.3**) to allow diffusion of molecules through network, connected pores favour the diffusion of molecules into all parts of the structure part of the IHO. Without an equal distribution of analyte molecules in the IHO, a proper sensing would be impeded.

5.3.3 Calculation of mesh sizes

From swelling ratios, which were determined for the hydrogels, it is possible to calculate the mesh size of polymer networks. According to studies by Peppas *et al.*, the mesh size ξ of hydrogels is proportional to the cross-link distance r the in non-swollen state.[160, 161] An estimation of the mesh size can be calculated with the following formulas:[7]

$$r = d_{C-C}\,(2N_C)^{1/2}\,C_n^{1/2} \tag{5.2}$$

$$\xi = r\,SR^{1/3} \tag{5.3}$$

The variables used in these equations are the length of a C−C single bond ($d_{C-C} = 0.154\,\text{nm}$) and the characteristic ratio C_n. Peppas *et al.* determined C_n for p(HEMA) as $C_n = 6.9$[160]. C_n is approximately equal for all methacrylates, so this value was used for the calculation of mesh sizes for all hydrogels in this work.

---

[7] The formulas were simplified by Dr. Jens Buller[142]

The number of monomer units between two cross-links N_c can be directly determined from the cross-linker ratio χ_{OEGDMA} in the feed. Here an ideal network has to be assumed: 1. quantitative turnover in the polymerisation reaction, 2. an equal distribution of cross-linker in the polymer network and 3. only "true" cross-links without loop formation are formed. Under these assumptions, the number of monomer units between to cross-links N_c can be calculated as follows:

$$N_C = \frac{1}{2\,\chi_{OEGDMA}} \tag{5.4}$$

With these equations, the mesh sizes for the synthesised hydrogels were calculated.

Table 5.2: Calculated mesh sizes for selected swollen hydrogels.

HG	χ_{OEGDMA} / %	SR	N_C	ξ / nm
HG-3[a]	4.5	3.8±0.2	11.0	3.0
HG-4	9.1	3.1±0.3	5.5	2.0
HG-9	15.0	2.9±0.2	3.5	1.5
HG-10[b]	20.0	2.3±0.1	2.5	1.2

[a] Corresponds to **IHO-1**.
[b] Corresponds to **IHO-2**.

Regarding the mesh sizes from **table 5.2**, all hydrogels presented here are composed of a rather dense network with mesh sizes below 3 nm. Proteins typically are in a size range of several nanometres, the model protein avidin has a size of 4 × 8 × 7 nm in the crystal.[162] This indicates, that the polymer networks are probably too dense for the diffusion of biomolecules into the inner part of the hydrogel film.

To tune the mesh sizes towards a more widely-meshed network, lower cross-linker ratios need to be used. This conflicts with the stability of the hydrogel films, which was only achieved with a certain amount of cross-linker (cf. **section 4.3.2**). So a widening of the meshes by reducing the cross-linker ratio could not be facilitated with the hydrogel films synthesised in this work.

Nevertheless, diffusion of biomolecules should be possible through the hollow inverse opal structure. Here, pore sizes of several hundred nanometres and interconnection between the pores (in a smaller size range) should be beneficial for the diffusion of analytes into the interior of the hollow IHO. As the response of the material to the outer stimuli (e.g. binding of (bio)-molecule) has to take place in the opal part to induce a visual response, the permeability of the opal regime is of a much higher importance than that of the dense hydrogel material (cf. **figure 5.3**).

5.4 Functionalisation of inverse hydrogel opals

For the possible application as biosensors, the presented IHOs were functionalised with targeting groups to specifically bind corresponding (bio)-molecules. The functionalisation was carried out by post-polymerisation modification of the hydrogels, applying active ester chemistry at the hydroxyl group of HEMA.

5.4.1 Coupling of 3'-(carboxyethyl)-4'-hydroxyazobenzene-2-carboxylic acid

A first test reaction for evaluating the coupling reaction was carried out with the dye 3'-(carboxyethyl)-4'-hydroxyazobenzene-2-carboxylic acid (abbreviated HABA-propionate), a derivative of the commercially available 4'-hydroxy azobenzene-2-carboxylic acid (HABA). The synthesis of this compound was performed by Dr. Jens Buller after the published route by Hofstetter *et al.*[163] and was kindly donated.

The evaluation of the coupling efficiencies when functionalising cross-linked insoluble polymers is always a challenge. In contrast to soluble polymers, the standard methods for determining coupling efficiency as NMR or size exclusion chromatography (SEC) cannot be applied due to the insolubility of the hydrogel film. To facilitate the analysis of the functionalisation, the dye molecule HABA-propionate was coupled, before further reactions with biotin were performed. The advantage of applying a dye molecule is the ability of a direct read-out after coupling *via* UV/Vis absorption measurements.

HABA-propionate was coupled to the hydroxyl groups of the hydrogel *via* Steglich esterification at standard conditions in a dichloromethane (DCM)/dimethylformamide

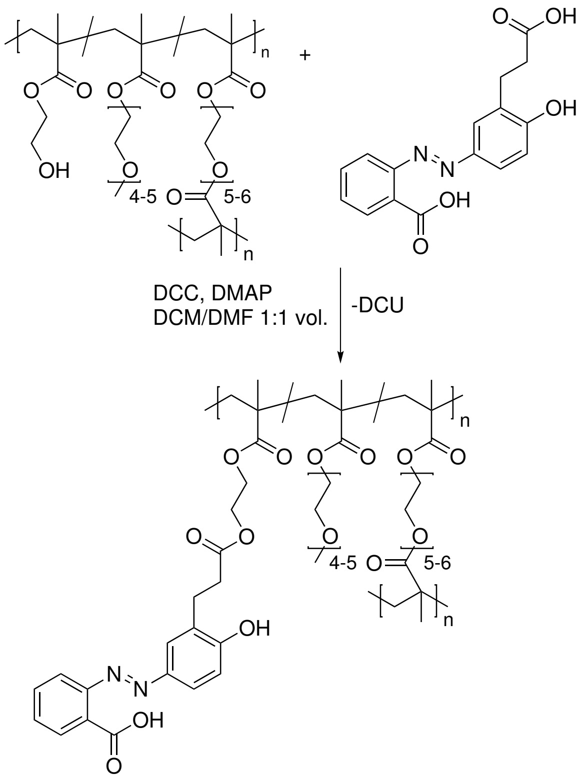

Figure 5.9: Scheme of HABA-functionalisation of IHOs, exemplarily shown for **IHO-1**.

(DMF) mixture with *N,N*'-dicyclohexylcarbodiimide (DCC) as coupling agent. HABA-propionate possesses two carboxyl moieties. Though a priori both can react with hydroxy functionalities under Steglich conditions, in practice, the propionate (in ortho position to the phenol, cf. **figure 5.11**) is more reactive than the benzoic acid moiety. The esterification will therefore predominantly occur at the propionate position.

After successful coupling of HABA-propionate to **HG-3**, the hydrogel was thoroughly washed with DCM, DMF and $0.1\,\mathrm{mol\,L^{-1}}$ aqueous NaOH to remove any physically absorbed dye from the hydrogel film. After several washing cycles, the film stayed dark orange to brown coloured, while the washing solvents were clear.

When introducing the film to (ultra-pure) water, pronounced curling of the polymer indicated an increased hydrophobicity of the film, as HABA-propionate is a rather hydrophobic molecule. Observation with bare eyes, as well as with UV/Vis spectroscopy, indicated a distinct amount of HABA-propionate, that was bound to **IHO-1**.

Quantitative determination of coupling efficiency to cross-linked HGs *via* UV/Vis

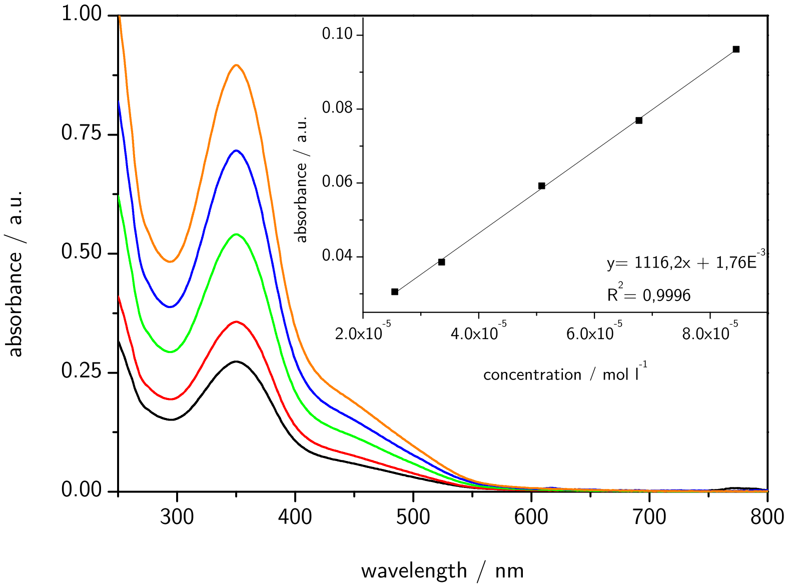

Figure 5.10: UV/Vis spectra and corresponding calibration curve at $\lambda = 500\,\mathrm{nm}$ of a concentration series of HABA-propionate in PBS buffer.

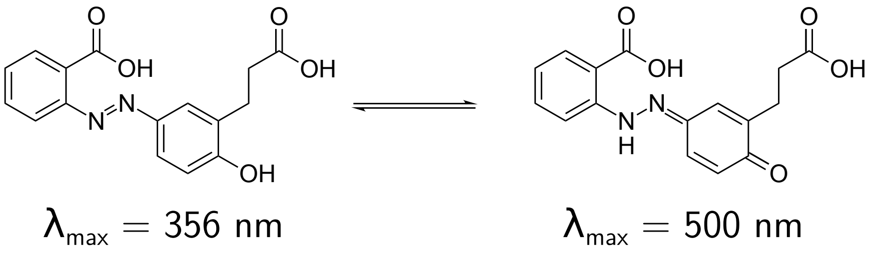

Figure 5.11: Structure, tautomerism and corresponding emission maxima of 3'-(carboxyethyl)-4'-hydroxyazobenzene-2-carboxylic acid (HABA-propionate).

spectroscopy is not as straight forward as for solutions. As the volume of the hydrogel is not known since it is difficult to determine, the amount of dye cannot be expressed in $\mathrm{mol\,L^{-1}}$.

Nevertheless, if the weight of the HG sample is known, it is possible to express the amount of coupled HABA-propionate per (milli)gram of hydrogel. First, the extinction coefficient of HABA-propionate was determined out of the concentration series in phosphate buffered saline (PBS) buffer (cf. **figure 5.10**). The extinction coefficient was determined at 500 nm, the peak of the keto form of HABA-propionate (cf. **figure 5.11**).

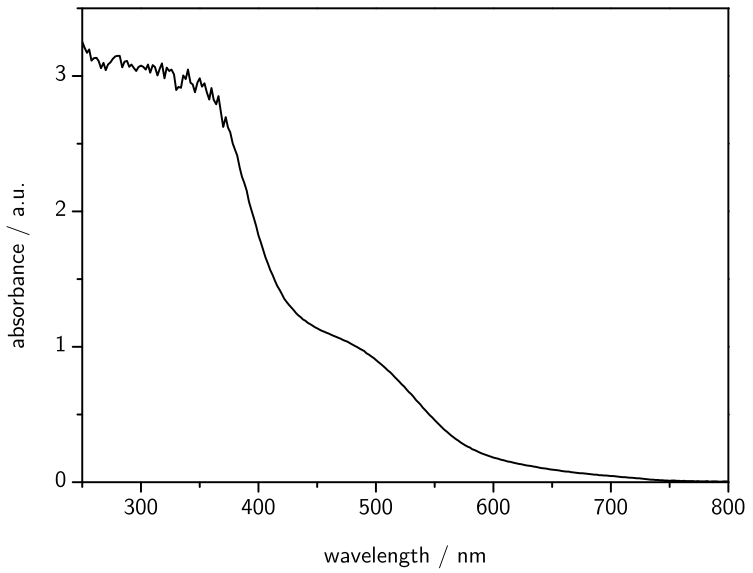

Figure 5.12: V/Vis spectrum of **IHO-1** functionalised with HABA-propionate.

When evaluating the UV/Vis absorption of the HABA-functionalised **HG-3** (**HG-3H**) in **figure 5.12**, starting from Beer-Lambert law, the amount of coupled HABA-propionate can be expressed by the following calculation:

From Beer-Lambert law,

$$E = \varepsilon\, c\, d \qquad ; \qquad c = \frac{E}{\varepsilon\, d} \tag{5.5}$$

with E the extinction, ε the absorption coefficient, the concentration c and the length of the cell d. The concentration of the dye in the cell is obtained in $\mathrm{mol\,L^{-1}}$ in the standard way of calculation by inserting the parameters. For the cell length d, the thickness of the film (125 µm) was taken, because the dye is only present in the hydrogel and not distributed over the whole cell.

As the dry weight of the sample was determined before the reaction, the concentration can be converted to molality b (in $\mathrm{mol\,kg^{-1}}$) by taking the density of poly(hydroxyethyl methacrylate) (PHEMA) as an approximation for the hydrogel's density. The molality is then multiplied by the dry weight of the HG sample to give the relative amount of HABA-propionate per HG sample. In total, the equation for the calculation of the relative amount of coupled HABA-propionate per gram of hydrogel can given as

$$b_{HABA-propionate} = \frac{E}{\varepsilon_{500nm}\, d_{HG-film}\, \rho_{HG-film}} \tag{5.6}$$

All data used in the calculations and the results thereof, are summarised in **table 5.3**.

Table 5.3: Summary of UV/Vis data, calculated concentrations and amount of 3'-(carboxyethyl)-4'-hydroxyazobenzene-2-carboxylic acid (HABA-propionate) coupled to a p(HEMA-stat-OEGMA$_{300}$-stat-OEGDMA$_{400}$) IHO (**IHO-1**).

ε_{500nm} / L mol^{-1} cm^{-1}	1110 ± 13
E_{500nm} / a.u.	0.9035
ρ_{HG}[a]/ g cm^{-3}	1.15
d_{HG} / 10^{-6} m	125.0
$b_{HABA-propionate}$[b] / 10^{-3} mol g^{-1}	5.48
b_{HEMA}[c] / 10^{-3} mol g^{-1}	4.11
F / %	130.0

[a] Density of PHEMA as approximation.
[b] Amount of HABA-propionate per g of hydrogel.
[c] Theoretical amount of HEMA in the hydrogel, calculated from monomer feed.

When comparing the amount of HEMA in the copolymer with the detected amount of HABA-propionate (cf. **table 5.3**), it appears that more HABA-propionate is coupled than HEMA was available for coupling. In terms of numbers, a degree of functionalisation (F) of 130 % would have been achieved for this Steglich-esterification. There are at least two hypotheses for this discrepancy: 1. additional HABA-propionate is physically adsorbed in the hydrogel or 2. the actual proportion of HEMA in the copolymer is higher than the theoretically calculated amount.

Although the functionalised **IHO-1** films were intensively washed with organic and aqueous solutions, there is always the possibility that a number of dye molecules are trapped inside the hydrogel, although they are not covalently bound to the polymer network. However, there are no positively charged moieties present in the polymer, which would facilitate a physical adsorption of HEMA-propionate *via* electrostatic interactions. Therefore, an additionally adsorbed amount of 30 % of HABA-propionate is rather unlikely.

Another possible explanation for the pronounced discrepancy of b_{HEMA} and $b_{HABA-prop.}$ is the hypothesis, that HEMA and OEGMA$_{300}$ do not copolymerise ideally and therefore $\chi_{HEMA,feed} < \chi_{HEMA,final}$. This hypothesis is supported e.g. by the findings of Zhu *et al.*, who copolymerised HEMA and OEGMA *via* surface induced polymerisation.[164] Their results indicated a difference of $\chi_{HEMA,feed}$ and $\chi_{HEMA,final}$ of 10 % to 40 %, depending on the total proportion of HEMA in the feed. Corresponding reactivity ratios were calculated as $r_{HEMA} = 2.47 \pm 0.27 > 1 > r_{OEGMA} = 0.83 \pm 0.10$ (for further details consult the reference). So if HEMA is predominantly incorporated in the copolymer network, then the values for b_{HEMA} and the resulting degree of functionalisation are incorrect. Though, a pronounced difference in monomer incorporation is only possible, if incomplete conversion is achieved in the UV polymerisations.

Regardless of these problems in determining the exact amount of coupled HABA-propionate, this first functionalisation reaction indicated hydroxyl groups in the hydrogel are accessible and reactive. Further, a functionalisation with biotin instead of a dye molecule was targeted and performed. The results thereof are shown in the next section.

5.4.2 Coupling of biotin

As a proof-of-concept system for the detection of bio-molecules with thermoresponsive IHOs, the binding pair of biotin and avidin was selected. The hydrophobic biotin molecules are to be incorporated into the hydrogel as a recognition unit, while the hydrophilic avidin serves as analyte molecule. This particular binding pair was selected because binding of avidin to the hydrogel-coupled biotin moieties changes the overall hydrophilicity of the hydrogel and thus its phase transition behaviour, inducing a shift in Bragg diffraction wavelength. This shift is analogous to the temperature induced shift shown in **section 5.3.1**, with the important difference, that in the IHO the shift is induced under isothermal conditions.

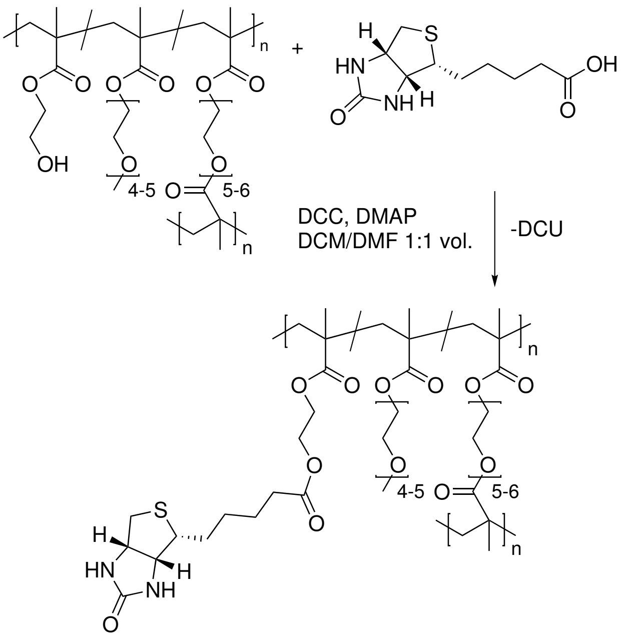

Figure 5.13: Scheme of the biotinylation of IHOs; exemplarily shown for **IHO-1**.

For several reasons, biotin/avidin is a vastly applied binding pair in biochemistry.[8] First of all, the binding between biotin and avidin is very selective, due to design of the binding pockets. With this very specific binding pair, it is possible to evaluate the specific binding of an analyte molecule (avidin) to a targeting group (biotin), which is immobilised in the hydrogel network.

A second reason, why biotin/avidin is frequently used, is the strong affinity between biotin and avidin, with an affinity constant of $K_a = 10^{15}\,\mathrm{mol\,L^{-1}}$.[165] In fact, the bond between biotin and avidin is the strongest non-covalent biological bond known. A binding pair with an affinity of this magnitude is an advantage and disadvantage at the same time. On the one hand, the high affinity ensures, that both binding partners will bind to each other nearly irreversibly without dissociation, increasing the sensitivity of the sensor. So for a proof-of-concept reaction, the chances that a successful coupling and therefore also a measurable event occurs are rather high. On the other hand, binding pair affinities, which occur in most biological systems, are several orders of magnitude lower[166], which makes the biotin/avidin system only remotely comparable. Nevertheless, biotin/avidin seemed to be a suitable tool for a first approximation of an analyte molecule binding selectively to a targeting group.

---

[8] The Web of Knowledge (Thomson Reuters) lists over 30.000 hits for the topic search term "biotin *avidin", which also includes streptavidin.

Biotin was coupled to the IHO *via* Steglich esterification, applying the previously established conditions for coupling of HABA-propionate, with marginal differences. E.g. the mixture of biotin and DMF had to be heated first to over 60 °C, to dissolve biotin properly. Subsequently, the solution was cooled down before the other reactants were added.

When comparing the coupling of biotin with the coupling of HABA-propionate, it is evident that coupling of a dye gives a much quicker and easier feedback, whether the reaction was successful. This is especially the case when cross-linked materials are used, because the analysis with standard analytical tools like NMR or infrared spectroscopy (IR) is more difficult compared to the work in solution, especially when only low amounts of biotin are coupled.

After thorough washing cycles, most of the films displayed an opaque appearance in water at room temperature, while their unfunctionalised precursors were perfectly transparent. This could be interpreted as a shift of the CP of the hydrogel, after the hydrophobic biotin was coupled. The reduced swelling of biotinylated hydrogel films supports this hypothesis (details in **section 5.4.2.3**).

5.4.2.1 Infrared analysis of biotinlyated hydrogel films

Qualitative spectroscopic analysis of dried biotinylated films was performed *via* IR. In **figure 5.14**, infrared spectra of biotinylated and unfunctionalised HEMA-rich **IHO-1** are overlayed for comparison. For better comparability, the spectra were normalised relative to their minimum (band at 1730 $\mathrm{cm^{-1}}$), which is considered to arise from the ester of the methacrylates. This peak should not change after biotin coupling.

The most important bands to verify whether biotin was bound to the hydrogel are highlighted in **figure 5.14**. Additionally to the ester-band of the methacrylate polymer at 1730 $\mathrm{cm^{-1}}$, a band at 1700 $\mathrm{cm^{-1}}$ appears in the spectrum of **bIHO-1**. This new band is attributed to the urea of biotin and the ester, which was newly formed in the Steglich esterification between biotin and HEMA.

The other band, which is attributed to biotin and is not superimposed by the polymer, is the υC−S band around 685 $\mathrm{cm^{-1}}$. This band is difficult to detect, because

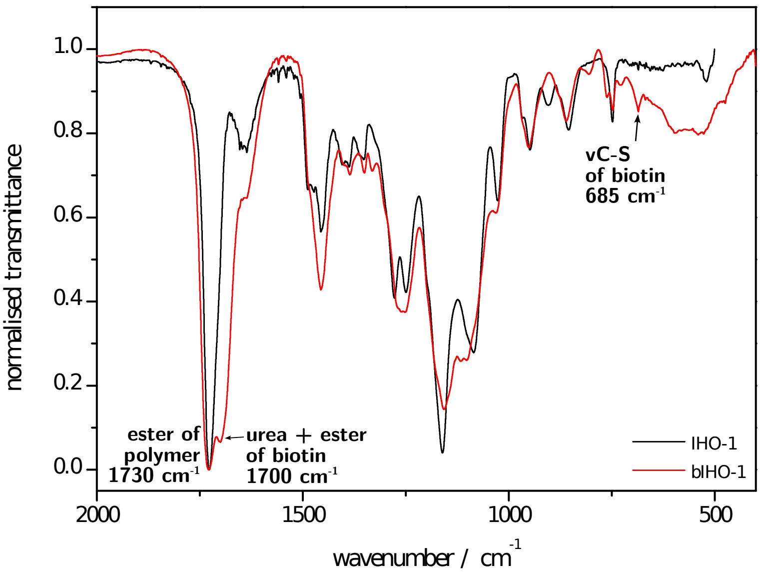

Figure 5.14: Overlay of a selected region of the normalised infrared spectra of **IHO-1** (black) and **bIHO-1** (red).

sulphur-related bands are normally rather weak in IR spectroscopy. Both urea and υC−S bands occur at the same wavelength for pure biotin.

In summary, IR bands of biotin can not be easily separated from those of the hydrogel. Therefore, a quantitative determination of the amount of coupled biotin could not be accomplished *via* IR spectroscopy. Nevertheless, a qualitative evidence for the presence of coupled biotin in the IHO could be made. The quantitative evaluation of accessible biotin was accomplished with the HABA/avidin assay, which is described in the next section.

5.4.2.2 Quantification of accessible biotin *via* HABA/avidin assay

The HABA/avidin displacement assay for the detection of coupled biotin works in the following way: avidin is incubated in an aqueous solution of a dye molecule, the previously mentioned HABA. Similar to biotin, HABA molecules also bind to the four binding pockets of avidin, but with a much lower affinity of $K_a = 10^6\,\mathrm{mol\,L^{-1}}$.[167] Due to the tautomerism of HABA (cf. figure 5.11), avidin-bound HABA in the keto-form has a maximum absorption at 500 nm, while free HABA in its enol-form has a maximum at 350 nm. When the HABA-loaded avidin is exposed to a biotinylated sample, HABA is displaced by biotin and is released to solution. The tautomeric rearrangement, which occurs when HABA is released, decreases the absorption intensity at 500 nm. This decrease can be quantified with a UV/Vis spectrometer and the amount of coupled biotin can be calculated.

Table 5.4: Accessible amount of biotin per gram of hydrogel for HEMA-rich and -poor inverse hydrogel opals, determined *via* biotin/avidin assay.

sample	$b_{HEMA}{}^{a}$/ 10^{-4} mol g^{-1}	$b_{biotin}{}^{b}$ / 10^{-7} mol g^{-1}	F / %
bIHO-1	41.1	5.55	0.013
bIHO-2	2.39	2.29	0.096

[a] Theoretical amount of HEMA in the hydrogel, calculated from monomer feed. See experimental part for details.
[b] Calculated from HABA/avidin assay. See appendix for details.

The accessible amount and calculated degree of functionalisation of coupled biotin in HEMA-rich and -poor IHOs is presented in **table 5.4**. The quantities of HEMA and biotin are given as molality, with the unit mol g^{-1}. The molality describes the molar amount of biotin or HEMA per gram of polymer, which is an applicable quantity when working with cross-linked systems.

The first observation is the big difference of b_{HEMA} and b_{biotin} for HEMA-rich biotinylated **bIHO-1**. The result is a degree of functionalisation F of only 0.013 %. Comparing the absolute amount of coupled biotin in HEMA-rich **bIHO-1** with HEMA-poor **bIHO-2**, the accessible amount of biotin in **bIHO-2** is approx. half as much compared to **bIHO-1**. This results in a difference of the degree of functionalisation of approx. one order of magnitude, due to the varying HEMA content in the hydrogels.

However, the HABA/avidin assay is only able to detect accessible biotin moieties in the hydrogel. If there is a high number of biotin molecules, not all of them are able to bind to avidin due to sterical hinderance. Thus, less biotin is detected than there is actually in the system. This problem could be potentially minimised by using a longer, more flexible spacer between the hydrogel network and biotin. A rather short anchor like HEMA might not show enough flexibility to adapt to more complex sterical demands. See **figure 5.15** for a schematic representation of biotinylated hydrogel network with bound avidin.

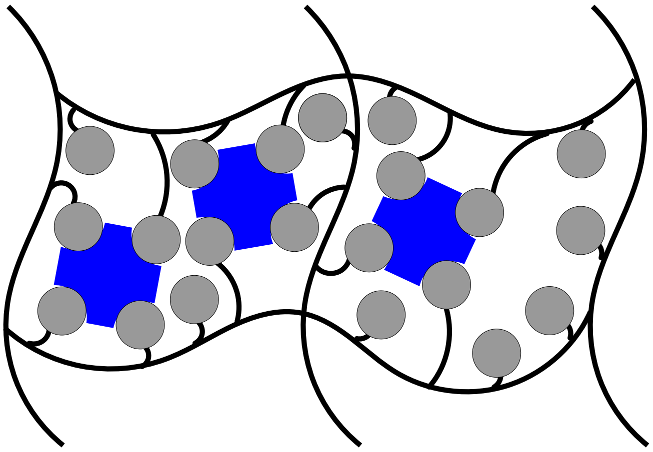

Figure 5.15: Schematic representation of a biotinylated (grey circles) hydrogel network, with bound avidin (blue squares with binding pockets) and excess of coupled biotin.

Another issue which might underestimate the amount of coupled biotin is hindered diffusion of avidin into the HG. If the HABA-loaded avidin molecules cannot diffuse into the HG to reach all biotin molecules, the amount of detected biotin does not reflect the true amount of coupled biotin. Regarding the calculated mesh sizes for the hydrogel networks (cf. **section 5.3.3**), it is possible that biotin molecules are able to diffuse into the dense part of the film, while avidin cannot do so due its much larger size. Although there might be coupled biotin in the dense part of the hydrogel, avidin would not be able to diffuse into the dense network and therefore also none of these biotin molecules would be detected.

Each of these possible factors, or a combination of all of them possibly leads to an underestimation of the amount of biotin, which is present in the hydrogel network. Alternatively, the results from HABA/avidin assay could also show the true picture and there is not as much biotin bound to the HG as expected. The results in the following sections indicate, that if only a small amount of biotin is coupled, it might still be enough to induce a measurable transition in the IHO.

5.4.2.3 Swelling properties of biotinylated inverse hydrogel opals

For evaluation of the thermoresponsive behaviour of the IHO after coupling of biotin, swelling ratios were determined for the biotinylated **bIHO-1** and compared to the non-functionalised **IHO-1** (**figure 5.16**). It is clearly visible, that **bIHO-1** shows

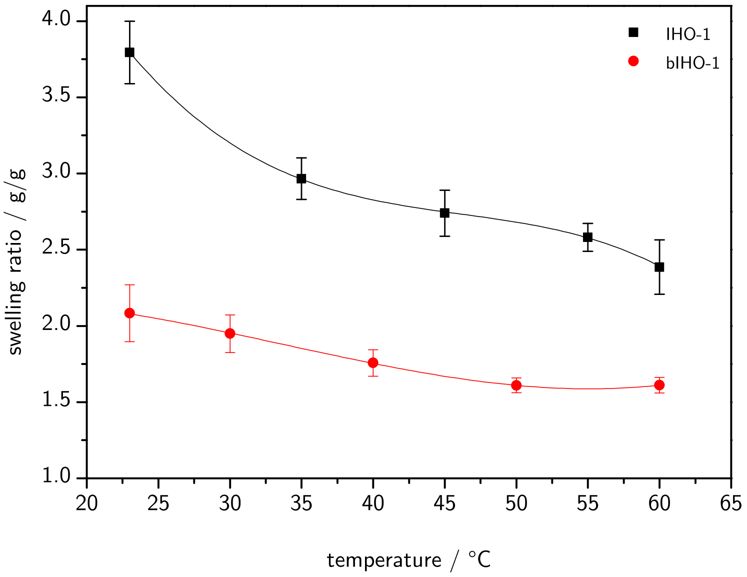

Figure 5.16: Comparison of swelling ratios of non-functionalised **IHO-1** (black squares) with biotinylated **bIHO-1** (red circles). Cubic fits were applied to guide the eye.

reduced swelling capacity at all temperatures due to the reduced hydrophilicity after coupling of the hydrophobic biotin molecules. Except for the less steep part in the beginning, both plots seem to follow a similar trend, as they reach a plateau-like state above 40 °C, where the swelling ratio did not change significantly when the temperature was elevated further. Although there seems to be only a relatively low amount of biotin coupled, this amount obviously has enough impact on the swelling characteristics of the hydrogel for a significant change in swelling ratio. Still, there might be a discrepancy in the amount of detected biotin in the HABA/avidin assay and the actually coupled biotin, which is not accessible for avidin.

5.4.2.4 Avidin response of biotinylated inverse hydrogel opals

The effect of coupled biotin on the optical properties of the IHOs was evaluated *via* UV/Vis transmission spectroscopy. First, the spectra of HEMA-poor **IHO-2** are depicted in **figure 5.17**. Comparing the non-functionalised **IHO-2** with the biotinylated **bIHO-2**, there is no significant difference in band gap wavelengths visible between the two samples. Probably, the absolute amount of coupled biotin was too low for a substantial change in phase behaviour of the hydrogel film, which was already indicated with the results of the HABA/avidin assay.

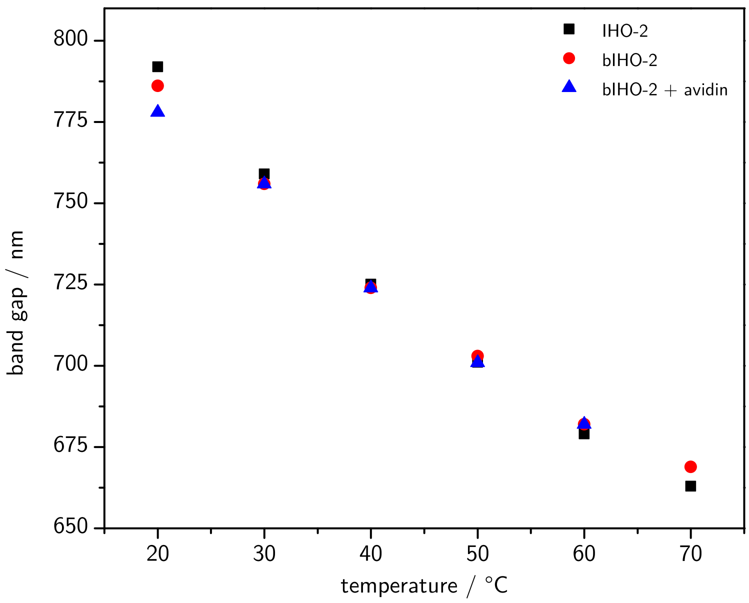

Figure 5.17: Plot of band gap wavelengths (λ_{max}) relative to temperature for **IHO-2** (black squares), **bIHO-2** (red circles) and **bIHO-2** with avidin (blue triangles).

For linear OEGMA copolymers, a pronounced shift of LCST of nearly 10 °C was determined for a copolymer with a biotin content of 3 mol-% by Buller *et al.*[138, 139, 142] As both **bIHO** contain much less biotin according to biotin/avidin assay, a similarly noticeable shift in band gap wavelength could not be expected. Nevertheless, the amount of biotin, which is coupled to **bIHO-1**, seems to be sufficient to induce a rather small but significant shift in Bragg peak wavelength, which is shown below.

For tests of the avidin response, films were equilibrated with an avidin solution (8.3 μmol L^{-1} in ultra-pure water) at least overnight and washed extensively, before measurements were made. Since there was already barely any effect after biotinylation of **IHO-2**, the same trend is observed for the avidin-response of **bIHO-2**. The exposure of avidin to the hydrogel does not seem to produce any effect, since there is no observable shift in band gap wavelength.

A slightly different picture is visible in plots of band gap wavelengths of HEMA-rich **IHO-1** and its biotinylated analogue **bIHO-1** in **figure 5.18**. Here, when comparing the non-functionalised **IHO-1** with the biotinylated **bIHO-1**, a difference in band gap wavelengths is visible. Apart from the results at 20 °C, band gaps of **bIHO-1** are always blue-shifted compared to **IHO-1**, with increasing magnitude at increasing

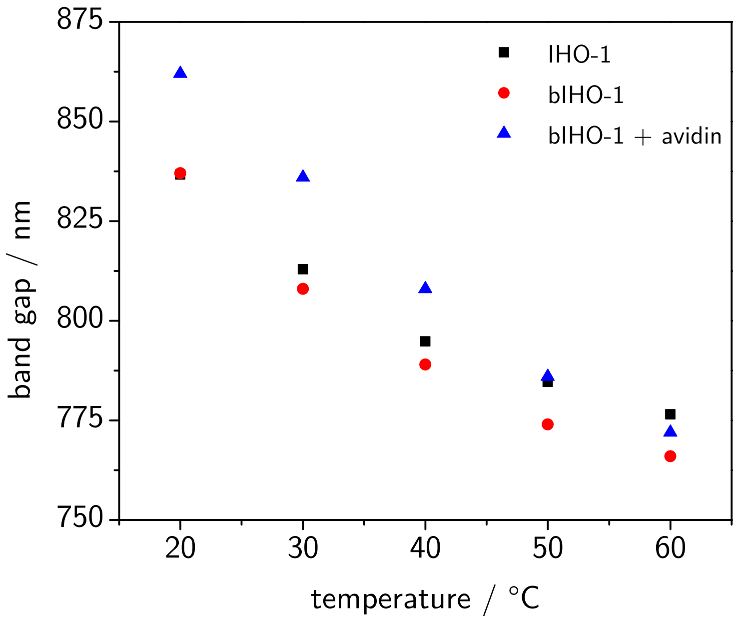

Figure 5.18: Plot of band gap wavelengths (λ_{max}) relative to temperature for **IHO-1** (black squares), **bIHO-1** (red circles) and **bIHO-1** with avidin (blue triangles).

temperature. This behaviour is explained with the increase in hydrophobicity with the introdution of biotin to the hydrogel network, resulting in a shrinking of the hydrogel matrix. Shrinking results in a decrease in distance between the regularly oriented cavities of the IHO, resulting in a blue-shift of the Bragg preak.

When avidin was added to **bIHO-1**, the opposite effect occurred. The hydrophilic protein induced a swelling of the hydrogel system and red-shifted the band gap by a maximum of 30 nm compared to **bIHO-1**. At temperatures up to 60 °C, **bIHO-1** with avidin always red-shifted compared to **bIHO-1** without avidin. The magnitude of the shift decreased with increasing temperature, possibly due to a pronounced shrinking at higher temperatures, which could not be compensated by the hydrophilic avidin.

This is remarkable, as the relative amount of biotin in the IHO with approximately 0.1 % is also not very high. Either this amount of biotin is already enough to cause a shift in this magnitude, or the the amount is underestimated by the HABA/avidin test, as discussed above.

To evaluate whether the red-shift after avidin addition is specific due to binding to biotin, which was coupled to the hydrogel backbone, a control experiment was

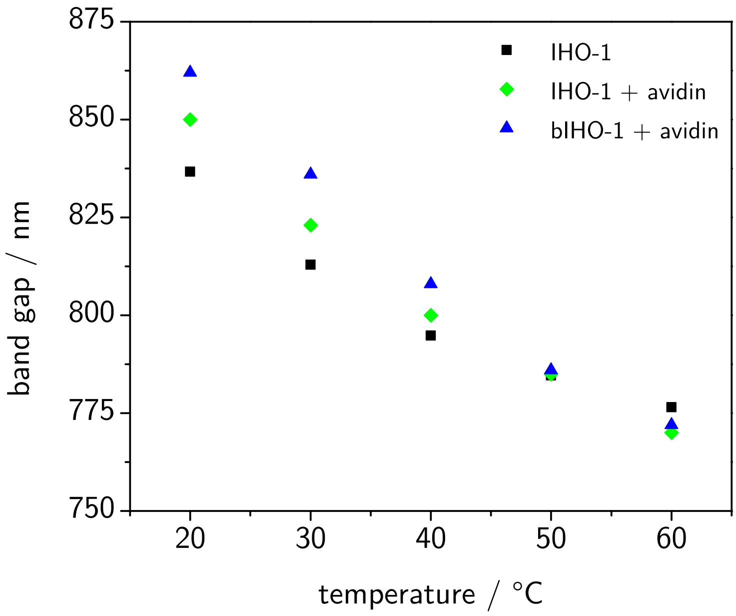

Figure 5.19: Plot of band gap wavelength (λ_{max}) relative to temperature for **IHO-1** (black squares), **IHO-1** with avidin (gree diamonds) and **bIHO-1** with avidin (blue triangles).

performed. The same avidin solution was added to non-functionalised **IHO-1** and the UV/Vis absorption was recorded. In **figure 5.19**, a plot of the UV/vis data of the control experiment is depicted.

When comparing the change of band gap wavelength at the various temperatures, the addition of avidin to the non-functionalised **IHO-1** also red-shifts the Bragg peaks. However, the magnitude of the shift is always lower compared to the response of **bIHO-1** to avidin. The response to avidin of **IHO-1** can be explained by the nature of the swelling/shrinking behaviour of the hydrogel. Probably, avidin is physically adsorbed in the hydrogel or hindered in diffusion and remains inside the network even after extensive washing procedures. The presence of avidin in the polymer system alters the swelling characteristics and red-shifts the band gap by a small magnitude.

Interestingly, exposing the HEMA-poor **IHO-2** and **bIHO-2** to avidin solution does not shift the band gap at all (cf. **figure 5.17**). The denser, more cross-linked architecture of **IHO-2** probably prevents diffusion of avidin inside of the dense hydrogel part. Maybe also HEMA plays a role in the adsorption of avidin in the hydrogel, since apart from cross-linking density, HEMA content is the other big difference

Table 5.5: Summary of band gap wavelengths at various temperatures for non-functionalised and biotinylated **IHO-1** with and without addition of avidin.

	λ / nm				
sample	20 °C	30 °C	40 °C	50 °C	60 °C
IHO-1	837	813	795	785	777
bIHO-1	837	808	789	774	766
bIHO-1 + avidin[a]	862	836	808	786	772
IHO-1 + avidin[a]	850	823	800	785	770

[a] Films were equilibrated in avidin solution (8.3 µmol L^{-1} in ultra-pure water) and washed extensively with ultra-pure water before analysis.

between **IHO-1** and **IHO-2**.

Nevertheless, with **IHO-1** it was possible to create an inverse hydrogel opal sensor based on bio-compatible OEGMA monomers, which is able to blue-shift its band gap wavelength when temperature is increased. When **IHO-1** is biotinylated, the thermoresponsive principle is extended towards protein responsiveness. Upon exposure of the biotinylated **bIHO-1** to avidin, the opal shows a red-shifts of its band gap wavelength due to specific binding of avidin to the recognition unit biotin. With the presented properties, this material can be used as a basis for upcoming development of biomolecule-responsive sensors.

6 Summary and conclusion

The overall aim of the work was the preparation of a hydrogel-based opal sensor material, which is able to detect the specific binding of a protein with a colour change of its opalescent reflection. This was realised by preparation of so-called inverse hydrogel opals (IHOs) in a two-step approach, where uniformly assembled particles (so-called colloidal crystals) were used as a template for the built-up of stimuli-responsive hydrogel matrices. The hydrogels were chosen from the group of oligo(ethylene glycol)methacrylates (OEGMAs), which are known to be biocompatible. For the detection of biomolecules, targeting groups were to be coupled to the hydrogel and the effect of the specific binding of the corresponding analyte on the reflected colour was to be evaluated.

As a first step for preparation of the templates, a series of differently-sized monodisperse silica particles were synthesised according to the well-known "Stöber method" and characterised by DLS, AFM and SEM. Subsequently, silica particles with a mean diameter of 400 nm assembled into colloidal crystals onto glass substrates *via* the vertical deposition technique. By variation of the deposition parameters, colloidal crystals consisting of 14 particle layers, which corresponds to a total vertical spread of approx. 5 µm, were assembled. SEM micrographs confirmed uniform arrays of particles. UV/Vis transmission analysis showed an extinction peak around 780 nm, resulting from Bragg diffraction of the colloidal crystal. The opalescent reflections could be also seen with bare eyes. UV/Vis reflection spectroscopy confirmed a linear angular dependence of the Bragg peak, which is predicted by the theory.

The functional hydrogels were prepared in a self-built polymerisation mould, which consisted of two glass slides, where one of the slides was coated with the colloidal crystal template. A polymerisation solution consisting among others of oligo(ethylene glycol)methacrylate monomers and crosslinker, hydroxyethyl methacrylate (HEMA) as a functional monomer, was injected into the mould and filled all voids in-between the template particles. After UV-polymerisation at 365 nm, thin free-standing hydrogel films were obtained. The films did not show any colourful reflection, due to the lack of refractive index contrast between particles and matrix. To restore the refractive index contrast, the hydrogels were treated with aqueous HF, to etch the particles and to obtain inverse opals, with uniformly aligned pores inside of the hydrogel matrix. These IHOs distinctly swelled in water below the critical temperature.

The regular array of pores with a mean diameter of 400 nm was confirmed by SEM, which was in the same range as the template particles. Additionally, connection points between the pores were visible in the SEM micrographs, which should facilitate diffusion of large molecules through the porous network. The reflected colour of the IHOs was analysed in respect to temperature. When temperature was increased, the IHOs displayed a blue-shift up to 65 nm of the Bragg peak wavelength, as water was released from the thermoresponsive hydrogel, resulting in a shrinking of the pores. The magnitude of the shift was depending on the composition of the hydrogels, and therefore their swelling characteristics in water.

For the sensing of biomolecules, a test system consisting of the hydrophilic protein avidin and its binding partner biotin was applied. Biotin was covalently coupled to the hydroxyl group of HEMA in the hydrogel. Despite low amount of accessible biotin, a red-shift of the Bragg peak wavelength of about 30 nm was accomplished, when avidin was introduced to the biotinylated IHOs at room temperature. The effect is based on the binding of the hydrophilic biotin to the hydrogel network, which affects the hydrophilicity of the whole system and induces a swelling of the hydrogel. Control experiments with non-biotinylated IHOs only displayed a very small shift of the Bragg peak.

In summary, hydrogel-based inverse opal sensor materials were prepared from biocompatible and thermoresponsive OEGMA monomers *via* a two-step process applying deposited silica colloidal crystals as templates. Biotin was incorporated as a targeting group for the protein avidin. Temperature and biomolecule response of the material was successfully evaluated by analysis of the Bragg peak shift *via* UV/Vis transmission spectroscopy. The combination of a hydrophilic, biocompatible matrix with a porous, interconnected inner structure ensures proper diffusion of hydrophilic biomolecules, also of larger size. The thermoresponsive nature of the hydrogel is considered to amplify the swelling or shrinking of the IHOs, so that small changes in hydrophilicity of the system lead to large effects on the swelling characteristics.

7 Experimental part

7.1 Chemicals

chemical	formula	CAS	purity	supplier
ammonia	NH_3	7664-41-7	28 % to 30 %	Acros
avidin	-	-	95 %+	BNLfood
4,4'-azobis(4-cyanovaleric acid) (V-501)	$C_{12}H_{16}N_4O_4$	2638-94-0	-	Wako
azobisisobutyronitrile (AIBN)	$C_8H_{12}N_4$	78-67-1	98 %	Aldrich
D-biotin	$C_{10}H_{16}N_2O_3S$	58-85-5	99 %	Iris Biotech
dichloromethane	CH_2Cl_2	75-09-2	-	J.T. Baker
N,N'-dicyclohexylcarbodiimide	$C_{13}H_{22}N_2$	538-75-0	99 %	Alfa Aesar
diethyl ether	$C_4H_{10}O$	60-29-7	99.5 %	Th. Geyer
di(ethylene glycol)methylether methacrylate	$C_9H_{16}O_4$	45103-58-0	99.5 %	Aldrich
N,N'-dimethylformamide	C_3H_7NO	68-12-2	99.9 %	Merck
ethanol	C_2H_6O	64-17-5	99.5 %	ChemSolute
hydrofluoric acid	HF	7664-39-3	10 %	ChemSolute
hydrogen peroxide	H_2O_2	7722-84-1	30 %	Acros
4-hydroxy azobenzene-2-carboxylic acid (HABA)	$C_{13}H_{10}N_2O_3$	1634-82-8	98 %	ABCR
2-hydroxyethyl methacrylate	$C_6H_{10}O_3$	868-77-9	96 %	Acros

chemical	formula	CAS	purity	supplier
Irgacure 2010	-	-	-	Ciba
oligo(ethylene glycol) dimethacrylate 400/550 g mol^{-1}	-	25852-47-5	-	Aldrich
oligo(ethylene glycol)methylether methacrylate 300/475 g mol^{-1}	-	26915-72-0	-	Aldrich
sodium hydroxide	NaOH	1310-73-2	-	ChemSolute
sulphuric acid	H_2SO_4	7664-93-9	98 %	ChemSolute
tetraethyl orthosilicate	$SiC_8H_{20}O_4$	78-10-4	99 %	Merck

7.2 Methods

UV/Vis spectroscopy Spectra were recorded on a Cary 50 UV/Vis spectrophotometer (Agilent, Germany) equipped with a xenon lamp and a thermoelectric Peltier element to control the temperature of the sample cell. All hydrogel films and inverse opals were analysed within a quartz window with a gap of 0.5 µm, filled with distilled water. Spectra of dry silica opals were recorded on a float glass slide, bearing the opal, placed orthogonally to the laser beam into the apparatus. Measurements were performed with a scan rate of 600 nm min^{-1}.

Dynamic light scattering Size determination of silica particles was performed with a High Performance Particle Sizer (HPPS, Malvern Instruments, UK) equipped with a thermoelectric Peltier element for temperature control, a He-Ne laser (λ = 633 nm) operated in backscattering mode at a scattering angle of θ = 173°. Samples were diluted with either ultra-pure H_2O or anhydrous EtOH to a concentration of approx. 2 g L^{-1}, filtered with a syringe filter with a mesh size of at least twice the particle diameter (mostly Acrodisk glass fiber 1 µm from Pall, Europe) and transferred to a disposable PS cuvette. When the presence of agglomerates had to be evaluated, only the solvent was filtered to remove dust particles. Measurements were performed at 20 °C with five individual runs; the data given over arithmetic averages of all runs. Size histograms were produced using Malverns ZetaSizer Software using 300 classes between 1 and 1000 nm, if there were no agglomerates visible above 1 µm.

Turbidimetry The cloud points of linear polymer solutions were determined at $2\,\mathrm{g\,L^{-1}}$ in ultra-pure water with a TP1 photometer (Tepper, Germany). The transmittance of the polymer solution was recorded as a function of temperature at a wavelength of 670 nm with heating and cooling cycles at rate of $1\,^{\circ}\mathrm{C\,min^{-1}}$. The optical path length was 1.2 cm. CP_{50} was determined as the temperature, where a transmittance of 50 % was measured.

Infrared spectroscopy IR-spectra were taken from KBr pellets using a Bruker IFS 66/s FT-IR spectrometer in synthetic air atmosphere.

Scanning electron microscopy [9]

A small amount of the sample was placed in a specimen holder and frozen to −196 °C by plunging into nitrogen at atmospheric pressure. Freeze-fracturing was carried out in a Gatan Alto 2500 cryo-preparation chamber at −150 °C. After fracturing the temperature of the sample was elevated to −98 °C for freeze-etching. The sample was etched for 45 s and subsequently the temperature of the sample was lowered to −130 °C for sputtering with platinum. The sample was transferred into a cryo high resolution-scanning electron microscope S-4800 from Hitachi. The SEM micrographs were obtained at a stage temperature of −145 °C and −100 °C at an accelerating voltage of 2 kV.

Atomic force microscopy [10]

Micrographs were recorded with an AFM unit by NT-MDT (Russia), type “Smena”, operated with a “Solver Pro-M Controller”. Probes were NSG10 silicon probes with a tip diameter of approx. 10 nm, operated at a resonance frequency of 230 kHz. Samples were treated in “semi contact mode”, which ensured a minimal lateral force between tip and surface.

Size exclusion chromatography [11]

---

[9] Measurements were performed by Dr. B. Tiersch, Uni Potsdam.

[10] Measurements were performed by B. Stiller, Uni Potsdam.

[11] Measurements were performed by Dr. C. Wieland and S. Stegmann, Fraunhofer IAP.

The setup of size exclusion chromatography measurements in DMF consisted of a single channel devolatiliser unit (WEG Dr. Bures, Germany), an isocratic pump P 1000 (Spectra Physics, USA), a set of PolarGel columns (Guard 7.5 × 75 mm and PolarGel L 7.5 × 300 mm; both from Polymer Laboratory, USA), a UV/Vis detector SEC-3010 and a refractometer SEC-3010 (both from WEG Dr. Bures, USA). Measurements were performed at 50 °C with a flow rate of 1 mL min^{-1}. For calibration, linear polystyrene standards (Polymer Standards Service, Germany) were applied.

NMR spectroscopy [12] ^{1}H (300 MHz) NMR spectra were taken on a Avance 300 spectrometer (Bruker, USA), equipped with an autosampler unit. If there was no TMS added to the solvent, then the solvent peak was chosen as point of reference.

UV-induced polymerisations UV-curing reactions were conducted in a UVA-Cube 100 (Hoenle, Germany) curing chamber at 100 W, equipped with a Fe-doped mercury vapour lamp and a soda-lime glass filter. Maximum emission was at 365 nm, while the filter extinguished all rays below 300 nm. Distance between lamp and sample was approx. 20 cm.

Ultrasonic treatment For cleaning of glass slides and dispersion of silica particles, an ultrasound device RK 100H from Bandelin Sonorex (Berlin, Germany) with a high-frequency output of 160 W with a frequency of 35 kHz.

Glass slides All glass-slides used in this work were standard soda-lime float glass slides by Carl Roth (Karlsruhe, Germany), with a size of 76 mm × 26 mm. Before use, they were cleaned according to this protocol:

- ultrasonic bath: 15 min in acetone
- rinsing with distilled water
- ultrasonic bath: 15 min in an aqueous detergent solution of Hellmanex II (Hellma, Müllheim; $w = 0.02$)

---

[12] Measurements were performed by A. Krtitschka, Group of Prof. Kleinpeter, University of Potsdam.

- rinsing with ultra-pure water
- ultrasonic bath: 15 min in ultra-pure water

When a hydrophilic glass surface was aspired, the clean slides were additionally treated with piranha acid (H_2SO_4/H_2O_2 v/v 1:1) to etch the SiO_2-groups on the glass surface.

HABA/avidin assay Determination of the amount of accessible biotin was conducted after a protocol from Thermo Scientific (USA) on basis of literature from Green *et al.*[167] For the HABA solution, 24.2 mg of HABA was dissolved in 9.9 mL of ultra-pure water and 0.1 mL of 1 M NaOH was added. 600 µL of the HABA solution were mixed with 10 mg of avidin and filled with 19.4 mL PBS. From this stock solution, 1 mL was taken and the UV/Vis absorption at 500 nm was recorded. Subsequently, a sample of a dry biotinylated hydrogel film was added and the whole mixture was placed in a fridge for equilibration. Afterwards, the absorption of the solution was recorded. The amount of accessible biotin was calculated from the difference in absorption before and after addition of the hydrogel:

$$\Delta A_{500} = 0.9\, A_{500,HA} - A_{500,HAB} \tag{7.1}$$

$$c_{biotin} = \frac{\Delta A_{500}}{\varepsilon_{500}} \tag{7.2}$$

$A_{500,HA}$: absorption of HABA/avidin solution at 500 nm.

$A_{500,HAB}$: absorption of HABA/avidin solution after addition of a biotinylated sample at 500 nm.

ΔA_{500} : difference of $A_{500,HA} - A_{500,HAB}$.

ε_{500} : the molar absorption coefficient of the HABA/avidin complex at 500 nm ($3.4 \times 10^4\,\mathrm{L\,mol^{-1}\,cm^{-1}}$).

7.3 Calculations

Calculation of $\overline{N}_{EG}$

$$\overline{N}_{EG} = \frac{N_{EG,MonomerA} * \chi_{EG,MonomerA} + N_{EG,MonomerB} * \chi_{EG,MonomerB+...}}{\chi_{EG,MonomerA} + \chi_{EG,MonomerB} + \cdots} \tag{7.3}$$

with $N_{EG,MonomerX}$ the number of EG units in the side chain of the respective monomer X.

Calculation of the theoretical amount of HEMA in a hydrogel

$$b_{HEMA} = \frac{n_{HEMA}}{\sum m_{monomers}} \tag{7.4}$$

All numbers are related to the monomer feed and are taken directly from the recipe.

Calculation of the amount of accessible biotin coupled to a hydrogel

$$b_{biotin} = \frac{\Delta A_{500}}{m_{sample}\ \varepsilon_{500}} \tag{7.5}$$

ΔA_{500} : difference in absorption between the HABA/avidin complex and free HABA in HABA/avidin assay

ε_{500} : the molar absorption coefficient of the HABA/avidin complex at 500 nm ($3.4 \times 10^4\,\mathrm{l\,mol^{-1}\,cm^{-1}}$)

m_{sample} : dry mass of the biotinylated polymer sample.

7.4 Silica nanoparticles and colloid crystals

7.4.1 Silica nanoparticle synthesis

The synthesis of spherical nanoparticles was performed analogous to the literature procedure developed by Stöber *et al.*[65]

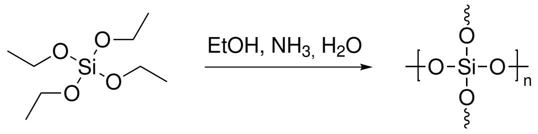

With the following formulation, spherical silica particles with a diameter of approx. 400 nm are obtained (formulations for particles of different diameters are presented in **table 2.2**):

5.0 g (24.0 mmol) of TEOS in 99.1 g absolute EtOH were added to a solution of 12.0 g ultra-pure H_2O and 53.4 g ammonium hydroxide (28 wt.-% NH_3 (877.9 mmol) at 30 °C over an interval of approx. 20 s. The solution was slowly stirred for at least 4 h. After a short time, arising turbidity in the solution indicated formation of particles. After completion, a sample was taken to determine the conversion by solid content measurements. Usually, a solid content of around 1.0 g L^{-1} was determined, indicating a conversion of 90 %.

For purification, the particles were separated from the solution *via* centrifugation at 4000 min^{-1}. To remove any residual impurities, the particles were cleaned by a cycle of re-dispersion in absolute EtOH *via* ultrasonic treatment, and subsequent centrifugation for multiple times. For better storage, the suspensions were concentrated to a solid content between 10 and 15 %.

The obtained suspensions were characterised by solid content and DLS. DLS data are shown in **table 2.3** and **figure 2.6**.

7.4.2 Colloidal crystal assembly via vertical deposition

The concentration of Stöber silica suspensions was adjusted to the desired level (usually $0.01 < w < 0.02$) with the appropriate solvent(s) (pure EtOH or EtOH/H_2O

mixtures). The obtained suspension was then treated with ultrasonics for approx. 15 min to properly disperse the particles in the suspension medium. Glass slides were cleaned and hydrophilised according to the protocol described in **section 7.2** above. 50 mL poly(propylene) (PP) bottles were decapitated to yield beaker-like vessels. The plastic vessels were cleaned with aqueous HF solution ((“weight”)/mass fraction (*w*) = 0.02) to remove potential silica contaminants. The silica suspension was filtered through a 1.0 µm syringe filter (Glass Acro Disk, Pall) into the PP beaker, which was placed in a drying oven. A clean glass slide was carefully placed vertically into the suspension. The oven temperature was set at 30 to 50 °C with fresh air supply. The dispersion medium was evaporated during to several days, depending on temperature and used solvent(s). After complete evaporation, the colloid crystal coated glass slide was rinsed carefully with EtOH to remove excess silica. The slides were dried with a heat gun in air at approx. 100 °C.

Formulations for selected deposition experiments are given in **table 3.1**. UV/Vis transmission analysis is shown in **figure 3.11** and reflection spectra in **figure 3.12**.

7.5 Synthesis of polymers

7.5.1 Synthesis of linear polymers

Synthesis of binary copolymers poly(hydroxyethyl methacrylate-stat-oligo(ethylene glycol)methylether methacrylate$_{300}$) (LCP-1 to -4)

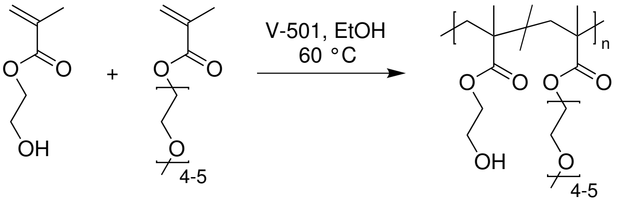

Linear polymers were synthesised *via* free radical copolymerisation. Briefly, a round-bottom flask was charged with monomers (HEMA, OEGMA$_{300}$, OEGMA$_{475}$ or MEO$_2$MA), initiator 4,4’-azobis(4-cyanovaleric acid) (V-501) and EtOH (v/v 4:1 solvent/monomers) as solvent (detailed formulations are shown in **table 4.1**). The mixture was degassed for 30 min by purging N_2 through the solution. After proper degassing, the mixture was heated to 60 °C and stirred over night. After the reaction was complete, the reaction was stopped by introducing air into the system. For work-up, the solution was precipitated into an excess of diethyl ether three times. The supernatant was decanted and the obtained polymer was dried *in vacuo*. Conversion was determined gravimetrically. The polymer was analysed *via* NMR spectroscopy, SEC and turbidity measurement

Turbidity spectra are shown in **figure 4.8**.

^{1}H NMR (300 MHz, **$CDCl_3$**) **δ (ppm):** 0.85 - 1.05 (**CH_3** backbone), 1.75 - 2.20 (**CH_2** backbone), 3.39 ($RCH_2O\mathbf{CH_3}$), 3.55 - 3.68 ($R\mathbf{CH_2}O\mathbf{CH_2CH_2}OCH_3$), 3.79 ($COOCH_2\mathbf{CH_2}OH$), 4.09 ($COO\mathbf{CH_2}CH_2OR$)

Table 7.1: SEC data of the synthesised linear copolymers **LCP-1** to **-4**.

sample	M_n / g mol^{-1}	M_w / g mol^{-1}	PDI
LCP-1	97000	250000	2.9
LCP-2	104000	235000	2.3
LCP-3	35000	89000	2.6
LCP-4	28000	72000	2.5

Synthesis of ternary copolymers poly(hydroxyethyl methacrylate-stat-oligo(ethylene glycol)methylether methacrylate$_{475}$-stat-di(ethylene glycol)methylether methacrylate) copolymers (LCP-5 to -7)

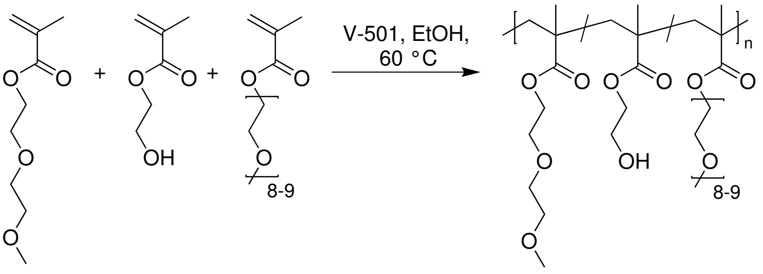

Synthesis, purification and analysis was performed analogous to the previously described synthesis of **linear copolymer (LCP)-1** to **-4**, with a different monomer composition. Formulations are given in **table 4.1**.

Turbidity spectra are shown in **figure 4.8**.

^{1}H NMR (300 MHz, **$CDCl_3$**) δ **(ppm):** 0.85 - 1.05 (**CH_3** backbone), 1.75 - 2.20 (**CH_2** backbone), 3.39 ($RCH_2O\mathbf{CH_3}$), 3.55 - 3.68 ($R\mathbf{CH_2OCH_2CH_2}OCH_3$), 3.79 ($COOCH_2\mathbf{CH_2}OH$), 4.09 ($COO\mathbf{CH_2}CH_2OR$)

Table 7.2: SEC data of the synthesised linear copolymers **LCP-5** to **-7**.

sample	M_n / g mol^{-1}	M_w / g mol^{-1}	PDI
LCP-5	74000	420000	5.7
LCP-6	72000	251000	3.5
LCP-7	67000	211000	3.2

7.5.2 Synthesis of chemically crosslinked hydrogels

Synthesis of poly(hydroxyethyl methacrylate-stat-oligo(ethylene glycol)methylether methacrylate$_{300}$-stat-oligo(ethylene glycol)dimethacrylate$_{400}$) hydrogels (HG-1 to -6)

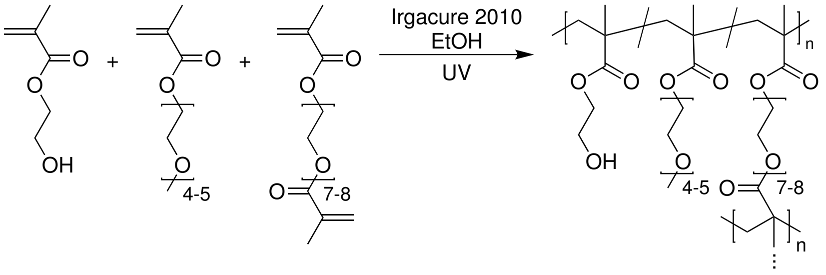

Chemically crosslinked hydrogels were prepared *via* UV-induced free radical polymerisation. A polymerisation mould consisting of two float glass slides, with parafilm as a spacer (final film thickness of 125 µm) were used. A solution of monomers (HEMA, $OEGMA_{300}$), crosslinker ($OEGDMA_{400}$), UV-initiator (Irgacure 2010) and water as solvent was prepared and subsequently injected into the mould with a pipette (for formulations consult **table 4.2**). Subsequently, the mould was introduced to a UV curing chamber UVA-Cube 100 (Hoenle, Germany) at 100 W and irradiated for 1 h while the mould was constantly cooled. After successful polymerisation, the mould was manually opened by first removing the parafilm followed by gentle lift-off of one of the glass slides. The film, which still adhered to the other glass slide, was placed into water to remove unreacted and leaching compounds.

Swelling ratios were determined gravimetrically and respective data is presented in **table 4.2** and **figure 4.13**. **FT-IR** (KBr, selected bands, wavenumber in cm^{-1}): 2945, 2885, 1727, 1635, 1480, 1456, 1160, 1086, 948. See appendix for full spectrum.

Synthesis of poly(hydroxyethyl methacrylate-stat-oligo(ethylene glycol)methylether methacrylate$_{475}$-stat-di(ethylene glycol)methylether methacrylate-stat-oligo(ethylene glycol)dimethacrylate$_{550}$) hydrogels (HG-7 to -10)

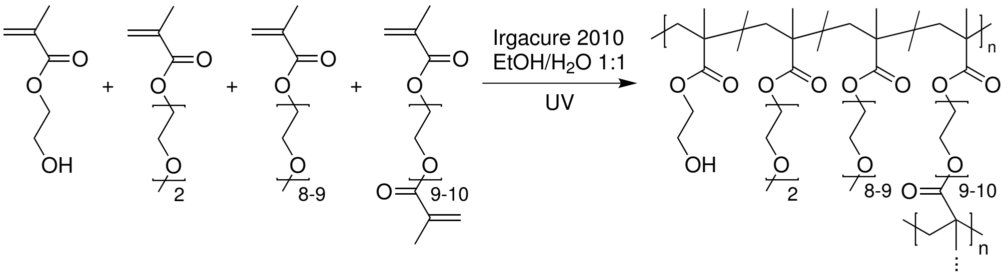

Synthesis and purification were performed analogous to **HG-1** to **-6**, with minor deviations concerning the polymerisation solution. The monomer feed consisted of MEO$_2$MA, HEMA, OEGMA$_{475}$ and OEGDMA$_{550}$, dissolved in water/EtOH 1:1 v/v. Except for this difference, the protocol of the previously described synthesis was followed.

For formulations and analytical data, consult **table 4.2**. **FT-IR** (KBr, selected bands, wavenumber in cm^{-1}): 2925, 2880, 1730, 1635, 1455, 1110, 948. See appendix for full spectrum.

7.5.3 Synthesis of inverse hydrogel opals (IHOs)

The synthesis of IHO was conducted in the same way as in section 7.5.2, with the difference, that one of the glass slides used in the mould was covered with a SiO_2 colloid crystal film of 5 µm thickness. Therefore, the reaction mixture filled the voids between the SiO_2 particles and a polymer network containing the particles was formed. After washing with water, the film was introduced into 2 wt.-% HF for the removal of the SiO_2 particles to yield a hollow honeycomb-like structure. As glass was etched by HF, the film glided away from the substrate into the liquid. When the particles were dissolved, a colourful opalescence in the free-standing film was visible. The IHO was washed with water and analysed *via* UV/Vis spectroscopy

Spectra are shown in **figure 5.5** and **5.6**.

7.5.4 Synthesis of HABA-functionalised hydrogels

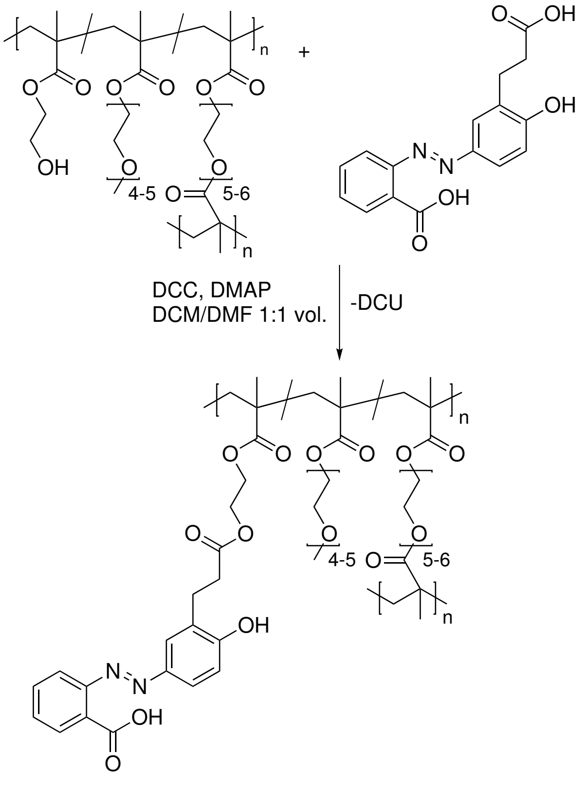

Polymer-analogous functionalisation of hydrogel films with a HABA derivative was achieved analogous to biotinylation under the same conditions. 3'-(Carboxyethyl)-4'-hydroxyazobenzene-2-carboxylic acid (synthesised by Dr. J. Buller, Fraunhofer IAP, after the procedure of Hofstetter *et al.*[163]) was dissolved in DMF while DCC and 4-dimethylaminopyridine (DMAP) were dissolved in DCM and added to the reaction mixture to start the esterification. The reaction was allowed to stand over night. The film obtained a strong dark-red colour, indicating high concentration of dye in the hydrogel film. Afterwards, the film was washed with DMF, water, 0.1 mol L^{-1} NaOH and finally PBS to equilibrate at a constant pH-value. The degree of functionalisation was determined *via* UV/Vis-spectroscopy with the film equilibrated in PBS solution.

UV/Vis: Concentration series and respective calibration curve are shown in **figure 5.10**. Analysis of the reacted hydrogel is presented in **figure 5.12** and results of HABA content calculations are given in **table 5.3**.

7.5.5 Biotinylation of IHOs

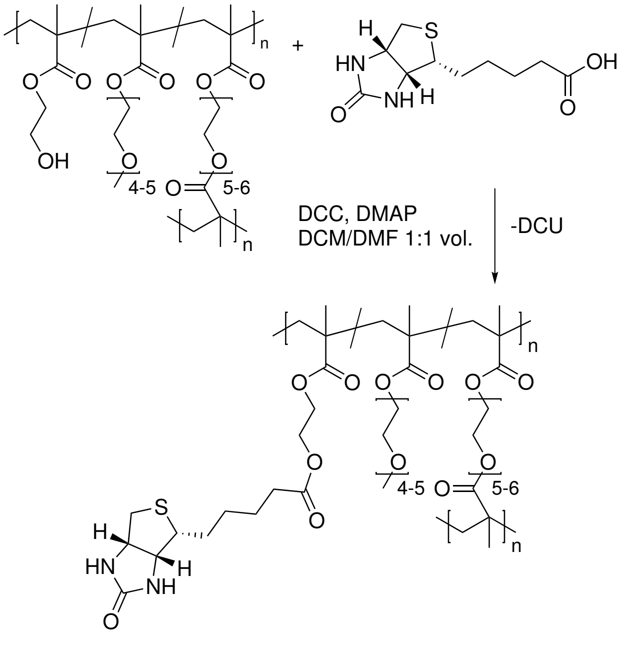

Biotinylation of hydroxyl group-containing polymers was done *via* Steglich-esterification with DCC as coupling agent. First, the dry weight of the polymer sample was determined. Afterwards, the hydrogel film was soaked with DMF and transferred to a reaction vial. Meanwhile, an excess of biotin (1 eq w/w of the film) was dissolved in anhydrous DMF at 60 °C and cooled down before it was added to the reaction vial.

DCC (1.2 eq rel. to biotin) and DMAP (0.1 eq rel. to biotin) were dissolved in anhydrous DCM and added to reaction vial to start the esterification. The mixture was gently agitated, so the hydrogel film was not ruptured. After successful conversion, the polymer film was washed thoroughly with DMF to remove dicyclohexylurea (DCU) and unreacted starting materials. Afterwards, the film was washed again with distilled water for the removal of DMF. The accessibility of biotin was evaluated with a HABA/avidin binding assay. The principle of this assay is described in **section 7.2**.

Results of the assay are shown in **table 5.4**, swelling ratios are shown in **figure 5.16** and UV/Vis data is presented in **figure 5.17**.

FT-IR (KBr disc, selected bands, wavenumber in cm^{-1}): 2930, 2873, 1727, 1699, 1635, 1456, 1157, 1105, 951, 685. See appendix for full spectrum.

Selbständigkeitserklärung

Ich erkläre, dass ich die vorliegende Arbeit selbständig und nur unter Verwendung der angegebenen Literatur und Hilfsmittel angefertigt habe.

Berlin, den 25. Oktober 2014 Martin Sütterlin

Appendix

Calculations

Calculation of $\overline{N}_{EG}$

$$\overline{N}_{EG} = \frac{N_{EG,MonomerA} * \chi_{EG,MonomerA} + N_{EG,MonomerB} * \chi_{EG,MonomerB+...}}{\chi_{EG,MonomerA} + \chi_{EG,MonomerB} + \cdots} \tag{6}$$

with $N_{EG,MonomerX}$ the number of EG units in the side chain of the respective monomer X.

Calculation of the theoretical amount of HEMA in a hydrogel

$$b_{HEMA} = \frac{n_{HEMA}}{\sum m_{monomers}} \tag{7}$$

All numbers are related to the monomer feed and are taken directly from the recipe.

Calculation of the amount of accessible biotin coupled to a hydrogel

$$b_{biotin} = \frac{\Delta A_{500}}{m_{sample}\ \varepsilon_{500}} \tag{8}$$

ΔA_{500} : difference in absorption between the HABA/avidin complex and free HABA in HABA/avidin assay

ε_{500} : the molar absorption coefficient of the HABA/avidin complex at 500 nm

$(3.4 \times 10^4\,\mathrm{l\,mol^{-1}\,cm^{-1}})$

m_{sample} : dry mass of the biotinylated polymer sample.

Infrared spectra

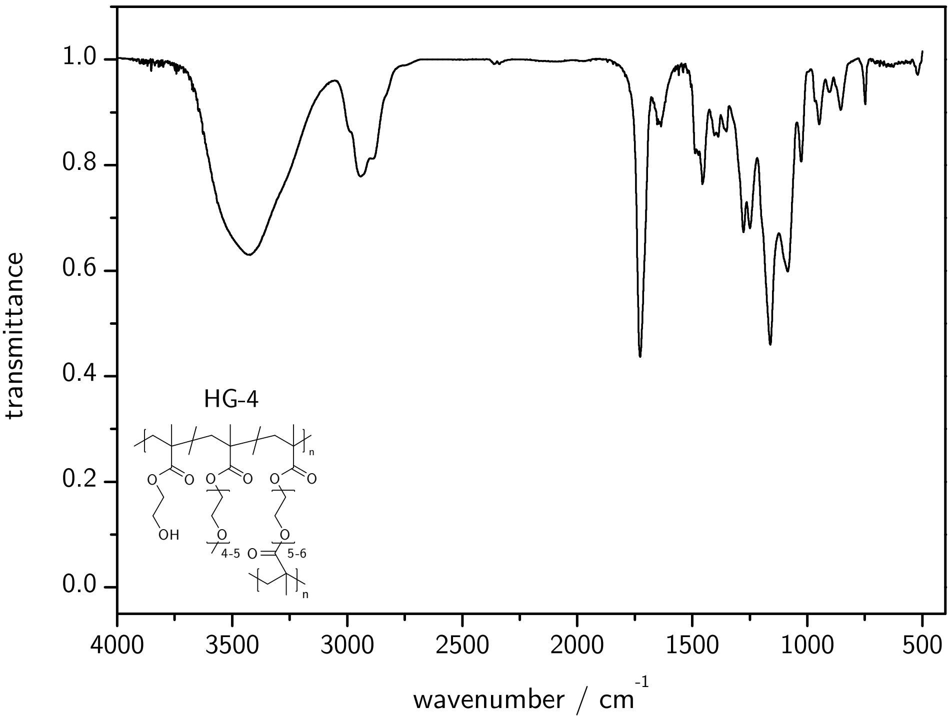

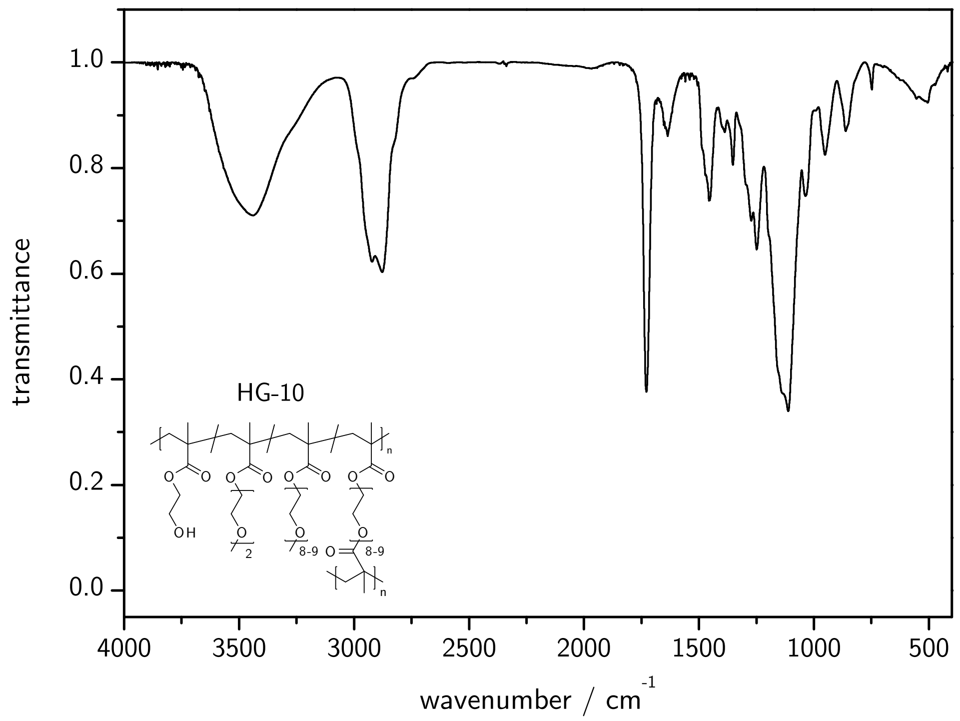

transmittance
1.0
0.8
0.6
0.4
0.2
0.0
4000
3500
3000
2500
2000
1500
1000
500
wavenumber / cm^{-1}
HG-10
OH
2
8-9
8-9
n

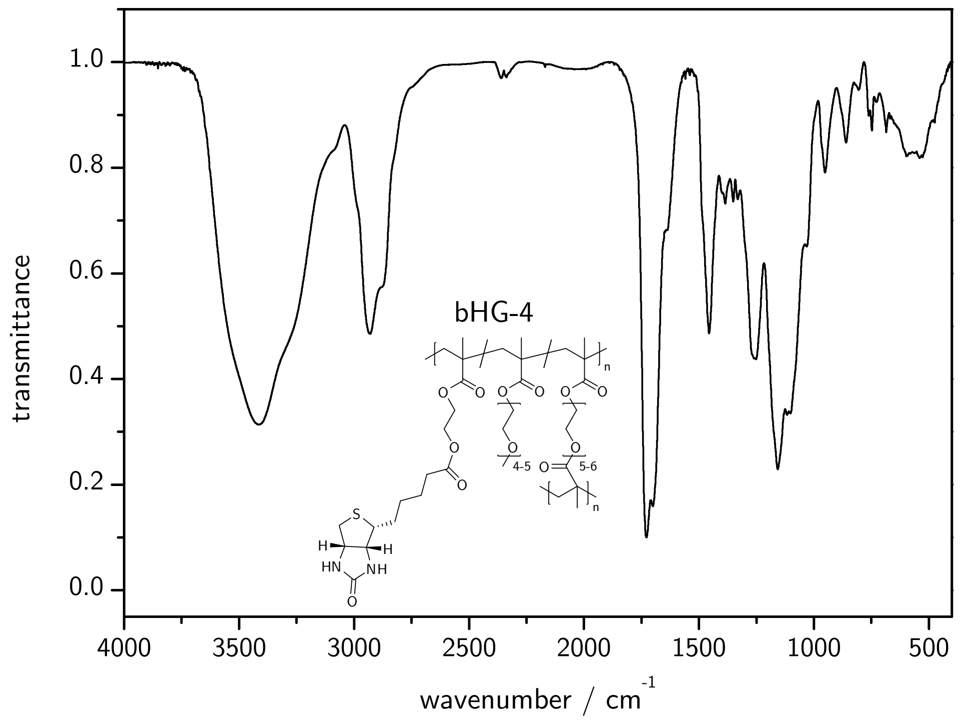

transmittance
1.0
0.8
0.6
0.4
0.2
0.0
4000
3500
3000
2500
2000
1500
1000
500
wavenumber / cm^{-1}
bHG-4
S
H
H
HN
NH
O
4-5
5-6
n

NMR spectra

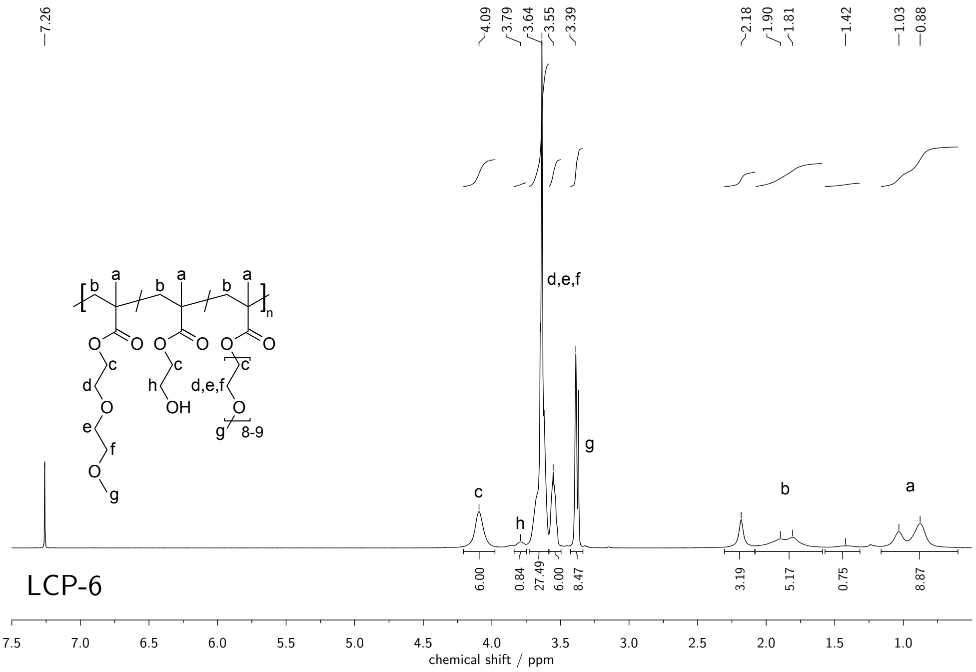
7.26
4.09
3.79
3.64
3.55
3.39
2.18
1.90
1.81
1.42
1.03
0.88
d,e,f
g
c
h
b
a
LCP-6
6.00
0.84
27.49
6.00
8.47
3.19
5.17
0.75
8.87
7.5
7.0
6.5
6.0
5.5
5.0
4.5
4.0
3.5
3.0
2.5
2.0
1.5
1.0
chemical shift / ppm
OH
8-9
n

List of Figures

1.1 Frontal and oblique views of the wing of a butterfly (Morpho didius) (a) and (c) in air and (b) and (d) when immersed into liquid ethanol. Colour change of the wing is observed when the viewing angles are changed, keeping the direction (e) perpendicular and (f) parallel to the wing veins. From [4], used with permission. 1

1.2 SEM micrographs of the lamellar architecture in scales of Morpho didius, M. sulkowskyii and M. rhetenor, observed with various magnifications and angles. From [4], used with permission. 2

1.3 a) Naturally found opal, cut as a gemstone, b) SEM micrograph of a natural opal; the amorphous matrix was partly etched with HF (From [8] with permission). 4

1.4 Schematic drawing of a) a synthetically made opal in a matrix, b) an inverse opal, where particles were etched and cavities are left. . . . 4

1.5 Schematic representation of an opal-based sensor subjected to a stimulus, resulting in deformation of the matrix ($d > d_0$) and a change in Bragg diffraction wavelength. 5

2.1 Particle size distribution of a commercially available Snowtex® ZL silica batch determined by dynamic light scattering. 12

2.2 Overall reaction equation of the condensation of tetraethyl orthosilicate in aqueous media. 13

2.3 Hydrolysis and condensation of tetraethyl orthosilicate in aqueous media. 14

2.4 Simplified interaction scheme of two Stöber silica particles. 18

2.5 Size distribution graphs of two synthesised Stöber silica particle batches; prepared with identical recipes except for different addition speed. . 23

2.6 Size distribution graphs of the synthesised Stöber particles. 26

3.1 a) Silica particles sedimented from ethanol suspension, b) magnification of the iridescent light interference in sedimented silica layer. . . 28
3.2 Scheme of the vertical deposition procedure 29
3.3 Electron micrograph of a colloid crystal consisting of PS colloids. Particles marked in red are non-uniformly sized, causing defects in the crystal structure. Reprinted (adapted) with permission from P. A. Hiltner et al., *The Journal of Physical Chemistry* **1971**, *75*, 1881–1886. Copyright 1971 American Chemical Society. 31
3.4 Crystal structure in opal layers a) common crystal representation; b) crystal orientation in horizontal opal films. 33
3.5 Optical pathways of light beams λ_{hkl} in an opal lattice at an angle of incidence of $\theta = 30°$. Diffraction is illustrated at the lattice planes $(1\,1\,1)$ (black), $(2\,0\,0)$ (red) and $(2\,2\,0)$ (blue) visualising the final direction of the refracted light beams (adapted from [103]). 35
3.6 Measurement setup of the used UV spectrometer in reflection mode (Perkin Elmer Lambda 950 with universal reflectance accessory). Visible are the lower and upper angular extremities, a) 22° and b) 82°. 37
3.7 Scheme of the hydrophilisation of a glass surface. 38
3.8 Photographs of a colloidal crystal **CC-7** deposited from 400 nm SiO_2 particles observed under different arbitrary angles. 41
3.9 SEM micrographs of SiO_2 CCs (with hydrogel matrix) after platinum sputtering. Scale bar is given below the micrographs. 42
3.10 Atomic force micrographs of a CC. a) image from top, defects marked in blue, hexagonal unit in black; b) 3D representation. Scales are depicted in the micrographs. 43
3.11 Plots of UV/Vis transmission measurements of various colloidal crystals deposited on glass slides. 46
3.12 Angular dependent UV/Vis reflection spectra of **CC-8**. Spectra are staggered for better viewing. 47

4.1 Schematic illustration of phase diagrams for polymer solution behaviour (temperature (T) v. polymer volume fraction (ϕ)). 50

4.2 Overview over a selection of oligo(ethylene glycol) methacrylates, sorted by hydrophilicity of the corresponding homopolymers (CPs from literature[107–113] denoted below). 51

4.3 Schematic representation of a polymer chain below and over the LCST. 52

4.4 Plots of measured CPs as a function of average amount of incorporated OEGMA$_{475}$ units per chain of poly(MEO$_2$MA-stat-OEGMA$_{475}$) copolymers with varying composition. (From [127] used with permission.) 54

4.5 Schematic representation of a turbidity measurement of a (co)polymer a) below and b) above the LCST. 56

4.6 Scheme of the radical copolymerisation of binary copolymers **LCP-1** to **LCP-4**. 59

4.7 Scheme of the radical copolymerisation of ternary copolymers **LCP-5** to **LCP-7**. 60

4.8 Plots of transmittance as a function of temperature (670 nm, 1 °C min^{-1}) measured for aqueous solutions (2 g L^{-1}) of a series of linear copolymers (**LCP-1** to **LCP-7**) of varying copolymer composition. 61

4.9 Scheme of the UV-induced radical copolymerisation of ternary hydrogels **HG-1** to **HG-6**. 62

4.10 Scheme of the UV-induced radical copolymerisation of quaternary hydrogels **HG-7** to **HG-10**. 63

4.11 Schematic drawing of the assembled polymerisation mould and procedure used for hydrogel synthesis. 63

4.12 Comparison of the turbidity curve of **LCP-3** (black) with the swelling ratio plot of **HG-3** (red). 66

4.13 Comparison of temperature dependant swelling ratios of **HG-3** (black squares) and **HG-10** (red triangles). 68

5.1 Scheme of the preparation of an inverse hydrogel opal *via* a two-step template infiltration and particle etching. 72

5.2 Schematic drawing of the procedure of monomer infiltration into a colloidal crystal followed by curing with UV light. 72

5.3 Schematic dimensions of the opalescent (multi-coloured) and sheer hydrogel (pale blue) part of an IHO film, which were synthesised in this work. 74

5.4 Photograph of **IHO-2** floating on water, illuminated from the side with white light. Size of the sample approx. 25 mm × 20 mm. 75
5.5 Plot of temperature dependant UV/Vis absorption measurements in ultra-pure water of **IHO-1**. The spectra are vertically staggered for better readability. 76
5.6 Plot of temperature dependant UV/Vis absorption measurements in ultra-pure water of **IHO-2**. The spectra are vertically staggered for better readability. 77
5.7 Plot of Bragg peak wavelength (λ_{max}) relative to temperature for **IHO-1** (black squares) and **IHO-2** (red circles). For both series, a cubic fit was applied. 78
5.8 SEM micrographs of an inverse hydrogel opal after platinum sputtering. Scale bar is given below the micrographs. For details on sample preparation and execution of the analysis see experimental part. . . . 79
5.9 Scheme of HABA-functionalisation of IHOs, exemplarily shown for **IHO-1**. 84
5.10 UV/Vis spectra and corresponding calibration curve at $\lambda = 500$ nm of a concentration series of HABA-propionate in PBS buffer. 85
5.11 Structure, tautomerism and corresponding emission maxima of 3'-(carboxyethyl)-4'-hydroxyazobenzene-2-carboxylic acid (HABA-propionate). 85
5.12 V/Vis spectrum of **IHO-1** functionalised with HABA-propionate. . 86
5.13 Scheme of the biotinylation of IHOs; exemplarily shown for **IHO-1**. 89
5.14 Overlay of a selected region of the normalised infrared spectra of **IHO-1** (black) and **bIHO-1** (red). 91
5.15 Schematic representation of a biotinylated (grey circles) hydrogel network, with bound avidin (blue squares with binding pockets) and excess of coupled biotin. 93
5.16 Comparison of swelling ratios of non-functionalised **IHO-1** (black squares) with biotinylated **bIHO-1** (red circles). Cubic fits were applied to guide the eye. 94
5.17 Plot of band gap wavelengths (λ_{max}) relative to temperature for **IHO-2** (black squares), **bIHO-2** (red circles) and **bIHO-2** with avidin (blue triangles). 95
5.18 Plot of band gap wavelengths (λ_{max}) relative to temperature for **IHO-1** (black squares), **bIHO-1** (red circles) and **bIHO-1** with avidin (blue triangles). 96

5.19 Plot of band gap wavelength (λ_{max}) relative to temperature for **IHO-1** (black squares), **IHO-1** with avidin (gree diamonds) and **bIHO-1** with avidin (blue triangles). 97

List of Tables

2.1 Summary of the influence of several reaction parameters on SiO_2 particle size in Stöber synthesis. 16

2.2 Reaction parameters for the syntheses of selected SiO_2 particles. . . 24

2.3 DLS data of selected SiO_2 particles. 25

3.1 Overview over selected vertical deposition experiments of SiO_2 particles (**SP-3**) with $d \approx 400\,\text{nm}$. Concentrations were adjusted with absolute ethanol ($w_{EtOH} = 100\,\% - w_{SiO_2} - w_{H_2O}$). 39

3.2 Overview over average silica particle (**SP-3**) diameters determined *via* various methods. 44

4.1 Composition and CP_{50} of various synthesised linear copolymers. . . 59

4.2 Composition and appearance of various p(HEMA-stat-OEGMA$_{300}$-stat-OEGDMA$_{400}$) and p(HEMA-stat-OEGMA$_{475}$-stat-MEO$_2$MA-stat-OEGDMA$_{550}$) hydrogels cured by UV-induced polymerisation in a glass slide mould.[a] 65

5.1 Composition of prepared inverse hydrogel opals, assembled around **CC-7** templates. 73

5.2 Calculated mesh sizes for selected swollen hydrogels. 82

5.3 Summary of UV/Vis data, calculated concentrations and amount of 3'-(carboxyethyl)-4'-hydroxyazobenzene-2-carboxylic acid (HABA-propionate) coupled to a p(HEMA-stat-OEGMA$_{300}$-stat-OEGDMA$_{400}$) IHO (**IHO-1**). 87

5.4 Accessible amount of biotin per gram of hydrogel for HEMA-rich and -poor inverse hydrogel opals, determined *via* biotin/avidin assay. 92

5.5 Summary of band gap wavelengths at various temperatures for non-functionalised and biotinylated **IHO-1** with and without addition of avidin. 98

7.1 SEC data of the synthesised linear copolymers **LCP-1** to **-4**. 111
7.2 SEC data of the synthesised linear copolymers **LCP-5** to **-7**. 112

Bibliography

[1] K. Chung, S. Yu, C.-J. Heo, J. W. Shim, S.-M. Yang, M. G. Han, H.-S. Lee, Y. Jin, S. Y. Lee, N. Park, J. H. Shin, *Advanced Materials* **2012**, *24*, 2375–2379.

[2] H. Ghiradella, *Applied Optics* **1991**, *30*, 3492.

[3] S. Kinoshita, S. Yoshioka, K. Kawagoe, *Proceedings of the Royal Society B: Biological Sciences* **2002**, *269*, 1417–1421.

[4] S. Kinoshita, S. Yoshioka, J. Miyazaki, *Reports on Progress in Physics* **2008**, *71*, 076401.

[5] R. T. Lee, G. S. Smith, *Applied Optics* **2009**, *48*, 4177.

[6] W. Zhang, D. Zhang, T. Fan, J. Ding, J. Gu, Q. Guo, H. Ogawa, *Bioinspiration & Biomimetics* **2006**, *1*, 89–95.

[7] J. B. Jones, J. V. Sanders, E. R. Segnit, *Nature* **1964**, *204*, 990–991.

[8] J. V. Sanders, *Nature* **1964**, *204*, 1151–1153.

[9] P. J. Darragh, A. J. Gaskin, B. C. Terrel, J. V. Sanders, *Nature* **1966**, *209*, 13–16.

[10] P. Gilson, *Journal of Gemmology* **1979**, *16*, 494–498.

[11] Y. Zhao, I. Avrutsky, *Optics Letters* **1999**, *24*, 817.

[12] W. Lee, S. Pruzinsky, P. Braun, *Advanced Materials* **2002**, *14*, 271–274.

[13] S. A. Rinne, F. García-Santamaría, P. V. Braun, *Nature Photonics* **2007**, *2*, 52–56.

[14] V. L. Alexeev, S. Das, D. N. Finegold, S. A. Asher, *Clinical Chemistry* **2004**, *50*, 2353–2360.

[15] K. Kamiyama, *pat.*, EP0141388A2, **1985**.

[16] G. Pauley, *pat.*, WO95/25642, **1995**.

[17] R. H. Kearnes, S. F. Starcke, *pat.*, US7,290,404, **2007**.

[18] Y. Zhao, X. Zhao, Z. Gu, *Advanced Functional Materials* **2010**, *20*, 2970–2988.

[19] J. Shin, P. V. Braun, W. Lee, *Sensors and Actuators B: Chemical* **2010**, *150*, 183–190.

[20] J. Y. Wang, Y. C. Han, *Journal of Colloid and Interface Science* **2011**, *353*, 498–505.

[21] M. Xu, A. V. Goponenko, S. A. Asher, *Journal of the American Chemical Society* **2008**, *130*, 3113–3119.

[22] A. Bozolan, R. M. Gerosa, C. J. S. d. Matos, M. A. Romero, *IEEE Sensors Journal* **2012**, *12*, 195–200.

[23] T. Cai, G. N. Wang, S. Thompson, M. Marquez, Z. B. Hu, *Macromolecules* **2008**, *41*, 9508–9512.

[24] J. D. Debord, L. A. Lyon, *Journal of Physical Chemistry B* **2000**, *104*, 6327–6331.

[25] N. Griffete, M. Dybkowska, B. Glebocki, T. Basinska, C. Connan, A. Maitre, M. M. Chehimi, S. Slomkowski, C. Mangeney, *Langmuir* **2010**, *26*, 11550–11557.

[26] M. Zhou, F. B. Xing, M. L. Ren, Y. Feng, Y. Q. Zhao, H. X. Qiu, X. D. Wang, C. J. Gao, F. F. Sun, Y. Q. He, Z. Q. Ma, P. Wen, J. P. Gao, *Chemphyschem* **2009**, *10*, 523–526.

[27] C. L. Chi, T. Cai, Z. B. Hu, *Langmuir* **2009**, *25*, 3814–3819.

[28] C. Fenzl, T. Hirsch, O. Wolfbeis, *Sensors* **2012**, *12*, 16954–16963.

[29] H. Fudouzi, Y. Xia, *Advanced Materials* **2003**, *15*, 892–896.

[30] T. Kanai, S. Yamamoto, T. Sawada, *Macromolecules* **2011**, *44*, 5865–5867.

[31] N. Kumano, T. Seki, M. Ishii, H. Nakamura, Y. Takeoka, *Angewandte Chemie - International Edition* **2011**, *50*, 4012–4015.

[32] S. Colodrero, M. Ocana, A. R. Gonzalez-Elipe, H. Miguez, *Langmuir* **2008**, *24*, 9135–9139.

[33] J. H. Kim, J. H. Moon, S. Y. Lee, J. Park, J. H. Kim, J. H. Moon, S.-Y. Lee, J. Park, *Applied Physics Letters* **2010**, *97*, 103701.

[34] H. Yang, P. Jiang, *Applied Physics Letters* **2011**, *98*, 11104.

[35] R. A. Barry, P. Wiltzius, *Langmuir* **2006**, *22*, 1369–1374.

[36] D. Arunbabu, A. Sannigrahi, T. Jana, *Soft Matter* **2011**, *7*, 2592–2599.

[37] W. Hong, X. B. Hu, B. Y. Zhao, F. Zhang, D. Zhang, *Advanced Materials* **2010**, *22*, 5043–5047.

[38] X. B. Hu, J. Huang, W. X. Zhang, M. Li, C. G. Tao, G. T. Li, X. Hu, J. Huang, W. Zhang, M. Li, C. Tao, G. Li, *Advanced Materials* **2008**, *20*, 4074–4078.

[39] Z. H. Wang, J. H. Zhang, Z. C. Tian, Z. Y. Wang, Y. F. Li, S. Liang, L. Y. Cui, L. A. Zhang, H. Zhang, B. Yang, *Chemical Communications* **2010**, *46*, 8636–8638.

[40] T. Cassagneau, F. Caruso, *Advanced Materials* **2002**, *14*, 34–38.

[41] G. R. Hendrickson, L. A. Lyon, *Soft Matter* **2009**, *5*, 29–35.

[42] M. Ben-Moshe, V. L. Alexeev, S. A. Asher, *Analytical Chemistry* **2006**, *78*, 5149–5157.

[43] T. Cassagneau, F. Caruso, *Advanced Materials* **2002**, *14*, 1629–1633.

[44] X. B. Hu, Q. An, G. T. Li, S. Y. Tao, B. Liu, *Angewandte Chemie - International Edition* **2006**, *45*, 8145–8148.

[45] G. A. Ozin, L. D. Bonifacio, B. V. Lotsch, D. P. Puzzo, F. Scotognella, *Advanced Materials* **2009**, *21*, 1641–1646.

[46] W. Z. Shen, M. Z. Li, L. A. Xu, S. T. Wang, L. Jiang, Y. L. Song, D. B. Zhu, *Biosensors & Bioelectronics* **2011**, *26*, 2165–2170.

[47] M. Honda, K. Kataoka, T. Seki, Y. Takeoka, *Langmuir* **2009**, *25*, 8349–8356.

[48] S. A. Asher, J. Holtz, L. Liu, Z. J. Wu, *Journal of the American Chemical Society* **1994**, *116*, 4997–4998.

[49] V. L. Alexeev, A. C. Sharma, A. V. Goponenko, S. Das, I. K. Lednev, C. S. Wilcox, D. N. Finegold, S. A. Asher, *Analytical Chemistry* **2003**, *75*, 2316–2323.

[50] G. A. Ozin, L. D. Bonifacio, D. P. Puzzo, S. Breslav, B. M. Willey, A. McGeer, *Advanced Materials* **2010**, *22*, 1351–+.

[51] Y. H. Ye, F. LeBlanc, A. Hache, V. V. Truong, *Applied Physics Letters* **2001**, *78*, 52–54.

[52] Y. G. Ko, D. H. Shin, *Journal of Physical Chemistry B* **2007**, *111*, 1545–1551.

[53] H. Cong, W. Cao, *Langmuir* **2003**, *19*, 8177–8181.

[54] B. Hatton, L. Mishchenko, S. Davis, K. H. Sandhage, J. Aizenberg, *Proceedings of the National Academy of Sciences of the United States of America* **2010**, *107*, 10354–10359.

[55] Z. Zhou, X. S. Zhao, *Langmuir* **2004**, *20*, 1524–1526.

[56] L. M. Goldenberg, J. Wagner, J. Stumpe, B. R. Paulke, E. Gornitz, *Materials Science & Engineering C-Biomimetic and Supramolecular Systems* **2002**, *22*, 405–408.

[57] A. S. Dimitrov, K. Nagayama, *Langmuir* **1996**, *12*, 1303–1311.

[58] J. Bertone, P. Jiang, K. Hwang, D. Mittleman, V. Colvin, *Physical Review Letters* **1999**, *83*, 300–303.

[59] P. Jiang, J. F. Bertone, K. S. Hwang, V. L. Colvin, *Chemistry of Materials* **1999**, *11*, 2132–2140.

[60] S. A. Johnson, P. J. Ollivier, T. E. Mallouk, *Science* **1999**, *283*, 963–965.

[61] D. A. S. Razo, L. Pallavidino, E. Garrone, F. Geobaldo, E. Descrovi, A. Chiodoni, F. Giorgis, *Journal of Nanoparticle Research* **2008**, *10*, 1225–1229.

[62] Y. Takeoka, M. Watanabe, *Langmuir* **2003**, *19*, 9104–9106.

[63] Y. Takeoka, T. Seki, *Langmuir* **2006**, *22*, 10223–10232.

[64] F. J. Xu, H. Z. Li, J. Li, Y. H. E. Teo, C. X. Zhu, E. T. Kang, K. G. Neoh, *Biosensors & Bioelectronics* **2008**, *24*, 773–780.

[65] W. Stoeber, A. Fink, E. Bohn, *Journal of Colloid and Interface Science* **1968**, *26*, 62–69.

[66] C. J. Brinker, G. W. Scherer, *Sol-gel science: The physics and chemistry of sol-gel processing*, Academic Press, Boston [etc.], **1990**.

[67] W. Noll, O. Glenz, G. Hecht, *Chemie und Technologie der Silicone*, Verlag Chemie, 2nd ed., **1968**.

[68] D. W. Schaefer, K. D. Keefer, *Phys. Rev. Lett.* **1984**, *53*, 1383–1386.

[69] C. H. Byers, M. T. Harris, D. F. Williams, *Industrial & Engineering Chemistry Research* **1987**, *26*, 1916–1923.

[70] M. T. Harris, R. R. Brunson, C. H. Byers, *Journal of Non-Crystalline Solids* **1990**, *121*, 397–403.

[71] T. Matsoukas, E. Gulari, *Journal of Colloid and Interface Science* **1988**, *124*, 252–261.

[72] R. Aelion, A. Loebel, F. Eirich, *Journal of the American Chemical Society* **1950**, *72*, 5705–5712.

[73] G. H. Bogush, M. A. Tracy, C. F. Zukoski, *Journal of Non-Crystalline Solids* **1988**, *104*, 95–106.

[74] K. Nozawa, H. Gailhanou, L. Raison, P. Panizza, H. Ushiki, E. Sellier, J. P. Delville, M. H. Delville, *Langmuir* **2005**, *21*, 1516–1523.

[75] V. K. LaMer, R. H. Dinegar, *Journal of the American Chemical Society* **1950**, *72*, 4847–4854.

[76] A. C. Makrides, M. Turner, J. Slaughter, *Journal of Colloid and Interface Science* **1980**, *73*, 345–367.

[77] P. J. Feeney, D. H. Napper, R. G. Gilbert, *Macromolecules* **1984**, *17*, 2520–2529.

[78] W. Ostwald, *Lehrbuch der Allgemeinen Chemie*, *Vol. 1*, Leipzig, 2nd ed., **1896**.

[79] H. Hamaker, *Physica IV* **1937**, *4*, 1058–1072.

[80] Z. Kiraly, L. Turi, I. Dekany, K. Bean, B. Vincent, *Colloid & Polymer Science* **1996**, *274*, 779–787.

[81] W. Brown, *Dynamic light scattering: The method and some applications*, Clarendon Press and Oxford University Press, Oxford [England] and New York, **1993**.

[82] W. I. Goldburg, *American Journal of Physics* **1999**, *67*, 1152.

[83] C. S. Johnson, D. A. Gabriel, *Laser light scattering*, Dover, New York, **1994**.

[84] C. Washington, *Particle size analysis in pharmaceutics and other industries: Theory and practice*, E. Horwood, New York, **1992**.

[85] *Measurement of suspended particles by quasi-elastic light scattering*, (Ed.: B. E. Dahneke), Wiley, New York, **1983**.

[86] R. Pecora, *Dynamic light scattering: Applications of photon correlation spectroscopy*, Plenum Press, New York, **1985**.

[87] Y. N. Xia, B. Gates, Y. D. Yin, Y. Lu, *Advanced Materials* **2000**, *12*, 693–713.

[88] P. Jiang, M. J. McFarland, *Journal of the American Chemical Society* **2004**, *126*, 13778–13786.

[89] H. T. Yang, P. Jiang, *Langmuir* **2010**, *26*, 13173–13182.

[90] J. Aizenberg, B. Hatton, L. Mishchenko, S. Davis, K. H. Sandhage, *Proceedings of the National Academy of Sciences of the United States of America* **2010**, *107*, 10354–10359.

[91] P. A. Hiltner, Y. S. Papir, I. M. Krieger, *The Journal of Physical Chemistry* **1971**, *75*, 1881–1886.

[92] B. Ackerson, S. Paulin, B. Johnson, W. van Megen, S. Underwood, *Physical Review E* **1999**, *59*, 6903–6913.

[93] S.-L. Kuai, X.-F. Hu, A. Haché, V.-V. Truong, *Journal of Crystal Growth* **2004**, *267*, 317–324.

[94] E. C. H. Ng, K. M. Chin, C. C. Wong, *Langmuir* **2011**, *27*, 2244–2249.

[95] J.-M. Meijer, F. Hagemans, L. Rossi, D. V. Byelov, S. I. Castillo, A. Snigirev, I. Snigireva, A. P. Philipse, A. V. Petukhov, *Langmuir* **2012**, *28*, 7631–7638.

[96] T. Okubo, *Journal of the American Chemical Society* **1990**, *112*, 5420–5424.

[97] O. D. Velev, A. M. Lenhoff, *Current Opinion in Colloid & Interface Science* **2000**, *5*, 56–63.

[98] P. Pieranski, *Contemporary Physics* **1983**, *24*, 25–73.

[99] B. T. Holland, *Science* **1998**, *281*, 538–540.

[100] P. Jiang, T. Prasad, M. J. McFarland, V. L. Colvin, P. Jiang, T. Prasad, M. J. McFarland, V. L. Colvin, *Applied Physics Letters* **2006**, *89*, 011908.

[101] W. Luck, M. Klier, H. Wesslau, *Naturwissenschaften* **1963**, *50*, 485.

[102] P. A. Hiltner, I. M. Krieger, *Journal of Physical Chemistry* **1969**, *73*, 2386.

[103] P. Spahn, PhD thesis, Technische Universität, Darmstadt, **2008**.

[104] Y. Lu, Y. Yin, Z.-Y. Li, Y. Xia, *Langmuir* **2002**, *18*, 7722–7727.

[105] C. Simmonds, *Alcohol, its production, properties, chemistry, and industrial applications*, MacMillan, London, **1919**.

[106] S. H. Im, M. H. Kim, O. O. Park, *Chemistry of Materials* **2003**, *15*, 1797–1802.

[107] C. R. Becer, S. Hahn, M. W. M. Fijten, H. M. L. Thijs, R. Hoogenboom, U. S. Schubert, *Journal of Polymer Science Part A: Polymer Chemistry* **2008**, *46*, 7138–7147.

[108] J. F. Lutz, A. Hoth, *Macromolecules* **2006**, *39*, 893–896.

[109] S. Han, M. Hagiwara, T. Ishizone, *Macromolecules* **2003**, *36*, 8312–8319.

[110] G. Coullerez, A. Carlmark, E. Malmström, M. Jonsson, *The Journal of Physical Chemistry A* **2004**, *108*, 7129–7131.

[111] D. Neugebauer, Y. Zhang, T. Pakula, S. S. Sheiko, K. Matyjaszewski, *Macromolecules* **2003**, *36*, 6746–6755.

[112] Y. Maeda, T. Kubota, H. Yamauchi, T. Nakaji, H. Kitano, *Langmuir* **2007**, *23*, 11259–11265.

[113] T. Ishizone, A. Seki, M. Hagiwara, S. Han, H. Yokoyama, A. Oyane, A. Deffieux, S. Carlotti, *Macromolecules* **2008**, *41*, 2963–2967.

[114] V. Aseyev, H. Tenhu, F. M. Winnik, *Adv. Polym. Sci. (Advances in Polymer Science)* **2011**, *242*, 29–89.

[115] G. D. Smith, D. Bedrov, *The Journal of Physical Chemistry B* **2003**, *107*, 3095–3097.

[116] M. Heskins, J. E. Guillet, *Journal of Macromolecular Science: Part A - Chemistry* **1968**, *2*, 1441–1455.

[117] H. Schild, *Progress in Polymer Science* **1992**, *17*, 163–249.

[118] R. Liu, M. Fraylich, B. R. Saunders, *Colloid and Polymer Science* **2009**, *287*, 627–643.

[119] X. Wang, X. Qiu, C. Wu, *Macromolecules* **1998**, *31*, 2972–2976.

[120] X. Wang, C. Wu, *Macromolecules* **1999**, *32*, 4299–4301.

[121] H. Cheng, L. Shen, C. Wu, *Macromolecules* **2006**, *39*, 2325–2329.

[122] Y. Xia, N. A. D. Burke, H. D. H. Stöver, *Macromolecules* **2006**, *39*, 2275–2283.

[123] S. Furyk, Y. Zhang, D. Ortiz-Acosta, P. S. Cremer, D. E. Bergbreiter, *Journal of Polymer Science Part A: Polymer Chemistry* **2006**, *44*, 1492–1501.

[124] M. M. Ali, H. D. H. Stöver, *Macromolecules* **2004**, *37*, 5219–5227.

[125] H. Kitano, T. Hirabayashi, M. Gemmei-Ide, M. Kyogoku, *Macromolecular Chemistry and Physics* **2004**, *205*, 1651–1659.

[126] J.-F. Lutz, K. Weichenhan, O. Akdemir, A. Hoth, *Macromolecules* **2007**, *40*, 2503–2508.

[127] J.-F. Lutz, *Journal of Polymer Science Part A: Polymer Chemistry* **2008**, *46*, 3459–3470.

[128] J. T. de Carle, *pat.*, US 39,376,680, **1976**.

[129] P. Hofer, U. Mueller, M. Barenz, H. Schafer, W. Mueller-Lierheim, *pat.*, US 4,463,148, **1984**.

[130] T. Kindt-Larsen, P. Wolff, J.-E. Soerensen, F. R. Steenstrup, H. Rossignol, F. F. Molock, *pat.*, US 6,846,892, **2005**.

[131] Y.-C. Lai, P. L. J. Valint, *pat.*, US 5,726,733, **1998**.

[132] Y. C. Bae, S. M. Lambert, D. S. Soane, J. M. Prausnitz, *Macromolecules* **1991**, *24*, 4403–4407.

[133] C. Porsch, S. Hansson, N. Nordgren, E. Malmström, *Polymer Chemistry* **2011**, *2*, 1114.

[134] I. Berndt, C. Popescu, F.-J. Wortmann, W. Richtering, *Angewandte Chemie International Edition* **2006**, *45*, 1081–1085.

[135] F. J. Xu, E. T. Kang, K. G. Neoh, *Biomaterials* **2006**, *27*, 2787–2797.

[136] K. van Durme, G. van Assche, B. van Mele, *Macromolecules* **2004**, *37*, 9596–9605.

[137] X. Ma, Y. Cui, X. Zhao, S. Zheng, X. Tang, *Journal of Colloid and Interface Science* **2004**, *276*, 53–59.

[138] J. Buller, A. Laschewsky, E. Wischerhoff, *Soft Matter* **2013**, *9*, 929.

[139] J. Buller, A. Laschewsky, J.-F. Lutz, E. Wischerhoff, *Polymer Chemistry* **2011**, *2*, 1486.

[140] P. J. Flory, J. Rehner, *The Journal of Chemical Physics* **1943**, *11*, 521.

[141] P. J. Flory, *The Journal of Chemical Physics* **1950**, *18*, 108.

[142] J. Buller, PhD thesis, Universität Potsdam, Potsdam, **2013**.

[143] T. Cai, M. Marquez, Z. B. Hu, *Langmuir* **2007**, *23*, 8663–8666.

[144] D. Buenger, F. Topuz, J. Groll, *Progress in Polymer Science* **2012**, *37*, 1678–1719.

[145] L. L. Duan, B. You, L. M. Wu, M. Chen, *Journal of Colloid and Interface Science* **2011**, *353*, 163–168.

[146] Z. B. Hu, X. H. Lu, J. Gao, *Advanced Materials* **2001**, *13*, 1708–1712.

[147] M. Kumoda, M. Watanabe, Y. Takeoka, *Langmuir* **2006**, *22*, 4403–4407.

[148] J. R. Lawrence, G. H. Shim, P. Jiang, M. G. Han, Y. Ying, S. H. Foulger, *Advanced Materials* **2005**, *17*, 2344–2349.

[149] Y. J. Lee, C. E. Heitzman, W. R. Frei, H. T. Johnson, P. V. Braun, *Journal of Physical Chemistry B* **2006**, *110*, 19300–19306.

[150] Y.-J Lee, P. Braun, *Advanced Materials* **2003**, *15*, 563–566.

[151] J. Shin, S. G. Han, W. Lee, *Sensors and Actuators B: Chemical* **2012**, *168*, 20–26.

[152] I. Tokarev, S. Minko, *Advanced Materials* **2010**, *22*, 3446–3462.

[153] J. Y. Wang, Y. Cao, Y. Feng, F. Yin, J. P. Gao, *Advanced Materials* **2007**, *19*, 3865–3871.

[154] J. Y. Wang, Y. C. Han, *Langmuir* **2009**, *25*, 1855–1864.

[155] J. Y. Wang, Y. C. Han, *Journal of Colloid and Interface Science* **2011**, *357*, 139–146.

[156] N. G. Khlebtsov, B. N. Khlebtsov, V. A. Khanadeev, *Langmuir* **2008**, *24*, 8964–8970.

[157] M. A. Biot, *Journal of Applied Physics* **1941**, *12*, 155.

[158] J. Yoon, S. Cai, Z. Suo, R. C. Hayward, *Soft Matter* **2010**, *6*, 6004.

[159] N. Bouklas, R. Huang, *Soft Matter* **2012**, *8*, 8194.

[160] N. A. Peppas, H. J. Moynihan, L. M. Lucht, *Journal of Biomedical Materials Research* **1985**, *19*, 397–411.

[161] T. Canal, N. A. Peppas, *Journal of Biomedical Materials Research* **1989**, *23*, 1183–1193.

[162] J. A. E. Määttä, T. T. Airenne, H. R. Nordlund, J. Jänis, T. A. Paldanius, P. Vainiotalo, M. S. Johnson, M. S. Kulomaa, V. P. Hytönen, *ChemBioChem* **2008**, *9*, 1124–1135.

[163] H. Hofstetter, M. Morpurgo, O. Hofstetter, E. A. Bayer, M. Wilchek, *Analytical Biochemistry* **2000**, *284*, 354–366.

[164] Y. Zhu, B. Lv, P. Zhang, H. Ma, *Chemical Communications* **2011**, *47*, 9855.

[165] N. M. Green, *Biochem. J. (Biochemical Journal)* **1963**, *89*, 585–591.

[166] B. Friguet, A. F. Chaffotte, L. Djavadi-Ohaniance, M. E. Goldberg, *Journal of Immunological Methods* **1985**, *77*, 305–319.

[167] N. M. Green in *Methods in Enzymology*, *Vol. 18*, pp. 418–424.